การสร้างเส้นใยนาโนแบบยืดหยุ่นของพอลิอะคริโลไนไตรล์/ซิงค์ออกไซด์ชนิดแกนร่วมที่มีความ
ว่องไวในการเร่งปฏิกิริยาโดยใช้แสงโดยการปั่นเส้นใยด้วยไฟฟ้าสถิต

นายกัญชัช ชัชกุล

FABRICATION OF FLEXIBLE POLYACRYLONITRILE/ZINC OXIDE CO-AXIAL NANOFIBERS
WITH PHOTOCATALYTIC ACTIVITY BY ELECTROSPINNING

Mr. Kanchat Chutchakul

A Thesis Submitted in Partial Fulfillment of the Requirements

for the Degree of Master of Engineering Program in Chemical Engineering

Department of Chemical Engineering

Faculty of Engineering

Chulalongkorn University

Academic Year 2013

Thesis Title	FABRICATION OF FLEXIBLE POLYACRYLONITRILE/ZINC OXIDE CO-AXIAL NANOFIBERS WITH PHOTOCATALYTIC ACTIVITY BY ELECTROSPINNING
By	Mr. Kanchat Chutchakul
Field of Study	Chemical Engineering
Thesis Advisor	Assistant Professor Varong Pavarajarn, Ph.D.

Accepted by the Faculty of Engineering, Chulalongkorn University in Partial Fulfillment of the Requirements for the Master's Degree

.... Dean of the Faculty of Engineering

(Professor Bundhit Eua-arporn, Ph.D.)

THESIS COMMITTEE

.... Chairman

(Akawat Sirisuk, Ph.D.)

.... Thesis Advisor

(Assistant Professor Varong Pavarajarn, Ph.D.)

.... Examiner

(Assistant Professor Apinan Soottitantawat, D.Eng.)

.... External Examiner

(Chanchana Thanachayanont, Ph.D.)

กัญชัช ชัชกุล : การสร้างเส้นใยนาโนแบบยืดหยุ่นของพอลิอะคริโลไนไตรล์/ซิงค์ออกไซด์ชนิดแกนร่วมที่มีความว่องไวในการเร่งปฏิกิริยาโดยใช้แสงโดยการปั่นเส้นใยด้วยไฟฟ้าสถิต. (FABRICATION OF FLEXIBLE POLYACRYLONITRILE/ZINC OXIDE CO-AXIAL NANOFIBERS WITH PHOTOCATALYTIC ACTIVITY BY ELECTROSPINNING) อ.ที่ปรึกษาวิทยานิพนธ์หลัก: ผศ. ดร. วรงค์ ปวราจารย์, 160 หน้า.

เส้นใยนาโนของพอลิอะคริโลไนไตรล์/ซิงค์ออกไซด์ชนิดแกนร่วมถูกสร้างขึ้นให้มีโครงสร้างที่ยืดหยุ่นของแกน/เปลือกหุ้ม ด้วยวิธี โซล-เจล ร่วมกับเทคนิคการปั่นเส้นใยแกนร่วมด้วยไฟฟ้าสถิต พอลิอะคริโลไนไตรล์ที่ละลายในไดเมทิลฟอร์มาไมด์ถูกใช้เป็นสารละลายแกน ในขณะที่สารละลายของพอลิไวนิลไพริลิโดนผสมกับซิงค์ออกไซด์โซลในไดเมทิลฟอร์มาไมด์ถูกใช้เป็นสารละลายเปลือกหุ้ม ความเข้มข้นของพอลิอะคริโลไนไตรล์ในสารละลายแกนถูกปรับค่าในช่วง 8% ถึง 12% โดยน้ำหนัก ในขณะที่พอลิไวนิลไพโรลิโดนในสารละลายเปลือกหุ้มถูกปรับค่าในช่วง 8% ถึง 18% โดยน้ำหนัก ทั้งนี้สามารถสร้างเส้นใยแกนร่วมที่ขนาดสม่ำเสมอโดยไม่มีเม็ดบีด ภายใต้ศักย์ไฟฟ้าที่ใช้เท่ากับ 25 กิโลโวลต์ต่อเซนติเมตร หลังจากเผาที่อุณหภูมิในช่วง 300 ถึง 500 องศาเซลเซียส พอลิไวนิลไพโรลิโดนในเปลือกหุ้มจะสลายตัวออกในขณะที่ซิงค์ออกไซด์โซลจะกลายเป็นผลึกระดับนาโนของซิงค์ออกไซด์ ติดอยู่บนแกนพอลิอะคริโลไนไตรล์ แกนพอลิอะคริโลไนไตรล์ซึ่งสามารถทนอุณหภูมิที่เผา จะทำให้เกิดความยืดหยุ่นของเส้นใยพอลิอะคริโลไนไตรล์/ซิงค์ออกไซด์ชนิดแกนร่วม เพื่อหลีกเลี่ยงปัญหาการแตกหักของเส้นใยในระหว่างการใช้งาน เส้นใยหลังเผาแล้วมีขนาดเส้นผ่านศูนย์กลางเฉลี่ย 210-1,400 นาโนเมตร และมีขนาดผลึก 21-39 นาโนเมตร พบว่าความว่องไวในการเร่งปฏิกิริยาของเส้นใยขนาดนาโนของพอลิอะคริโลไนไตรล์/ซิงค์ออกไซด์ชนิดแกนร่วมในการทดสอบการสลายตัวของสีย้อมเมทิลีนบลูโดยใช้แสงมีค่าใกล้เคียงกับซิงค์ออกไซด์ชนิดอนุภาคนาโน นอกจากนี้ยังได้ศึกษาอิทธิพลของอุณหภูมิการเผา ระยะเวลาการเผา และระยะเวลาการบ่มออกไซด์โซล ต่อความว่องไวในการเร่งปฏิกิริยา

ภาควิชา	วิศวกรรมเคมี	ลายมือชื่อนิสิต ....
สาขาวิชา	วิศวกรรมเคมี	ลายมือชื่อ อ.ที่ปรึกษาวิทยานิพนธ์หลัก ....
ปีการศึกษา	2556	

5570119421 : MAJOR CHEMICAL ENGINEERING

KEYWORDS: ZINC OXIDE / NANOFIBERS / CO-AXIAL ELECTROSPINNING / FLEXIBLE / PHOTOCATALYST

KANCHAT CHUTCHAKUL: FABRICATION OF FLEXIBLE POLYACRYLONITRILE/ZINC OXIDE CO-AXIAL NANOFIBERS WITH PHOTOCATALYTIC ACTIVITY BY ELECTROSPINNING. ADVISOR: ASST. PROF. VARONG PAVARAJARN, Ph.D., 160 pp.

Polyacrylonitrile (PAN)/zinc oxide (ZnO) nanofibers were fabricated in flexible core/sheath structure using combination of sol-gel and co-axial electrospinning techniques. PAN dissolved in dimethyl formamide (DMF) was used as core-solution while poly vinyl pyrrolidone (PVP) solution containing ZnO sol in DMF was used as sheath-solution. Concentration of PAN in the core-solution was varied in the range of 8 to 12 wt%, while the PVP concentration in the sheath-solution was varied in the range of 8 to 18 wt%. Under the applied potential of 25 kV/cm, the uniform and bead-free co-axial nanofibers can be fabricated. Upon the calcination, at temperature in the range of 300-500oC, PVP in the sheath is removed while ZnO sol is crystallized into ZnO nanoparticles attached to the PAN core. The presence of PAN core, which can withstand the calcination, provides flexibility for the final PAN/ZnO nanofibers so that crumbling of the fibers during the use can be avoided. The calcined fibers have average diameter of 210-1,400 nm and 21-39 nm in crystalline size of ZnO. The activity of PAN/ZnO nanofibers on the photocatalytic degradation of methylene blue is almost the same as that of ZnO nanoparticles. Furthermore, the effects of calcination temperature, calcination time, and aging time of ZnO sol on the photocatalytic activity were studied.

Department:	Chemical Engineering	Student's Signature	....
Field of Study:	Chemical Engineering	Advisor's Signature	....
Academic Year:	2013		

ACKNOWLEDGEMENTS

CONTENTS

CHAPTER I

INTRODUCTION

Heterogeneous photocatalytic technology has been attracting much attention to industry today because of its diversely potential applications, including environmental remediation, production of renewable fuel, organic syntheses and so on. The more global environmental pollution has been recognized as a serious problem that needs to be solved, the more heterogeneous photocatalytic has been continuingly studied. Therefore the heterogeneous photocatalysis, in which solid photocatalysts are used. The basic principle of semiconductor photocatalytic reaction relies on light irradiation. When the energy of the irradiating light is greater than the band gap, it gives rise to excited state of electrons and holes at the conduction band and valence band of the semiconductor, respectively. Consequently they initiate various redox reactions at the semiconductor surfaces or interface, leading to the decomposition of pollutants. Among the various semiconductor materials, zinc oxide (ZnO) is one of the most significant and promising semiconductors because of its suitable band gap that can utilize UV light, the chemical inertness and nontoxicity making it a superior photocatalyst.

Based on the theoretical considerations (e.g., high surface area, high crystallinity), utilization of water suspension of nanoparticles has been conducted.

However, practical uses of nanoparticles are limited not only by difficulty to separate them from the solution after completion of reactions, but also a strong tendency to agglomerate into larger particles leading to decrease in photocatalytic activity. These problems can render cost-ineffective, because of the loss of catalyst and most importantly, it can be harmful to health if nanoparticles of heavy metal are released to the environment.

In order to avoid these problems, many studies on modifying and improving photocatalyst have been conducted. One of many techniques is using thin film [1-3] in which the catalyst is formed into film composing of nanoparticles, but the drawback of this technique is significant loss in surface area. Another technique is using granules or pellets containing nanoparticles [4]. In spite of being easily captured, it is not suitable for photocatalyst because the limit of light to penetrate into the pellets making the inner part of the pellet inactive. A few obstacles are overcome by another interesting technique that is the photocatalyst in form of nanofibers consisting of nanosized grains. The small diameter of fiber and nanometer scale of grains offer same benefits of nanoparticles, i.e., enhancement of its surface-to-volume ratio promoting the photocatalytic activity, while the length of the fiber reaching several hundreds of micrometer or millimeter leads to an easy separation. In recent years, a lot of researches have been conducted to fabricate the ceramic nanofibers in many ways. A simple way successfully demonstrated to fabricate

ceramic nanofibers is the combination of sol-gel process with elecrospinning technique. Experimental results have also reported the photocatalytic activity of the nanofibers in comparison to the nanoparticle [5]. Unfortunately, most semiconductor photocatalysts are brittle by nature. Therefore, the ceramic nanofibers are inevitably crumbled into powder after repeated uses and ultimately give the same problems as mentioned previously.

Such a dilemma can be overcome by introducing a polymer core into nanofibers structure to enhance the flexibility of the fibers, hence the fibers can retain their advantages of being nanofibers toward photocatalysis. It can be achieved by using co-axial electrospinning of polymer and precursor of the semiconductor material as core and sheath parts of the fibers, respectively. As a primary study, polyarylonitrile (PAN) is a polymer extensively used in electrospinning, and its nanofibers are good precursors for preparing carbon nanotube. Consequently, it is believed that the property of PAN could be selected as a core polymer and poly vinyl pyrrolidone (PVP) solution containing ZnO sol as a sheath to fabricate the co-axial nanofibers. PAN/ZnO core/sheath nanofibers can be easily separated from solution, and thereby the flaws arising due to the use of photocatalysts in forms of either fine-powdered or ceramic nanofibers can be overcome.

This research focuses on the fabrication of flexible ZnO nanofiber to be used in practical process. The fabrication of the flexible co-axial electrospinning, the

morphology, crystalline phase and structure of polymer after calcination along with the use of the nanofibers in photodegradation will be investigated.

CHAPTER II

THEORY AND LITERATURE REVIEWS

This chapter is the theory and the survey of several studies involving electrospinning technique, sol-gel process, zinc oxide nonofibers and zinc oxide as a photocatalyst. Section 2.1 discusses the properties of materials. Section 2.2 explains sol-gel process. Section 2.3 and 2.4 explain electrospinning and co-axial electrospinning method, respectively. Zinc oxide photocatalytic degradation process and the factors affecting the activity are described in section 2.5

2.1 Properties of Materials

2.1.1 Zinc oxide (ZnO)

Zinc oxide is a II-VI compound semiconductor. The crystal structures shared by zinc oxide are wurtzite, zinc blend, and rocksalt, as schematically shown in Figure 2.1. At ambient condition, the thermodynamically stable phase is wurtzite. The zinc-blende structure can be formed only by the growth of ZnO on cubic substrate. The rocksalt structure may obtain at relatively high pressure.
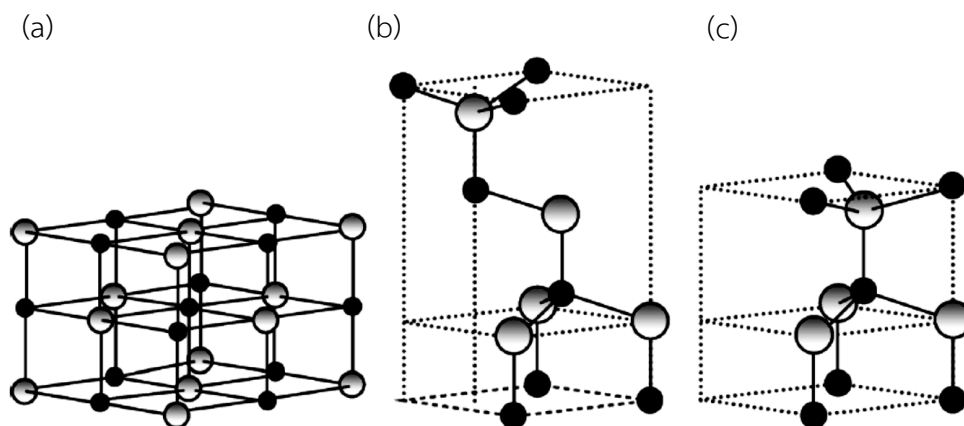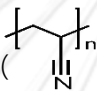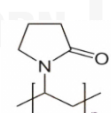
Figure 2.1 Stick and ball representation of zinc oxide crystal structures: (a) cubic rocksalt, (b) cubic zinc blende, and (c) hexagonal wurtzite. (The shaded gray and black spheres denote Zn and O atoms, respectively).

The hexagonal wurtzite structure has two lattice parameters i.e., a=0.32495 nm and c=0.52069 nm (a/c=1.602). The lack of a center of symmetry in wurtzite, combined with large electromechanical coupling, results in strong piezoelectric and pyroelectric properties of ZnO. Consequently ZnO can be used in mechanical actuators and piezoelectric sensors. In addition, ZnO is a direct wide band-gap (~3.3 eV at 300 K) [6] compound semiconductor that is suitable for short wavelength optoelectronic applications. The high excition binding energy (60 meV) of ZnO crystal can ensure efficient excitonic emission at room temperature. Room temperature ultraviolet (UV) luminescence has also been reported in disordered ZnO nanoparticles and thin film.

ZnO is a versatile functional material that has a diverse group of morphologies, such as nanocombs, nanorings, nanohelixes/nanosprings, nanobelts, nanowires and nanocages and nanofibers. Nanostructured ZnO materials have received broad attention due to their distinguished performance in electronics, optics and photonics [7]. In this study, ZnO was synthesized in form of nanofibers to be one-dimensional (1D) photocatalyst.

2.1.2 Poly acrylonitrile (PAN) and Poly vinyl pyrrolidone (PVP)

Polyacrylonitrile ( ) is extensively used in electrospinning as they are good precursors for preparing carbon nanofibers and carbon nanotubes. The common solvents for preparing PAN solutions often have poor volatile properties, such as N,N-dimethylacetamide (DMAc),dimethyl sulfoxide (DMSO), N,N-dimethylformamide (DMF) and NaSCN aqueous solution. Thus in this study PAN was selected as the polymer core and DMF was taken as the solvent for both the sheath and the core fluids.

Poly vinyl pyrrolidone (PVP) ( ) is a thermoplastic. High molecular weight PVP has been used as a polymer media in zinc oxide sol preparation to increase the viscosity of sheath solution in order to spin the fiber via the electrospinning. Table 2.1 shows the thermal properties of PAN and PVP.

Table 2.1 The thermal properties of PAN and PVP.

Polymer	Glass transition temperature (^{0}C)	Crystalline melting temperature (^{0}C)	Decomposition temperature (^{0}C)
PAN	140	318 [8].	350-500 [9].
PVP	175 [10].	150-180	410 [11], 250-420 [12].

2.2 Sol-gel process

Sol-gel technology has found increasing applications in development of new materials for catalysis, fibers, and ceramic industry. The motivations for this method are primarily the potentially high purity, homogeneity, the lower processing temperature comparing with traditional glass melting or ceramic powder method. The relatively economic benefits of sol-gel method are summarized by Mackenzie and T.K Tseng [13, 14].

By applying the sol-gel process, it is possible to fabricate advanced materials in broad variety of forms, e.g. ultra-fine or spherical shaped powders, thin film coatings, fibers, microporous membranes, monolithic materials and porous aerogel materials as shown in Figure 2.2.
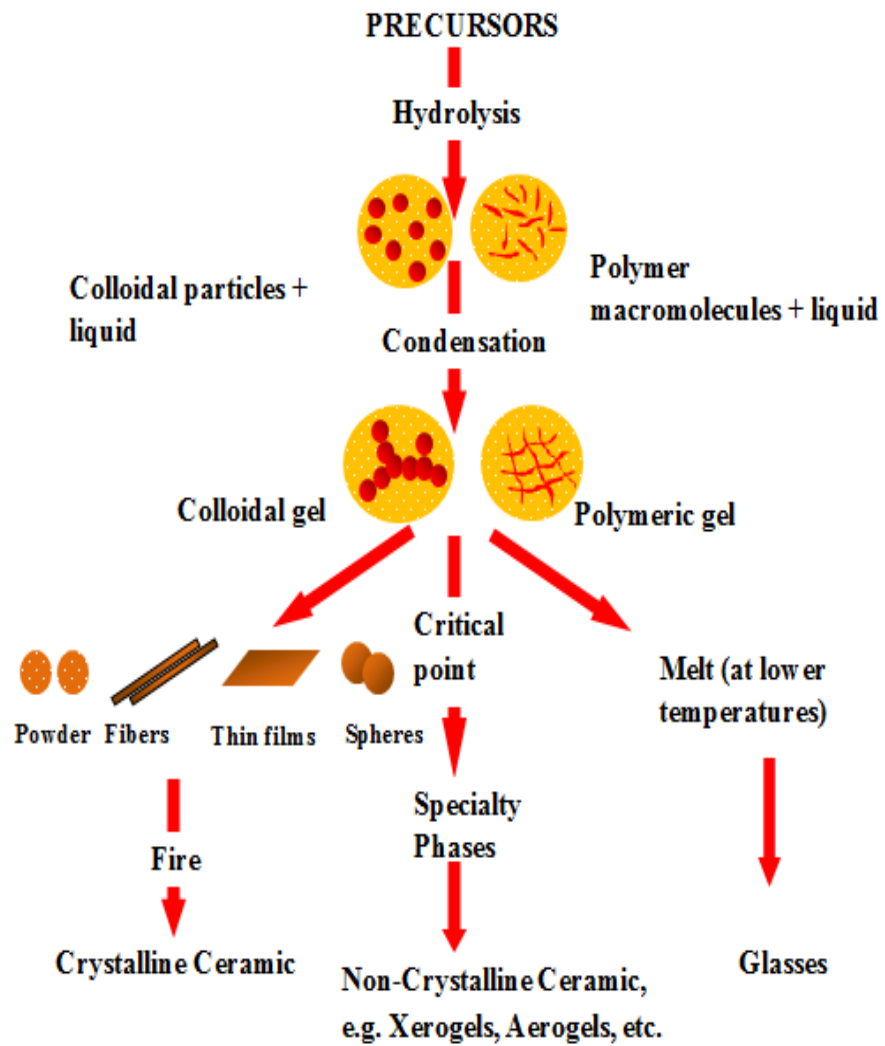
Figure 2.2 Simplified chart of sol-gel process for ceramic materials [15].

2.2.1 Hydrolysis and Polycondensation

Hydrolysis and polycondensation reactions play significant role for sol-gel process. The precursor in sol-gel processes can either be metal salt/alkoxide dissolved in suitable solvent or stable colloidal suspension of preformed sols. Usually, alkoxides are used as starting compounds, that is, organometallic substances of the form $M(OR)_n$ (M: metal of valence n, R: alkyl group C_xH_{2x+1}). By two groups of reaction, i.e., hydrolysis and condensation, the alkoxides are converted to three-dimensionally connected network. The following reactions will take place

Hydrolysis: $\qquad M(OR)_n + nH_2O \longrightarrow M(OH)_n + nR(OH)$ $\qquad$ (1)

Water Condensation: $\qquad M(OH)_n \longrightarrow M\,O_{n/2} + (n/2)\,H_2O$ $\qquad$ (2)

Alcohol Condensation: $M(OR)_n + M(OH)_n \longrightarrow 2M\,O_{n/2} + nR(OH)$ $\qquad$ (3)
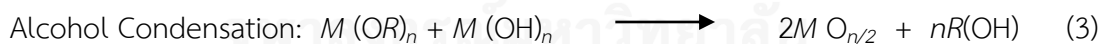
These equations are simplified. In fact, the reactions are much more complicated, especially because the hydrolysis occurs in successive steps. Furthermore, the condensation reaction already started before the hydrolysis is completed. The major important variables are: (I) temperature, (II) nature and concentration of electrolyte (acid, base), (III) nature of solvent, (IV) type of alkoxide

precursor, i.e., an increase of the R ratio (mole of water/mole of precursor) induces hydrolysis reaction (k_H) to increase but for some range [16]. Because both hydrolysis and condensation are nucleophilic displacement reactions, the reactivity of metal alkoxides depends on the positive charge of partially charged metal atom and its coordination number. As general rule, the longer and the bulkier the alkoxide group, the slower the rate constant.

Table 2.2 addresses issues relating to the main chemical systems used for undoped ZnO thin films elaboration by sol-gel process.

Table 2.2 Main chemical systems used for undoped ZnO thin films elaboration by sol-gel process.

Year	Authors	Zinc acetate dihydrate (mol/ml)	solvent	Additive ([additive]/[Zn2+])	Water ([H2O]/[Zn^{2+}])	Aging time (h)	heat treatment (^{o}C)	main crystallographic orientation
1998	Gonza'lez et al.	0.59	Methanol	-	-	24	300,450	(002)
1999	Nagase et al.	0.6	2-Methoxyethanol	Monoethanolamine (1)	-	-	Laser irradiation	(002)
2006	Wang et al.	0.5	Ethanol	Diethanolamine (1)	-	-	400-800	(101)
2006	Ghosh et al.	0.6	2-Propanol	Dimethylamine	-	-	550	(101)
2006	Choi et al.	0.5	2-Methoxyethanol	Monoethanolamine (1)	-	-	400-700	(002)
2007	Sagar et al.	0.6	Methanol	Monoethanolamine (0-1)	-	48	400-600	(002)
2008	O'Brien et al.and Rao et al.	0.3-0.7, 1.3	2-Propanol	Monoethanolamine (1)	-	24	450-650	(002)
2008	Hsieh et al.	0.6	2-Methoxyethanol	Monoethanolamine (1)	-	-	600-900	(002)
2008	Yoon et al.	0.5	2-Methoxyethanol	Monoethanolamine (1), Diethanolamine (1)	-	72	700	(002)
2008	Srinivasan et al.	0.5	2-Methoxyethanol	Monoethanolamine (1)	-	-	500, 450-600	(002)
2009	Lin and Kim	0.5	2-Propanol	Diethanolamine (1)	-	24	450-550	(101)
2003	Basak et al.	0.6	2-Propanol	Dimethylamine	-	-	550	(002)
2008	Liu et al.	0.6	Ethanol, Polyetylene glycol	Diethanolamine (1),	2	-	500	(101)

2.3 Electrospinning

Electrospinning method has been widely studied due to its economical aspect, efficiency, simplicity for mass production of nanostructured materials and applicability to manufacture fibers.

Electrospinning depends on the complex interplay of polymer science, electrical engineering, mechanical engineering, material engineering and rheology. The basic components include a power source capable of forming a large electric field, a counter electrode, a viscous solution, and means of pumping the solution. The main forces acting on the viscous solution are gravity force, external force, surface tension, and electrical force. The electrical forces acting in opposition to the surface tension of the fluid in order to create the Coulomb repulsion between the charged ions that favors the fabrication of specific shape called "Taylor cone". Once a charged jet start to emanate from the apex of the Taylor cone when the applied electrical potential is increased to a sufficiently high value. The charged jet will remain stable for a certain distance called "instability region" which is specific to each solution and electrical configuration. While the jet travels toward to collector, the solvent evaporates or the polymer solidifies and randomly deposited as a non-woven on the collector.

Rultledge et al. explained the in-depth about predicted theory of the two types of instability mode of charged jet, namely a "varicose instability" in which the jet's centerline remains straight but the jet's radius is modulated and "whipping instability" in which the jet's radius is constant but the centerline is modulated. Whipping instability causes decrease in diameter of the fibers and the jet is further decreased in diameter by solvent evaporation [17].

The dominant instability strongly depends on the following important factors of electrospinning:

- Fluid parameters of the jet (viscosity, dielectric constant, vapor pressure, conductivity) and also the static charge density on the jet. In particular, for high conductivity fluid, when there is no static charge density on the jet, the varicose mode dominates the whipping mode. On the other hand, when there is a large static charge density, the whipping mode dominates.

- The power supply should be adequate to overcome the viscosity and surface tension of fluid.

- The gap between the tip of the nozzle and grounded surface should not be too small to prevent a spark between the electrodes, yet it should be large enough for the evaporation of solvent to form the fibers deposited on the collector.

Another problem encountered in the electrospinning is the morphological defects such as beads. It has been found that the polymer concentration also affects the formation of the beads. Many studies recognized that high polymer concentration results in fewer beads and higher aspect ratio [18, 19] (Figure 2.3 (a)). The applied voltage also results in beads morphology and aspect ratio (Figure 2.3 (b)). In general, the aspect ratio increases first due to increasing applied voltage giving rise to higher electrostatic repulsion force, hence making the bead size smaller [18, 20]. With increasing the tip-to-collector distance (Figure 2.3 (c)), beads becomes larger. When the applied voltage is constant, the electrostatic force will be decreased as the tip-to-collector distance increases. As a result, drawing stress on the jet is decreased. The aspect ratio decreased with the tip-to-collector distance [18].
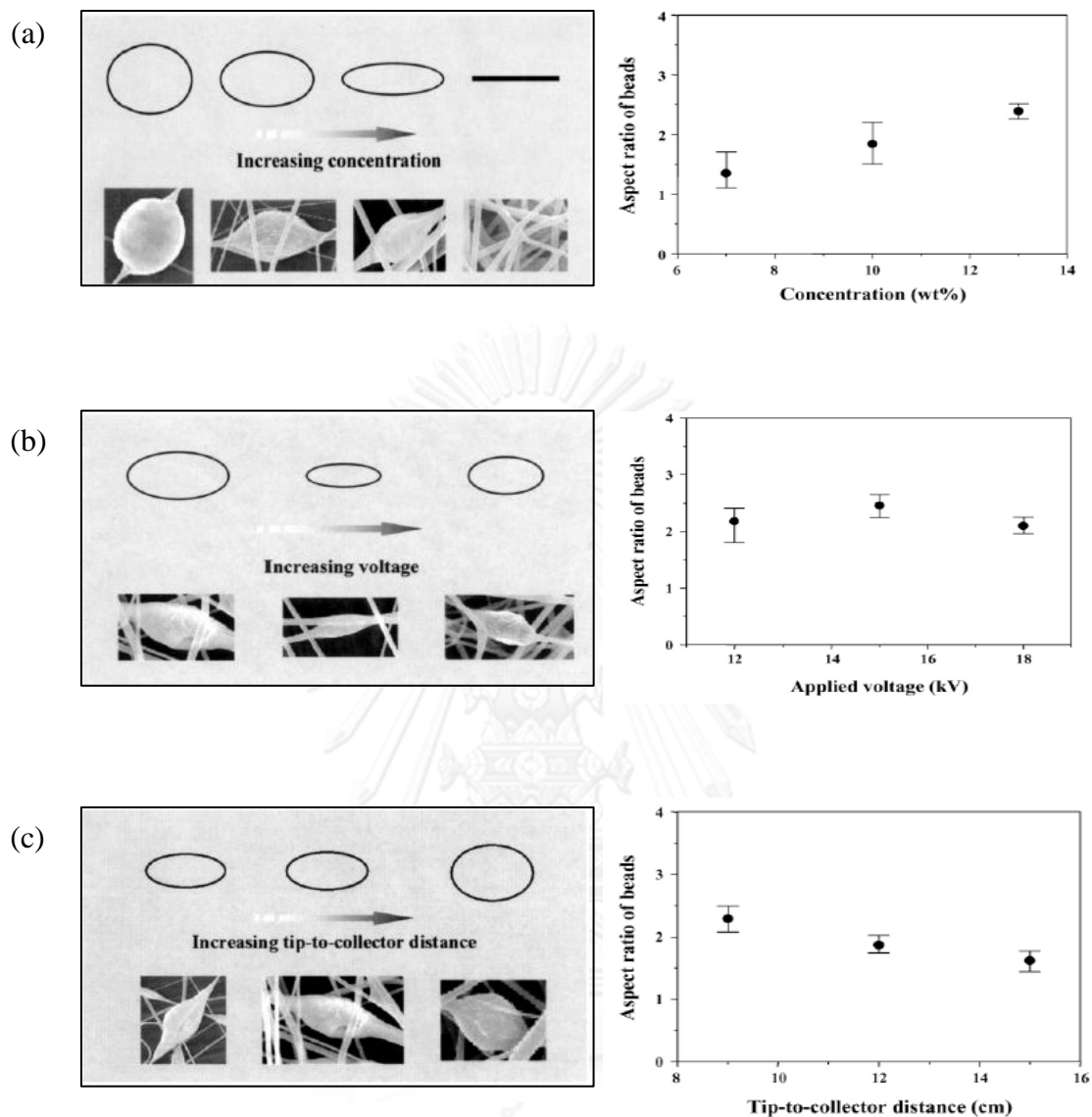
Figure 2.3 The change of bead morphology and the aspect ratio with (a) the polymer concentration (PS dissolve in the mixture of THF/DMF fixed applied voltage at 15 kV, TCD=12 cm), (b) the applied voltage (Fixed concentration at 13 wt. %, TCD=12 cm), and (c) the tip-to-collector distance (TCD) (Fixed concentration and applied voltage of 13 wt. % and 15 kV respectively) [18].

The scaling law on fiber formation during electrospinning was proposed to predict the different morphologies such as pure beads, beaded fibers, and pure fibers as a function of solution properties. It was calculated and measured based on an entanglement number diagram reporting that using PVP Mw=1,300k. Fibers initiation was predicted to commence at 4 wt.% while only fibers should be obtained for PVP concentration $\geq$ 7.5 wt.% . Between these two concentration limits, a mixture of fibers and beads was predicted [21, 22].

Yang et al. studied the influence of solvent on the formation of PVP fibers with electrospining. They proposed that a lower tension and higher viscosity, leading to the formation without the beads. [23].

In this study, PVP was chosen as the polymer for sheath solution, while PAN (Mw~150,000) was chosen as the core polymer. The literature reviews of the PVP and PAN nanofibers formation via electrospinning are summarized in Table 2.3 and Table 2.4, respectively.

Table 2.3 Literature reviews of the PVP electrospinning.

Year	Authors	PVP (wt%)	Solvent	Tip diameter (mm)	Distance (cm)	Flow rate (ml/h)	Voltage (kV)	Average fiber diameter (nm)
2006	Eryun Yan et al.	4	Ethanol/chloroform	0.6	20	-	17	401-600
2007	Wang et al.	4, 6, 8	Ethanol	0.8	15	0.5	13	245 - 420
2007	Qiang Zhao et al.	6	1,2-dichloroethane/chlorobenzene	0.6	20	-	17	smooth fiber
2008	J. Bai et al.	8	Water/ethanol (2/8)	0.6	16	-	15	300-350
2011	G. Chang, J. Shen	10	Ethanol	0.05	15	-	15	coiled microfibers (ribbons formed)
2011	P. Kongjumnean et al.	18-20	Deionized water	-	10	-	10, 12, 14, 16	2800-7500
2011	M. Miyauchi et al.	10.7	2-propanol	0.94	18	3.6	10.0-12.0	200
2012	M. Dai et al.	15	0.01 mg/mL HRP/aqueous solution	-	12	0.1	20	155 ± 34
2013	Waseem S. Khan et al.	15	Ethanol	0.3	15-25	1.0-3.0	18-20	-
2013	Wahyudiono et al.	4	Dichloromethane	0.75	8	3	17	4110 ± 2000
				0.5	8	3	17	4930 ± 1020
				0.25	8	3	17	2280 ± 380

Table 2.4 Literature reviews of the PAN electrospinning.

Year	Authors	PAN (wt%)	Solvent	Tip diameter (mm)	Distance (cm)	Flow rate (ml/h)	Voltage (kV)	Average fiber diameter (nm)
2005	S.Y. Gu et al.	10	DMF	-	10	-	20	206
2008	J.-H. He et al.	9 12 15 18	DMF	7	8	2.8	20	90 210 275 380
2009	D. Zhang et al.	6.5 6.5 6.5 10 6.5	DMF	0.6	19 10	0.24	15 10 20 15 20	250 153 300 500 500
2009	P. Heikkila et al.	13	DMF	0.4	15	0.4	28	270
2010	Y. Cai et al.	12	DMF	0.3	15	0.4	14	200-400
2010	W. Pan et al.	7	DMF	0.5	17	1	14	270
2011	J. Zhu et al.	8 10 12 14	DMF DMF DMF DMF	0.8	15	0.6	20	300 600 800 1100
2013	Y. Ou et al.	15	DMF	-	5	0.7	16	420-490

Nicole et at. reported the effect of collector geometry, particularly for alignment of fibers. Rotating collector such as mandrels or disks, as well as electrodes separated by a gap, are facile ways to generate oriented fibers [24]. Unaligned or randomly oriented fibers are conventionally collected on a static substrate, such as grounded metal plate. Researchers have explored the use of conductive grids or series of charged needles to guide the collection of fibers along the charged regions. Figure 2.4 shows a diversity of collectors and their effect on the nanofibers mat pattern [25].
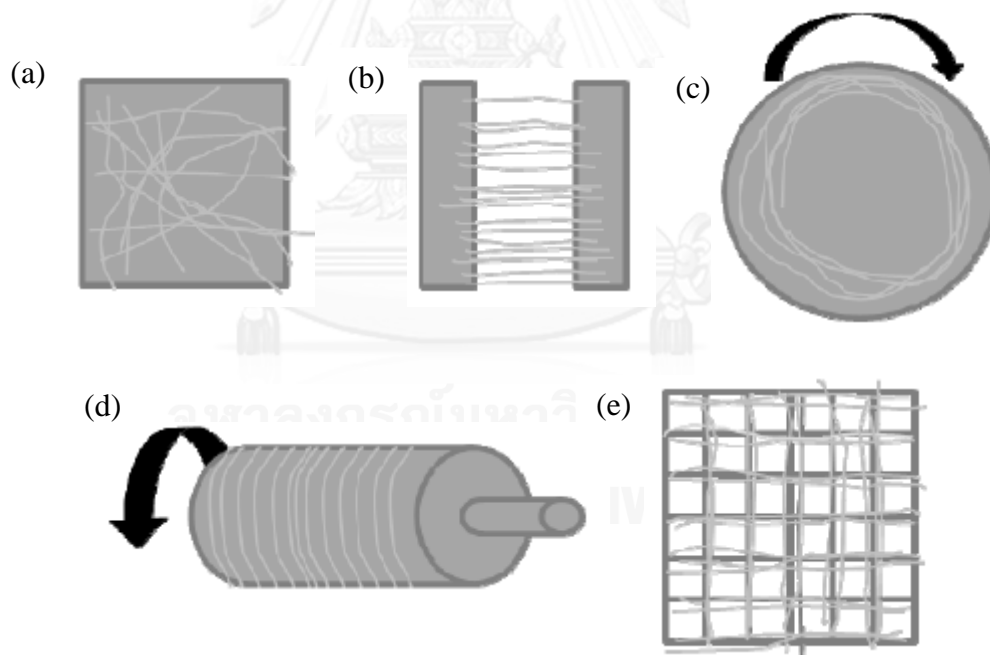

Figure 2.4 Different collector geometries for electrospinning; (a) static plate, (b) parallel electrodes, (c) rotating disk, (d) rotating mandrel, (e) grid [25].

2.4 Co-axial electrospinning

Core-sheath nanofibers configuration are typically two dissimilar fibers consisting of core of one material type and an encapsulating shell of another material. It can be achieved by using co-axial electrospinning. Co-axial electrospinning is conceptually akin to that of the single jet electrospinning. The electrically driven bending instability should originate from the same origin as in the case of single fluid jet and should be qualitatively similar to the single-fluid electrospinning [26].

A modification is made in the concentric spinneret by inserting a smaller capillary, connected to the one holding the core solution that fits concentrically inside the bigger capillary, attached to the reservoir containing the sheath solution, to make co-axial configuration (Fig 2.5). The feeding rates of the solutions are controlled using either metering pumps or air pressures.
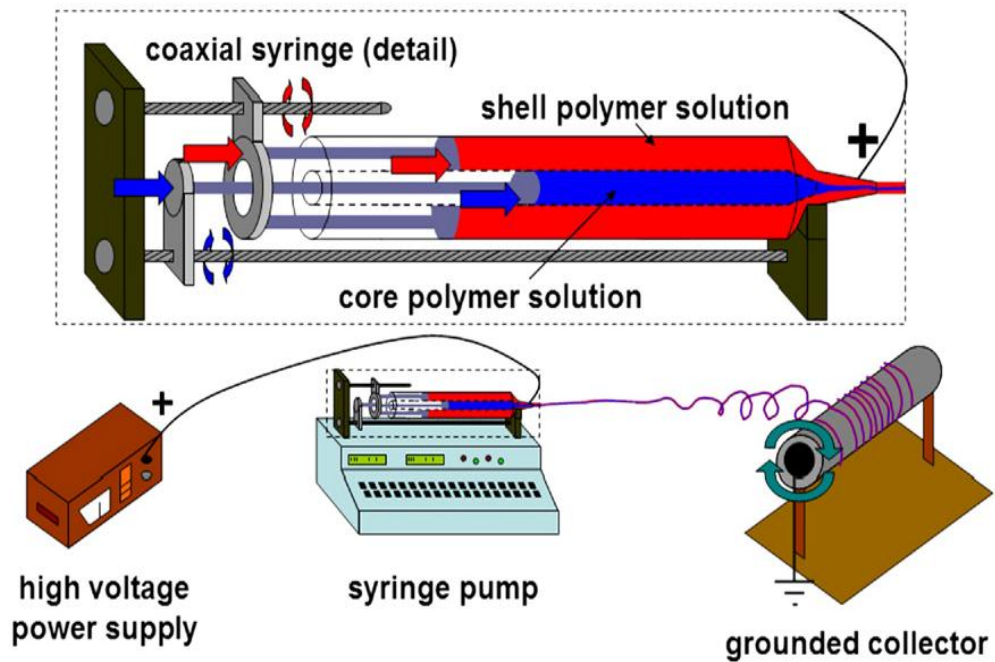
Figure 2.5 Schematic of co-axial electrospinning set-up [27].

The core and sheath material are delivered independently through a co-axial capillary forming compound droplet. The compound droplet is charged after high voltage is supplied. Charges are induced predominantly on the surface of sheath fluid. When the charges approach to the threshold value due to the higher applied potential, the jet emanates from the droplet. Rapid stretching of the sheath can cause strong viscous stress, which will transfer to the core, which can be made from a low viscosity fluid [26]. Tangential to the jet line, the shear stress will stretch the core. This causes the core liquid to deform into the conical shape, which is consequently stretched and elongated it along with the sheath via "viscous

dragging" and "contact friction" [28] (Fig 2.6). It is expected that as long as the compound cone is stable, the core is uniformly incorporated into the sheath for core-sheath fibers formation [29].
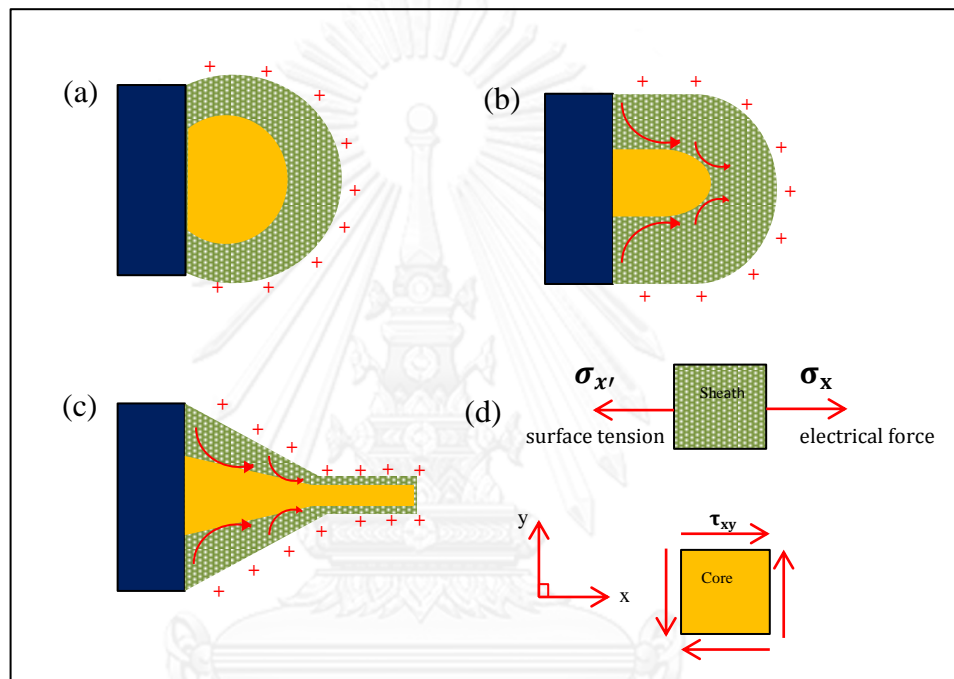
Figure 2.6 Schematic illustration of compound Taylor cone formation

(a) surface charges on the sheath solution,

(b) viscous drag exerted on the core by the deformed sheath droplet,

(c) Sheath-core compound Taylor cone formed due to continuous viscous drag

(d) Morh circle performs principle stress and shear stress

On the way to the collector, the jet gradually gets longer and thinner due to bending instability, simultaneous evaporation of the solvent. Then polymer solidifies and randomly deposited on the collector. Factors affecting co-axial electrospinning depend on material parameters and process parameters.

I)   Material parameters

Solution viscosity

It was reported that in the co-axial electrospinning process, sheath solution acts as a guide and surrounds the core material. A sufficiently high viscosity of sheath solution such that the viscous stress imparted by it on the core solution needs to overcome the interfacial tension between the two solution in order to from the compound Taylor cone and jet. Accordingly, the viscosity of sheath solution is critical and the sheath polymer selected should be electrospinnable by itself [30, 31]. From the studies available, it appears that the requirements for the spinnability of the core solution by itself are not as critical as they are for the sheath material. The viscosity of core solution should not to be too low to avoid varicose breakup, leading to the sprayed and/or the segmented morphology [32].

Solution concentration

In a single fluid electrospinning, increase in solution concentration yields an increase in the fiber diameter because of higher constant of material in the jet. A similar effect has been observed in the case of co-axial electrospinning.

Zhang et al. found that increasing the core concentration resulted in an increase not only in core size but the overall fiber diameter as well. [33]. Similarly, He et al. observed an increase in the overall fiber diameter when sheath concentration is increased while core concentration is maintained constant [34].

Solvent/Solution miscibility and incompatibility

There are some criteria for selecting core and sheath materials for elctrospinning. First of all, for successful spinning, the solvent in either of the solutions should not precipitate the polymer from the other solution when the solutions meet at the tip of the capillary. Secondly, the interfacial tension between the sheath and the core should be as low as possible for generate the stable compound Taylor cone.

Divergences on the issue of miscibility of the sheath and core solution have been reported. Sun et al. proposed that the diffusion at the boundary of core and sheath takes longer time than that of the electrospinning process and therefore, no mixing takes place [35]. Yu et al. indicated that the same solvent would reduce the

interfacial tension between core and sheath solutions, resulting in smooth interface of core and sheath parts [30]. However, Li and Xia reported that mixing could be occurred in co-axial electrospinning process in which two solutions are miscible [28].

Solvent vapor pressure

The type of solvent used, in particular in the core solution, can also have a strong effect on the resulting co-axial fiber morphology. Li et al. reported that the solvent with high vapor pressure (e.g. chloroform, acetone etc.), created a thin layer at the interface between the sheath and the core when it is used in the core due to rapid evaporation [36].

Since the stabilized compound Taylor cone and the initial jet are requirements for the co-axial electrospinning, higher vapor pressure may not be used in the sheath solution because they may produce unstable Taylor cone and lead to multiple jets due to fast evaporation [37].

Solution conductivity

Conductivity difference between the core and the sheath solutions can also affect the fiber formation. Yu et al. have found that more conductive core solution was pulled at a higher rate by the applied electric field and caused discontinuity in the core-sheath structure. Higher sheath conductivity, on the other hand, would not hinder the process but would result in higher shear stress on the core material and

subsequent elongation to form a thinner core. It is clear that even non-conductive or less conductive liquids can be successfully incorporated as the core into a higher conducting sheath [30].

II)   Process parameters.

Applied voltage

Moghe et al. found the existed a small range of applied voltage in which a stable compound Taylor cone was formed (Fig 2.7 (b)). This range varied with the type polymer used. Voltage below the critical range caused dripping of two solution followed by an intermittent jet from the sheath (Fig 2.7 (a)) with an occasional incorporation of core. Voltage above the critical range caused the strength of the electric field to exceed that required for the given material and process conditions and Taylor cone tended to recede and the jets tended to emanate from inside the capillaries resulting into separate jets from the sheath and core solutions (Fig 2.7 (c), 2.8) and no core-sheath structure formed [29].
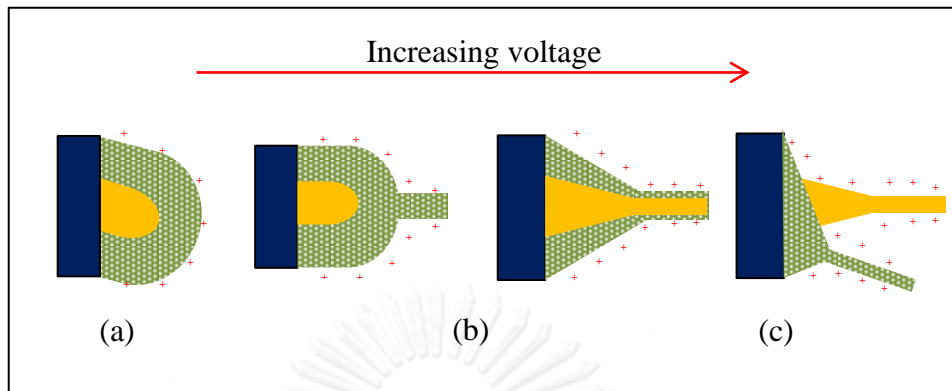
Figure 2.7 Schematic of the voltage dependence of the core-sheath fiber formation in co-axial electrospinning ; (a) subcritical, (b) critical, and (c) supercritical voltage.
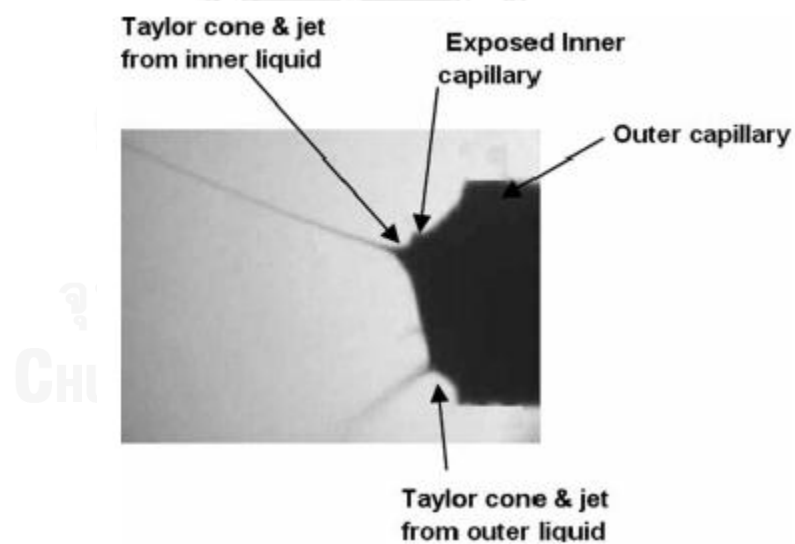

Figure 2.8 Separate fluid jets formed at supercritical voltage.

Solution flow rates

It was reported that if the core flow rate is too low, the core was unsuccessfully incorporated in the sheath owing to the insufficiency of solution delivered. The too high core flow rate, on the other hand, would not render the core-sheath structure because the size of the core liquid Taylor cone increase to the point that resulting the viscous drag applied by sheath solution is insufficient to confine the core solution within the cone. It concluded that the core flow rate should be lower than that of the sheath [29].

Chakraborty et al. reported that the ratio of flow rates between the core and sheath solutions profoundly affects the quality of the co-axial electrospinning product. At flow rate ratio less than 1:2 (core: sheath), there is insufficient shell solution to encapsulate the core. For increased shell flow rate ratios between 1:2 and 1:3, encapsulation of the core solution occasional takes place, although most of the product formed in this condition remains as solution-mixture droplets. Flow rate ratio between 1:3 and 1:6 allows the formation of stable core-sheath Taylor cones. Further increase in the sheath flow rate (1:7 to 1:10) does not change the capability of core-sheath solution to be electrospun, but reduces the encapsulation efficiency of core solution [27] (Fig 2.9).
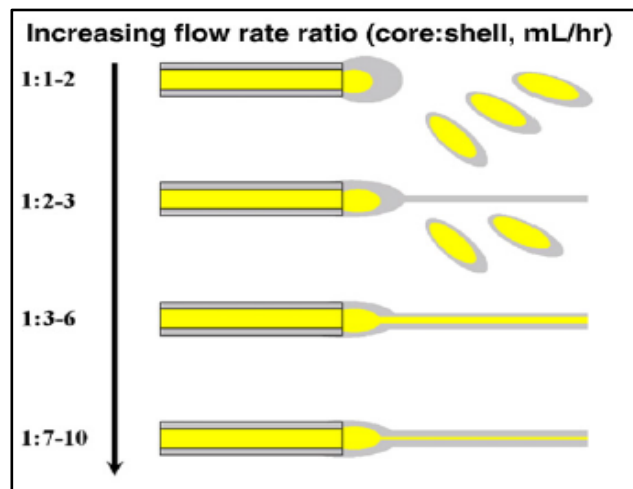
Figure 2.9 An illustration of effect of different flow rate ratios in the encapsulation of core solution [27].

Distance between the tip of the nozzle to collector

The distance from tip of nozzle to the collector can be called "working distance". It directly affects the strength of electric field in the process. Therefore, the decrease in working distance, which means higher electric filed strength, could result in smaller diameter of fibers.

Table 2.5 addresses issues relating to the fabrication and uses of this technique.

Table 2.5 List of studies using co-axial electrospinning

Year	Authors	Core	sheath	Solvent		Applications
				Core	sheath	
2003	Sun et al.	polydodecylthiophene (PDT)	PEO	Chloroform	Chloroform	protective clothing, filter and biomedical applications
2005	Song et al.	FePt	Poly (ε-caprolactone)(PCL)	hexane	2,2,2-trifluoroethanol(TFE)	magnetic nano-device
2005	H.Jiang et al.	Poly(ethylene glycol) (PEG)	Poly (ε-caprolactone)(PCL)	DI water mixing protein	DMF/chloroform	controlled release of protein and tissue engineering
2006	J.E. Diaz et al.	hydriphobic liquid	PVP	-	DMF	controlled encapsulation of hydrophobic liquid in hydrophilic polymer nonofibers in various biological or medical applications
2008	G. Chang et al.	PVP/ silver nanoparticles	PVP/ titanium n-butyloxide	ethanol	acetic acid/ethanol	photocatalysis
2009	Choi et al.	. Polyvinyl-acetate (PVAc)	ZnO	DMF	-	hollow ZnO fibers senser
2010	M. Miyauchi et al.	MWNTs	Cellulose	(. 1-Ethyl-3-methylimidazolium acetate)[EMIM][Ac]	(. 1-Ethyl-3-methylimidazolium acetate)[EMIM][Ac]	conductive cable fibers with insulating surface

Table 2.5 List of studies using co-axial electrospinning (continued)

Year	Authors	Core	sheath	Solvent		Applications
				Core	sheath	
2012	L. Liu et al.	EPDM	PVP	EPDM/BPO	DMF	brittle plastics toughening, and applications in extremely high or low temperatures
2011	D. Han et al.	PEO	DFPase	DI water	DFPase	controllable drug release systems
2011	D.-G. Yu et al.	PAN	LiCl	N,N-dimethylacetamide (DMAc)	N,N-dimethylacetamide (DMAc)	encapsulating drugs, biological agents, and fabricating polymeric microtubes
2012	X. Li et al.	Oil	LaCl3+PVP	Oil	ethanol/acetic acid	catalyst supports, luminescentmaterials, and gas sensors
2012	H. Kriel et al.	poly(L-lactic acid) (PLLA)	poly(D,L-lactic acid) (PDLLA)	DCM/DMF	DCM/DMF	tissue engineering and drug release applications

2.5 Photocatalytic degradation

2.5.1 Principle of heterogeneous photocatalytic

For classical heterogeneous catalysis, the overall process can be decomposed into five independent steps: (1) Transfer of the reactants in the fluid phase to the surface, (2) Adsorption of a least one of reactants, (3) Reaction in the adsorbed phase, (4) Desorption of the product(s), (5) Removal of the products from the interface region. The photocatalytic reaction occurs in the adsorbed phase (step 3). The only difference between conventional catalysis and photocatalytic is the mode of activation of catalyst of which the thermal activation is replaced by a photonic activation.

When the semiconductor catalyst is illuminated with photons whose energy is equal to or greater than their band-gap energy E_g $(h\nu \geq E_g)$. There is adsorption of these photons and creation within the bulk of electron-hole pairs, which separate into free photoelectrons in the conduction band (CB) and photoholes in the valence band (VB) ,(Figure 2.10).
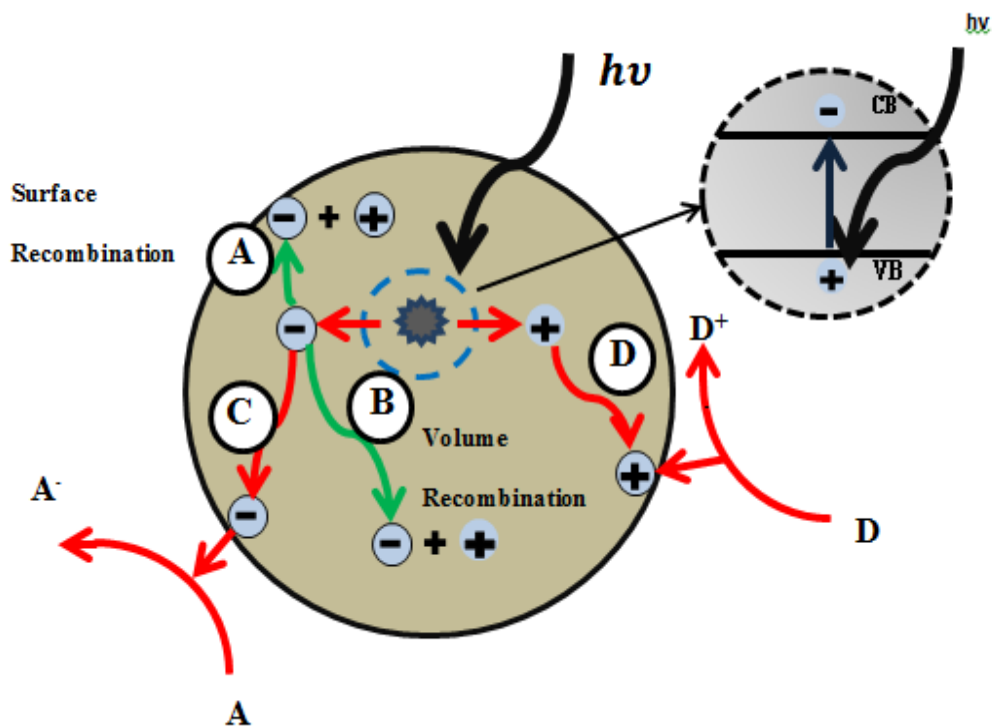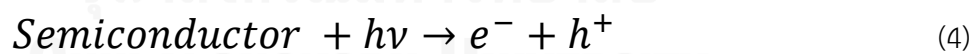
Figure 2.10 Schematic diagram; overall process of semiconductor photocatalysis in an aqueous system

$$Semiconductor \; + h\upsilon \rightarrow e^- + h^+ \tag{4}$$

$$A(ads) + e^- \rightarrow A^-(ads) \tag{5}$$

$$D(ads) + h^+ \rightarrow D^+(ads) \tag{6}$$

In the presence of a fluid phase as a media, e.g. gas phase, pure organic liquid phase, or aqueous solution, a spontaneous adsorption occurs and according to the

redox potential of each adsorbed species, an electron transfer proceeds towards acceptor molecules (usually oxygen in a solution) as shown in pathway C in Figure 2.13 and Equation 5. Simultaneously, positive photoholes are transferred to donor molecules pathway D in Figure 2.13 and Equation 6. In competition with charge transfer to adsorbed species, there is electron and hole recombination. It can occur both in the volume of the semiconductor (pathway B) and on the surface (pathway A). The efficiency can be reduced by the electron-hole recombination, described in Fig 2.13 and Equation 7, which corresponds to the degradation of the photoelectric energy into heat.

$$e^- + h^+ \rightarrow N + E \tag{7}$$

where N is the neutral center and E is the energy released under the form of light or heat. It is reported that surface and bulk defects naturally occurring during the synthesis may help suppress the recombination by trapping charge carriers.
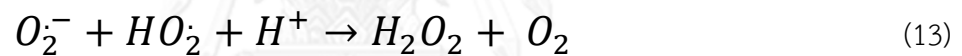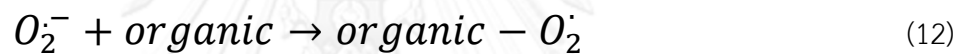
For ZnO as a heterogeneous photocatalyst, once excitation occurs across the band gap, it creates electron-hole pair to undergo charge transfer as following in Eq.8.

$$ZnO + h\nu \rightarrow e^- + h^+ \tag{8}$$

The photoholes produced by irradiation reacts with water (Eq.9) or surface-bound hydroxyl ion (Eq.10) producing hydroxyl radical (very reactive hydroxyl radicals).

$$h^+ + H_2O \rightarrow H^+ + OH^. \tag{9}$$

$$h^+ + OH^- \rightarrow OH^. \tag{10}$$

Electron released by irradiation of photocatalyst combines with dissolved molecular oxygen, producing the superoxide radical, $O_2^{.-}$ (Eq.11). This radical, in the presence of organic scavengers, may form organic peroxides (Eq.12) or hydrogen peroxide (Eq.13).

$$e^- + O_2 \rightarrow O_2^{.-} \tag{11}$$

$$O_2^{.-} + organic \rightarrow organic - O_2^. \tag{12}$$

$$O_2^{.-} + HO_2^. + H^+ \rightarrow H_2O_2 + O_2 \tag{13}$$

The photoholes in the valence band are also responsible for the production of hydroxyl radical, which have been indicated as the primary cause of degradation (Eq.14).

$$OH^- + Organic \rightarrow degradation\ of\ the\ organic \tag{14}$$
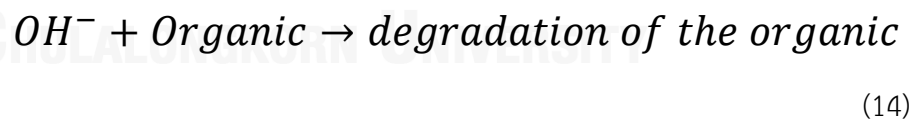
The efficiency of the photocatalytic process can be measured as a quantum yield, which is defined as the number of defined events occurring per photon absorbed by the system or as the mole of reactant consumed or product formed per amount of photon absorbed. The ability to measure the actual absorbed light is practically not

feasible in heterogeneous systems due to scattering of light by semiconductor surface and the recombination. It is usually assumed that all the light is absorbed and the capacity is quoted as an apparent quantum yield. The quantum yield for an ideal system $(\emptyset)$ can be given by the simple relationship [38]:

$$\emptyset \propto \frac{k_{CT}}{k_{CT}+k_R} \tag{15}$$

where k_{CT} is the charge transfer process rate and k_R is the electron-hole recombination rate.

There are five major physical parameters governing the kinetics of photocatalytic reaction in and aqueous system [39] : (A) mass of catalyst which was found to be directly proportional to the mass m of catalyst (Fig 2.11). This indicates a true heterogeneous catalytic regime, however, above a certain value of m, the reaction rate levels off and becomes independent of m. (B) wavelength; the variations of the reaction rate as a function of the wavelength follows the absorption spectrum of catalyst, with a threshold corresponding to its band gap energy. In order for ZnO to be photocatalytically reactive, at least UV-A is required. (C) initial concentration of reactant (Figure 2.11) , (D) temperature; due to photonic activation process, the systems does not require heating and they are operated at a low temperature range (20°C to 80°C). At very low temperatures below 0°C or at very high temperature above 80°C, the photocatalytic activity decreases. Thus a

photocatalytic experimental setup required air coolers for the optimum temperature.

and (E) radiant flux; the photocatalytic reaction rate is proportional to the radiant

flux ,ϕ, and this confirms the photo-induced nature of activation of the catalytic

process, with the participation of photo-induced electrical charges to the reaction

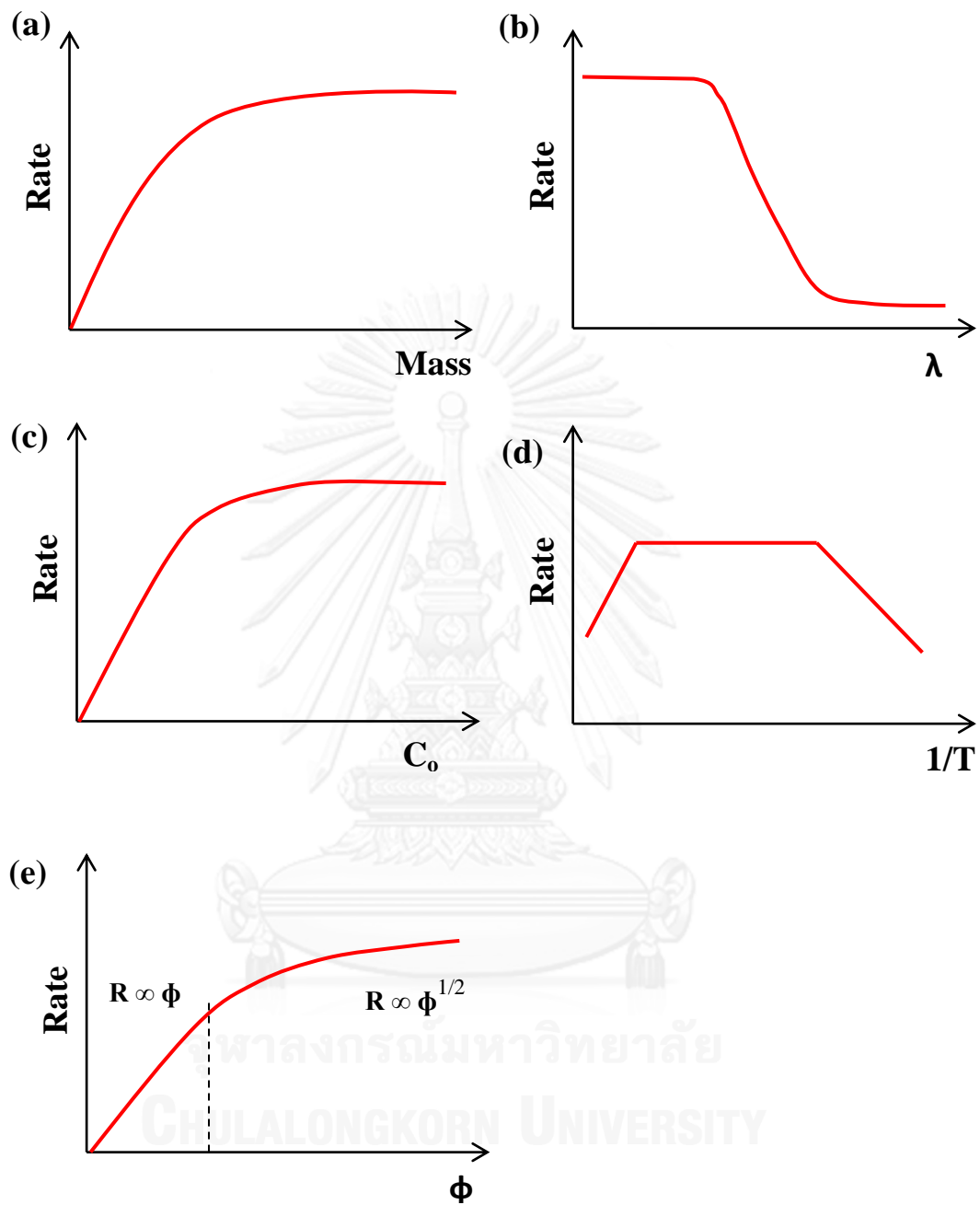mechanism. However, above a certain point, the reaction rate becomes proportional

to $\phi^{1/2}$.

Figure. 2.11 Influence of the different experimental parameters which govern the reaction rate r; (a) amount of catalyst, (b) wavelength , (c) initial concentration of reactant, (d) temperature, and (e) radiant flux [39].

The UV-A, wavelength of 400-315 nm, was selected for photocatalytic reactions with UV irradiation.

In this study, the reduction in the concentration of the dye molecule was determined with the absorbance value at the maximum of the absorption spectrum at 664 nm for every dye by monitoring UV-Vis spectrum in 400-800 nm

To investigate photocatalytic efficiency of each photocatalytic material, it was assumed that the absorption intensities of UV-Vis data were linearly propotional to the dye concentration.

$$\text{Degradation (\%)} = \frac{C_0 - C}{C_0} \times 100 \qquad (16)$$

Where C_0 the initial dye concentration and C is the dye concentration after the treatments as concentration unit, mgL^{-1}

The rates of photocatalytic oxidation over illuminated ZnO are often fitted to the Langmuir-Hinshelwood (L-H) kinetics model which:

$$r = \frac{dC}{dt} = \frac{kKC}{1+KC} \qquad (17)$$

Where r is the oxidation rate of the reactant (mg/Lmin), C is the concentration of the reactant (mg/L), t is the irradiation time, k is the reaction rate constant (mg/Lmin), and K the adsorption coefficient of reactant (L/mg).

The Langmuir-Hinshelwood model represents a mechanism for surface catalysis in which the reaction occurs between species that are adsorbed on the surface. When the chemical concentration C_0 is small the equation can be simplified to an apparent first-order equation. In general the first-order kinetics is appropriate for the entire concentration range up to few ppm. The L-H model has been established to describe the dependence of the observed reaction rate on the initial solute concentrations.

$$ln\left(\frac{C_0}{C}\right) = kKt = k_{app}t \tag{18}$$

The expression for the rate of photomineralization of organic substrates such as dyes with irradiated TiO_2 follows the L-H law for five possible situations; (a) photocatalytic reactions must be initiated by photoabsorption, (b) excited electron and hole are formed, (c) electrons and holes react with surface adsorbed species, (d) otherwise recombine each other to give no chemical reaction but heat, (e) if any chemical or photoinduced reaction(s) follows, its kinetics must be included. However, it is not possible to say whether the process takes place on the surface in solution or at the interface [40].

Bhatkhande et al. summarized the compounds that can be degraded such as, aliphatic, inorganic, aromatic, and surfactants dyes [41].

CHAPTER III

EXPERIMENTAL METHODOLOGY

The aim of this chapter was to elucidate the experimental methodology for fabrication Polyacrylonitrile (PAN)/zinc oxide (ZnO) nanofibers and photocatalytic degradation of Methylene blue. It is divided into four parts: materials used preparation of flexible PAN / ZnO coaxial nanofibers, characterizations of products and photocatalytic degradation process.

3.1 Materials

List of the chemicals employed in this work are illustrated in Table 3.1

Table 3.1 List of chemical agents used in the research.

Chemical agents	Using for	Manufacturer/ Grade
1. Zinc acetate $(CH_3COO)_2Zn.2H_2O$	Synthesis of ZnO sol	Ajax Finechem, 99.5%
2. Diethanolamine (HOCH2CH)2NH	Synthesis of ZnO sol	Ajax Finechem, 98.5%
3. N,N'-dimethylformamide (DMF) ,$(CH_3)_2NC(O)H$	Solvent	Sigma-Aldrich
4. Water H_2O	Synthesis of ZnO sol	-
5. Hydrochloric acid HCl	Synthesis of ZnO sol	J.T.Baker,37.7%
6. Methylene blue $C_{16}H_{18}N_3ClS.2H_2O$	substrate of degradation	Ajax chemicals
7. Poly vinyl pyrolidone (PVP), Mw~1,300,000	Polymer sheath of co-axial fibers	Sigma-Aldrich
8. Poly acrylonitrile (PAN), Mw~150,000	Polymer core of co-axial fibers	Sigma-Aldrich

3.2 Preparation of flexible PAN / ZnO coaxial nanofibers

3.2.1 Electrospinning Apparatus

The schematic of co-axial electrospinning apparatus is shown in Figure 3.1.
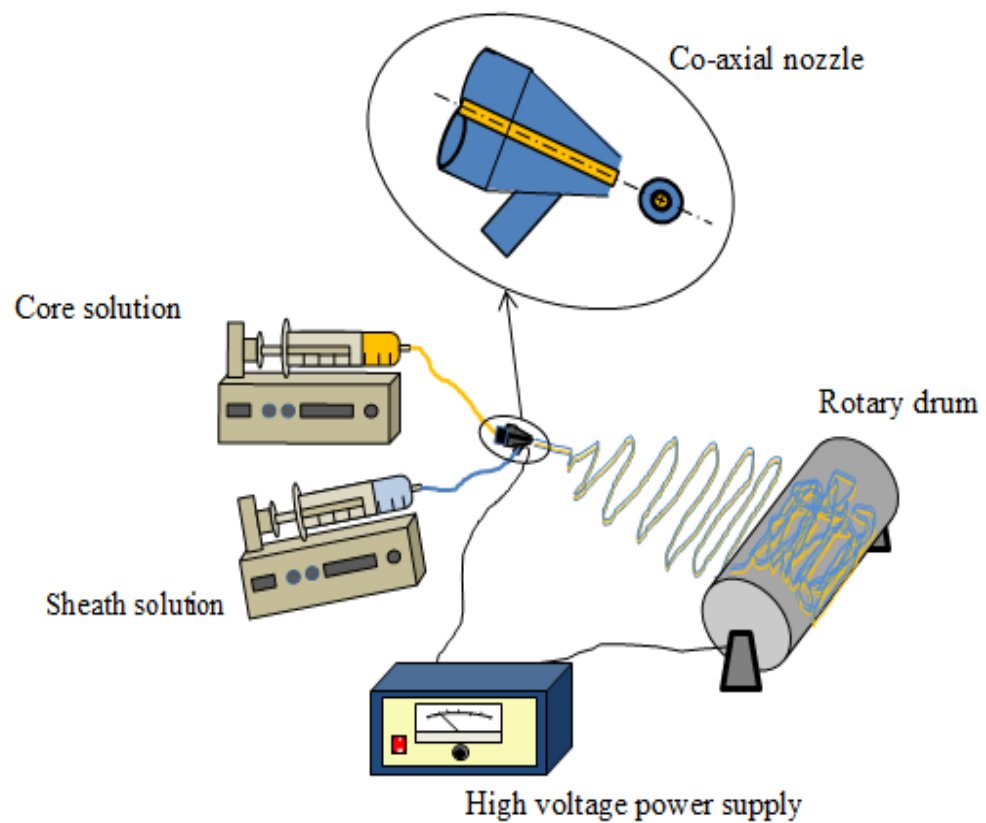
Figure 3.1 Schematic of co-axial electrospinning set-up

The components of the apparatus and their functions are described as follows

- A high voltage power supply (Gamma, High Voltage Research) was used to generate either positive or negative DC voltage up 50 kV, with very low electrical current.

- A co-axial copper nozzle of which the core diameter is equal to that of the stainless needle (gauge number 22, the outer diameter of 0.7 mm) and outer diameter of the sheath is 1.5 mm will be attached to two syringes for producing co-axial fibers.

- Two 10 ml syringes and pump were used as containers for eletrospinning solutions. The syringes are made from plastic and set in horizontal orientation.

- The rotary drum diameter of 17 cm (equipped with 60 KTYZ synchronous motor, 220 VAC 50/60 Hz, 30 RPM 14W).

- Aluminum foil wrapping the rotary drum was considered to be a ground collector.

3.2.2 Preparation of electrospinning solutions

The polyacrylonitrile (PAN) core solution was prepared by dissolving PAN (Mw=150,000) in N,N'-dimethylformamide (DMF) at 60^0C and stirred for 1h. In this study, the concentration of PAN core solution was varied to investigate the effect of concentration.

On the other hand, ZnO sol for sheath solution was prepared by using 3.29 g of zinc acetate and polyvinylpyrolidone (PVP), Mw~1,300,000 in various amount to be dissolved in 20 ml DMF and stirred to get the precursor solution. A mixture of 0.26 ml distilled water, 0.18 ml HCl and 1.58 ml diethanolamine in 5 ml DMF was dropped into the precursor solution and continuously stirred for 2 h to achieve a transparent ZnO sol.

3.2.3 Co-axial electrospinning process

Each electrospinning solution was filled into each plastic syringe, which was furnished into the co-axial nozzle. The PAN syringe connected to the core of nozzle and the other connected to the shell of the nozzle contained PVP/ZnO solution for producing PAN-PVP/ZnO core-sheath fibers. The grounding electrode from the same power supply was attached to a piece of aluminum foil wrapping on the rotary drum as the collector placed in front of the tip of the nozzle. The coaxial electrospinning process was initiated when electric field strength of 1 kV/cm (25 kV and 25 cm to the collector drum) was applied. The flow rate of 0.8 ml/h was maintained for both core and sheath solutions. It took 6 h to collect nanofibers in each batch. In addition the fibers were left for complete evaporation of solvent for 24 h.

3.2.4 Calcination of the PAN-PVP/ZnO core-sheath fibers

The calcination of electrospun products were placed in a box furnace. The temperature of furnace was raised from room temperature to 450°C, 500°C and 550°C with heating rate of 10°C/min, then holding for 2 hours.

3.3 Characterizations of products

3.3.1 Scanning electron microscopy (SEM)

The morphology of the obtained product was determined by scanning electron microscopy (SEM, Jeol JSM-6400). In addition, the composition of fibers was investigated by energy dispersive x-ray spectroscopy (EDX) at Scientific and Technological Research Equipment Centre Foundation (STREC), Chulalongkorn University.

3.3.2 Transmission electron microscope (TEM)

The core-sheath structures of PAN-PVP/ZnO co-axial nanofibers before and after calcination were investigated by using transmission electron microscopy at Faculty of engineering, Chulalongkorn University and National Nanotechnology Center (NANOTEC).

3.3.3 Rheometer

The viscosities of the solutions were measured by using cone and plate type viscometer (BROOKFIELD, DV-II+Pro) at Center of excellence in particle technology (CEPT), Faculty of engineering, Chulalongkorn University.

3.3.4 Thermogravimetric analysis (TGA)

The decomposition temperature and thermal behavior of the obtained products were studied by using thermogravimetric analysis on a Mettler-Toledo TGA/DSC1 STARe System at Center of excellence in particle technology (CEPT), Faculty of engineering, Chulalongkorn University. The samples were heated under the oxygen flow of 40 ml/h heated from $25^{o}C$ to $1,000^{o}C$ under ramp rate of $10^{o}C/min$.

3.3.5 Fourier-transform infrared spectroscopy (FT-IR)

A Fourier transform infrared spectrometer (Nicolet 6700) at Center of excellence in particle technology (CEPT), Faculty of engineering, Chulalongkorn University was used to investigate the functional group in the products. The sample of the product was mixed with KBr in a ratio of sample to KBr 1:10 before measurement.

3.3.6 X-ray diffraction analysis (XRD)

The crystalline phase of the synthesized photocatalyst (ZnO) is analyzed by X-ray diffraction (XRD, *Bruker* AXS *D8 Advance*) using CuK$_\alpha$ radiation of wavelength 1.5406 Å at 40 kV in the range of 2Θ = 20° – 70°. The crystallite size of the synthesized product was estimated from the full-width at half-maximum (FWHM) of the (101) diffraction peak according to the Debye-Scherrer equation.

$$D = \frac{k\lambda}{\beta\cos\theta} \qquad (19)$$

Where *k* is a constant equal to 0.9, λ is the X-ray wavelength; β is the full width at half maximum and θ is the half diffraction angle.

3.3.7 Universal testing machine (UTM)

The tensile strength of the fiber products was measured by Universal Testing Machine (UTM) (Hounsfield H 10 KM) at Scientific and Technological Research Equipment Centre Foundation (STREC), Chulalongkorn University. The films of fibers were cut into a dimension of 1x3 cm^2 in width and length, respectively. The thickness of the films is control by the electrospinning time of 6 h. The specimens were pulled with the rate of 10 N/min while measuring.

3.3.8 Brunauer-Emmett-Teller (BET) analyzer

The surface area of synthesized products was analyzed by using Brunauer-Emmett-Teller (BET) analyzer (BEL model BELSORP-mini, Japan) at Excellence in Particle and Technology Engineering laboratory, Chulalongkorn University. The process was carried out by nitrogen adsorption-desorption at liquid nitrogen temperature (77K).

3.4 Photocatalytic Degradation Process

3.4.1 Photodegradation Apparatus

The schematic of protodegradation apparatus used in this work is shown in Figure 3.2 the components of the apparatus and their functions are described as the follows.
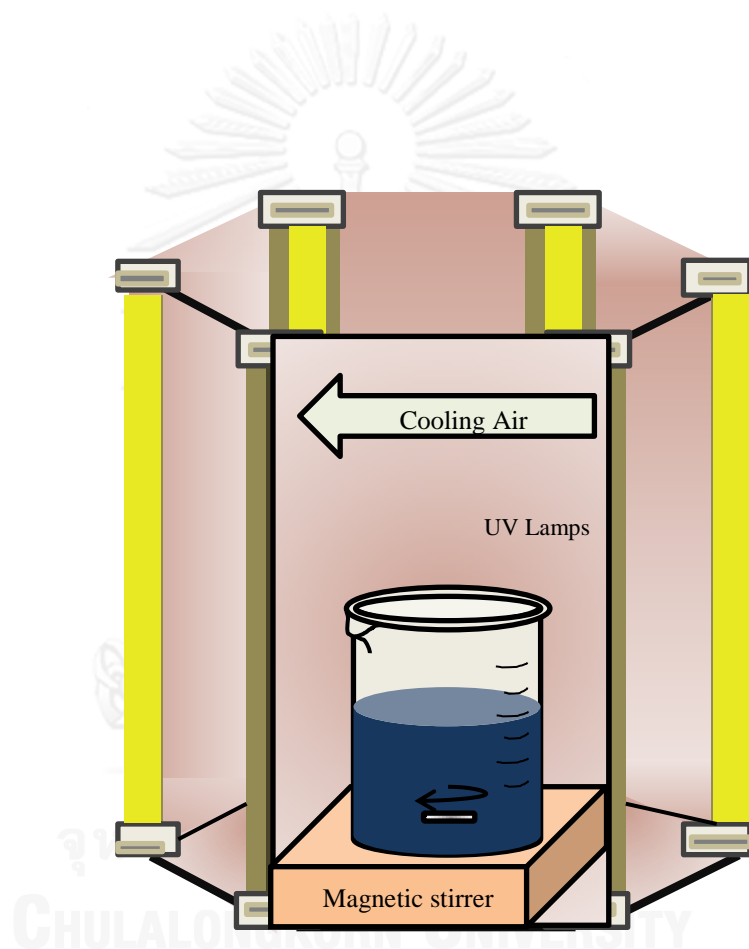
Figure 3.2 Experimental setup for photocatalytic dye degradation

This system is consisting of:

- 6 UV-A lamp (Phillips TLD 15W/05) used as a light source of the photocatalytic reaction.

- A magnetic stirrer used to generate turbulent conditions in mixture during the experiment to keep mixture homogeneous.

3.4.2 Photocatalytic Degradation Procedure

The photocatalytic activity of the PAN- ZnO nanofibers structures was evaluated by degradation of methylene blue (MB) solution under UV irradiation. The content of the co-axial fibers were used equivalent to 1 mg of the catalyst per 10 ml of the solution of 10 ppm of MB solution ($C_{16}H_{18}N_3SCl.3H_2O$). The solution was magnetically stirred in the dark for 30 min to reach the adsorption equilibrium of MB on the surface of catalyst, prior to the reaction. After that, the solution was irradiated with six UV-A lamps (Phillips TLC 15w/05) and continuously stirred by a magnetic stirrer to keep the catalyst uniformly dispersed within the solution. The degradation rate of methylene blue was measured by UV–Vis spectrophotometer (Shimadzu, UV-1700) at the maximum absorption wavelength of MB (664 nm) at 10, 20, 30, 40, 60 and every single hour until the MB degraded completely.
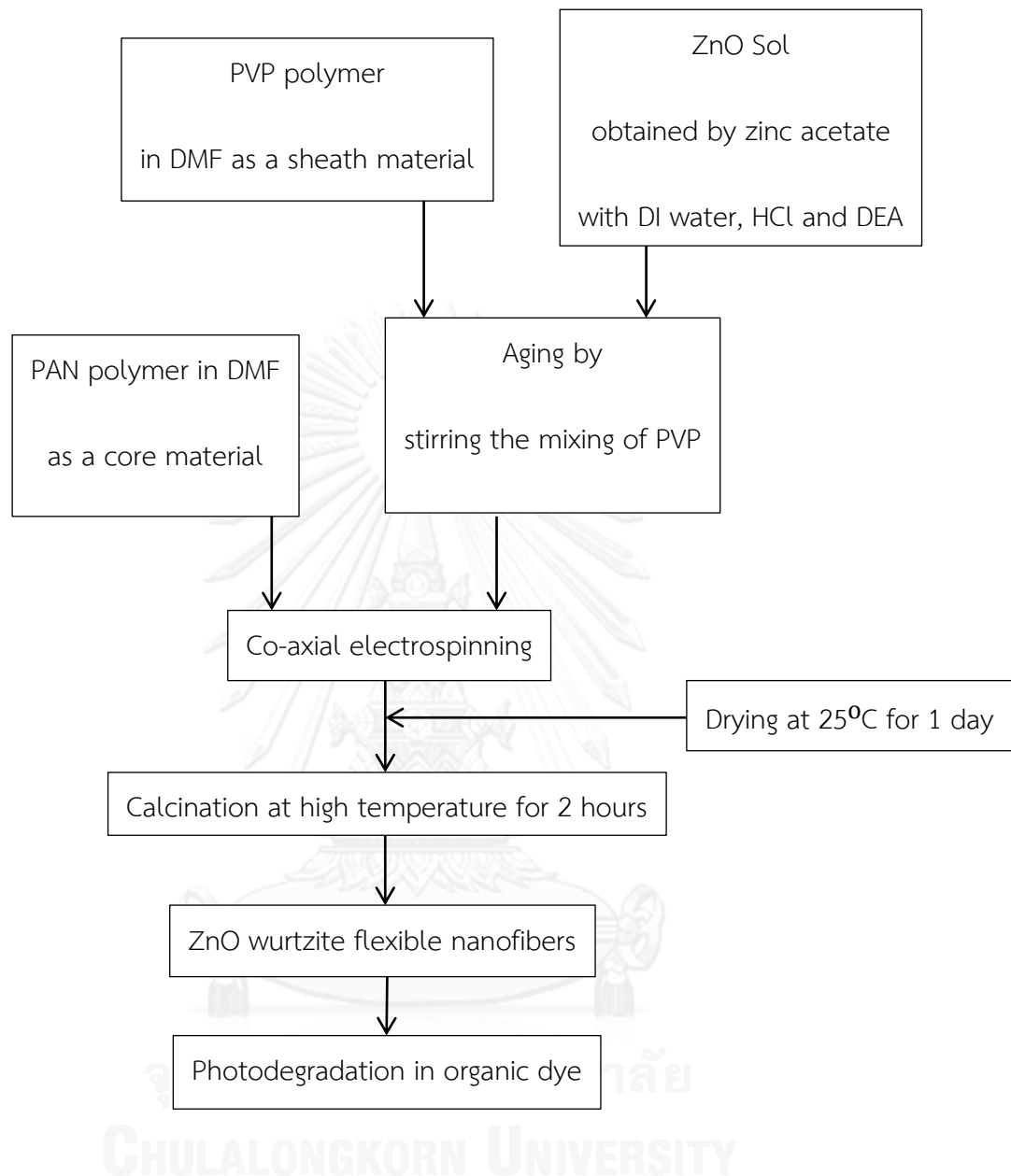
Figure 3.3 Flowchart of synthesis flexible PAN / ZnO coaxial nanofibers and photodegradation process.

3.5 Statistical Analysis

The analysis of variance (ANOVA) was used to determine the significant differences by Bonferroni test. Two–way ANOVA was selected to determine the interaction between the PVP concentration and PAN concentration on average diameter of fibers and mechanical properties of fibers. The data presented in figures are at 95% confidence levels of the fitting values.

CHAPTER IV

RESULTS AND DISCUSSION

Results and discussion are presented in this chapter. The fabrication of ZnO/PAN co-axial nanofibers, core-sheath structure and ZnO nanocrystallites are reported in section 4.1. The ANOVA analysis of the flexibility of fibers products are presented in section 4.2. Furthermore in section 4.3 the photocatalytic degradation test and effects of various parameters such as calcination temperature, calcination time, and aging time are discussed.

4.1 Fabrication of ZnO/PAN Co-axial Nanofibers

4.1.1 Effect of polymer viscosity

There are many factors that play a role in governing successful co-axial electrospining of fibers. One of these is solution viscosity, which is directly controlled by the molecular weight and the solution concentration. Figure 4-1 shows the viscosity of the prepared ZnO sol mixed with PVP at different concentration, as well as that of PAN core solution.
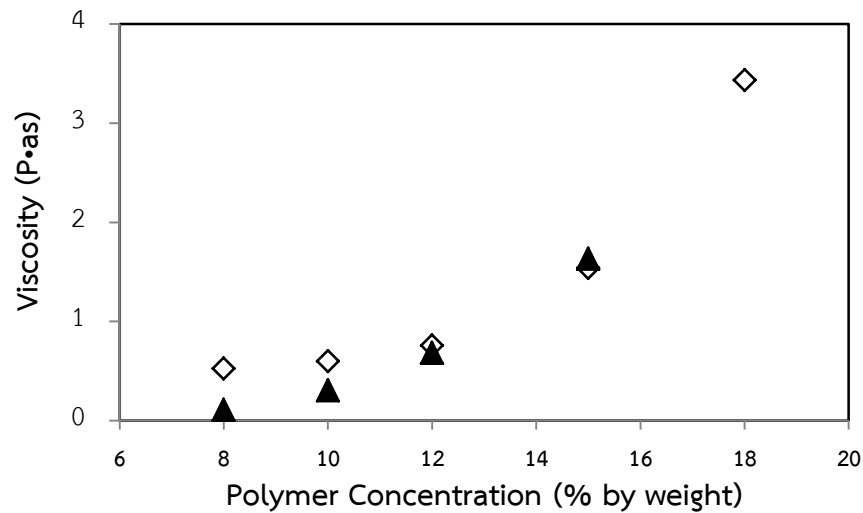
Figure 4-1. Viscosity of ZnO sol mixed with PVP solution (◇) and PAN solutions

(▲) at different polymer concentration (8, 10, 12, 15, and 18% by weight).

The viscosity of sheath solution is required to be higher than the viscosity of core solution[29]. The comparison between the lower and the higher viscosity of sheath than that of core solution in Figure 4-2 (a), it is obviously shown that the lower viscosity of sheath concentration than that of core concentration could not be successfully fabricated the co-axial structure. On the other hand the co-axial structure could be formed using the sheath solution with higher viscosity than that of core solution (e.g., 0.758 Pa.s of PVP sheath / 0.525 Pa.s of PAN core) as shown in Figure 4-2(b). The viscosity of the sheath solution is critical [30, 31]. A sufficiently high viscosity of the sheath solution such that the viscous stress imparted by it on the core solution needs to overcome the interfacial tension between the two solutions in order to from the compound Taylor cone and the subsequent jet [29].
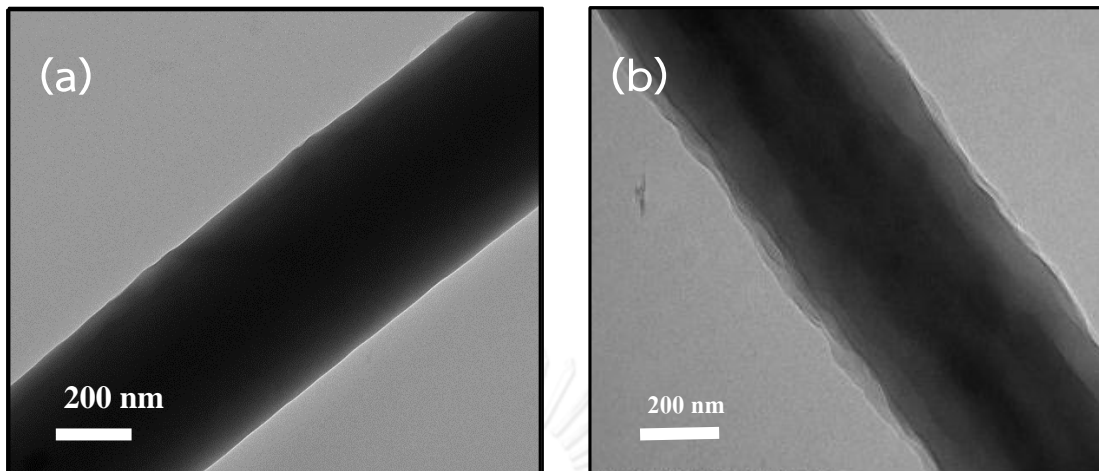
Figure 4-2. The comparison of the co-axial structure between using the sheath

solution (a) with lower viscosity, (b) with higher viscosity than that of core solution

4.1.2 Effect of PVP concentration in sheath solution

It has been reported that PVP fibers (Mw=1,300,000) should be obtained via the

electrospinning if the concentration of PVP in the solution is higher than 7.5 wt.% [21,

22]. In this study, the concentration of PVP in the sheath solution is varied from 8%

to 18% by weight, which corresponds to the viscosity in the range of 0.52 to 3.43 P.as

respectively. As shown in Figure 4-3, the diameter of the fibers trends to gradually

rise as the PVP concentration is increased. It should be noted that the concentration

of PAN in the core solution, the feeding rate and the electric field were fixed at 8

wt%, 0.8 ml/h, and 1 kV/cm respectively. The average diameter of as-spun co-axial

fibers tuned in the range of 403±73 to 516±93 nm. It can also be noted that the

diameter of the fibers tends to gradually rise even though PVP in sheath was

disappear after calcination at 450°C and 500°C, because the interaction factors between the concentration of PVP in sheath and PAN in core resulting to the Taylor cone. From this reason, the diameter of PAN in core may be different even fixed at 8% PAN by weight.
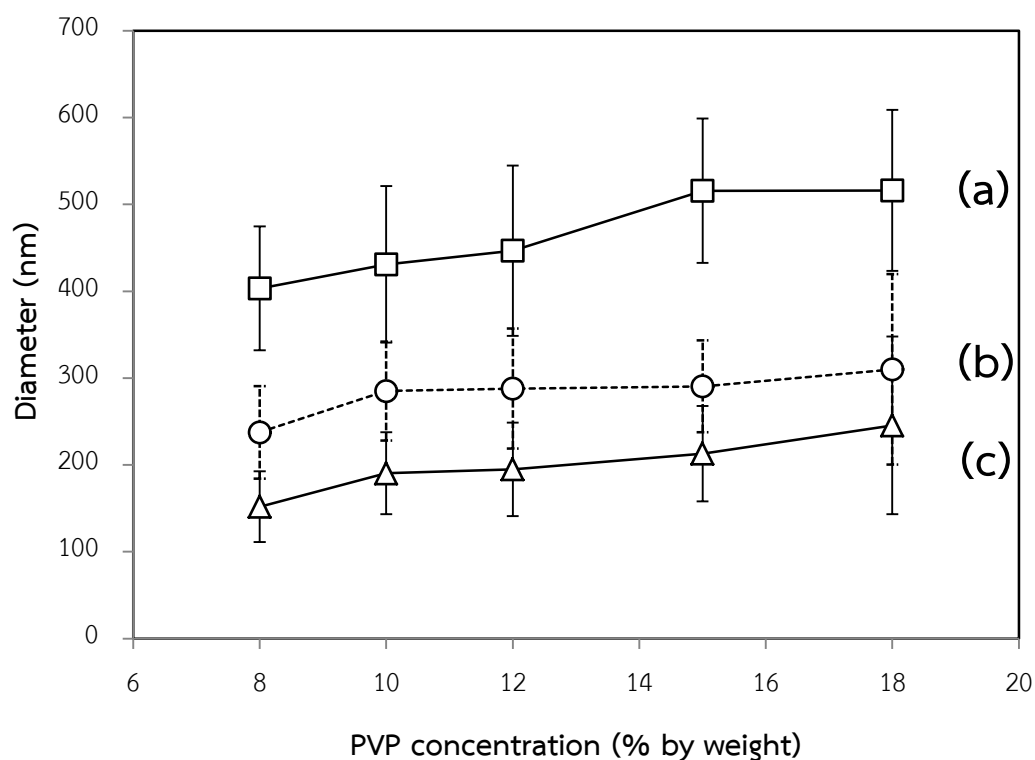
Figure 4-3. The diameters of co-axial nanofibers as the concentration of PVP in sheath solution is varied, while that of PAN in core solution is fixed at 8 wt%: (a) before being calcined, and after being calcined at (b) 450°C, and (c) 500°C.

The average diameter of the fibers is decreased when the fibers are calcined at increased temperature, as shown in Figure 4-3(b,c). The calcined fibers are smaller than the as-spun fibers by about 39% and 57% when the calcination temperature is increased from 450 to 500°C respectively. The shrinkage could be accounted for by considering the loss of PVP from the sheath, **structural changes and deterioration of PAN core.**

The uniform bead-free fibers were produced as shown in Figure 4-4. The size distributions of the fibers are shown in Figure 4-5. Figure 4-6 represents the size distribution of co-axial nanofibers before and after it had been calcined in air at 450°C and 500°C.
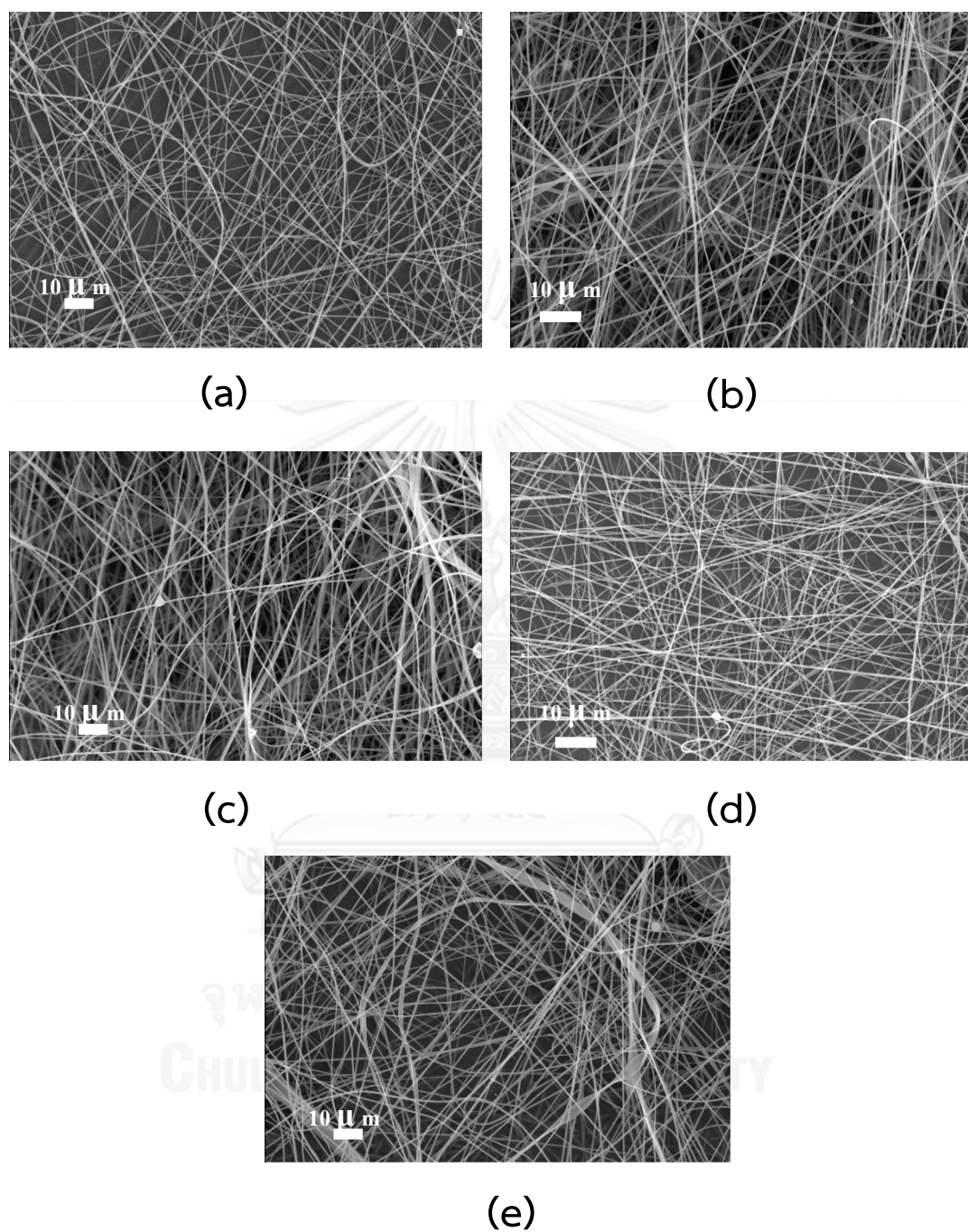
Figure 4-4. SEM images of ZnO/PAN co-axial nanofibers prepared by using PVP concentration of (a) 8%, (b) 10%, (c) 12%, (d) 15%, and (e) 18% by weight after calcination at 450°C. The concentration of PAN in the core solution was fixed at 8%.

Figure 4-5. The size distributions of the nanofibers prepared by using PVP concentration of (a) 8%, (b) 10%, (c) 12%, (d) 15%, and (e) 18% by weight after calcination at 450°C. The concentration of PAN in the core solution was fixed at 8%.
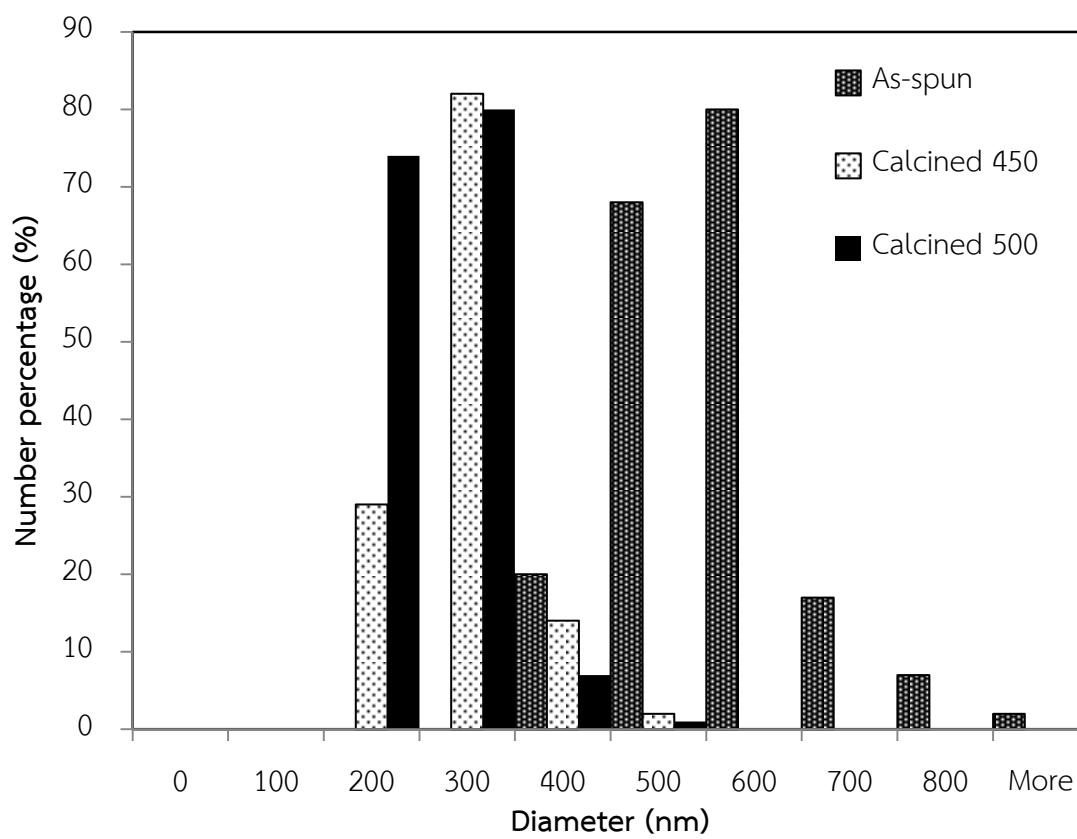
Figure 4-6. Histogram showing the size distribution of co-axial nanofibers before and after it had been calcined in air at 450°C and 500°C.

4.1.3 Effect of PAN concentration in core solution

Furthermore, the important parameter to be considered is the concentration of PAN in the core solution. In this study, the PAN concentration is varied in value of 8, 10 and 12% by weight, which corresponds to viscosity of 0.11, 0.31, and 0.68 Pa•s respectively. The products are smooth fibers (Figure 4-7(c-f)). It is noted that the PAN concentration lower than results in beaded fiber as shown in Figure 4-7(a-b).

The effect of PAN concentration on size of the as-spun fibers is shown in Figure 4-8. As the PAN concentration is increased from 8 to 10%, diameter of the as-spun fibers is gradually increased. The size is sharply risen when the PAN concentration is increased from 10 to 12%. It should be noted that the concentration of PVP in sheath solution, the feeding rate and the electric field were fixed at 12 wt%, 0.8 ml/h, and 1 kV/cm respectively. The average diameter of as-spun co-axial fibers is in the range of 447±98, 866±234, and 3407±816 nm when the PAN concentration used is 8, 10 and 12%, respectively. It should be point out that, when compared with the effect of PVP concentration in the sheath solution shown in Figure 4-3, changing in PAN concentration affects size of the fibers more dramatically.

As shown in Figure 4-9, the fibers also show a significant decrease when the calcination temperature is increased from 450 to 500°C. Fibers shrink about by 30-36% and 56-70% after being calcined at 450 and 500°C respectively.
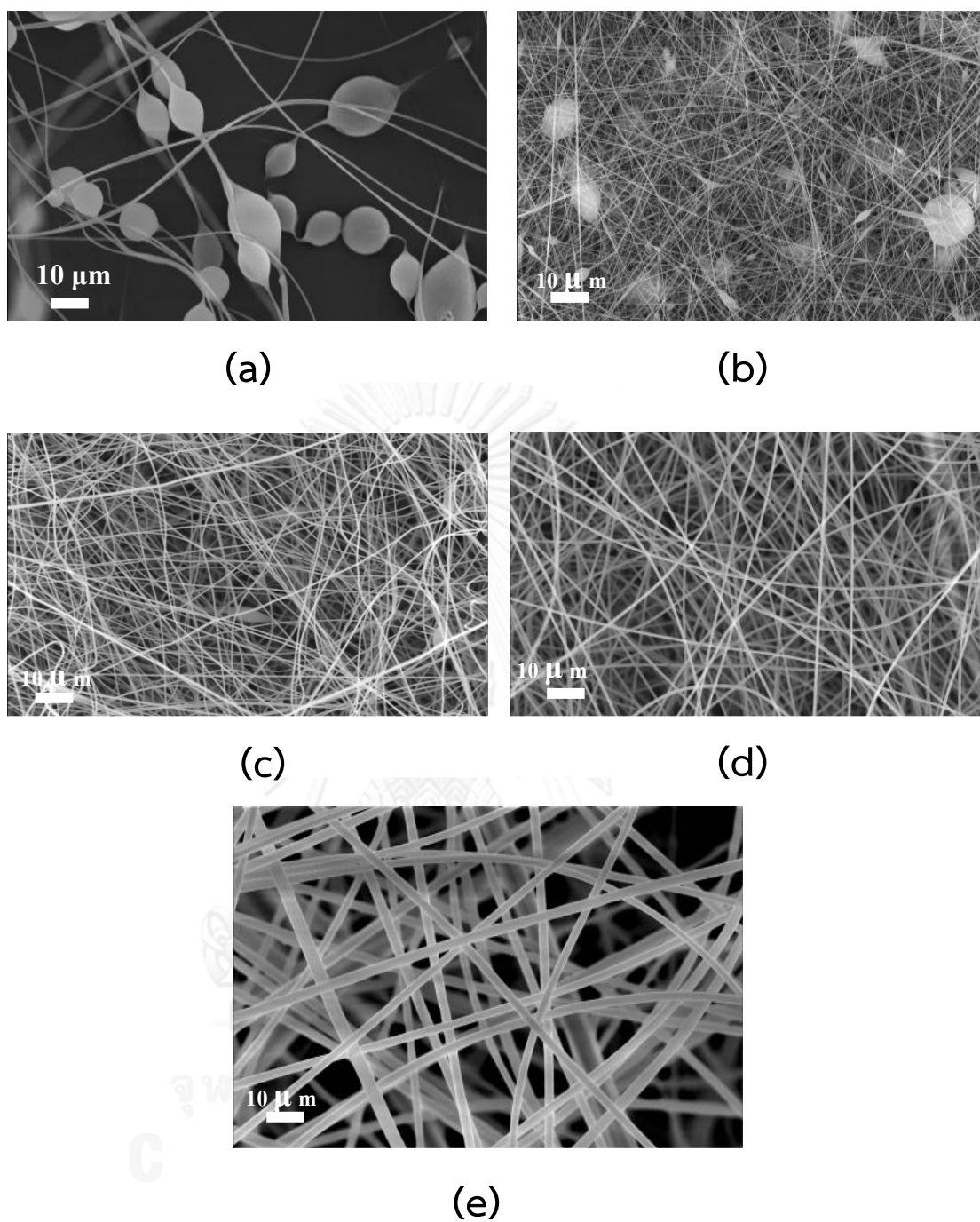
Figure 4-7. SEM images of ZnO/PAN co-axial nanofibers prepared by using PAN concentration of (a) 4%, (b) 6%, (c) 8%, (d) 10%, and (e) 12% by weight after calcination at 450°C. The concentration of PVP in the sheath solution was fixed at 12%.
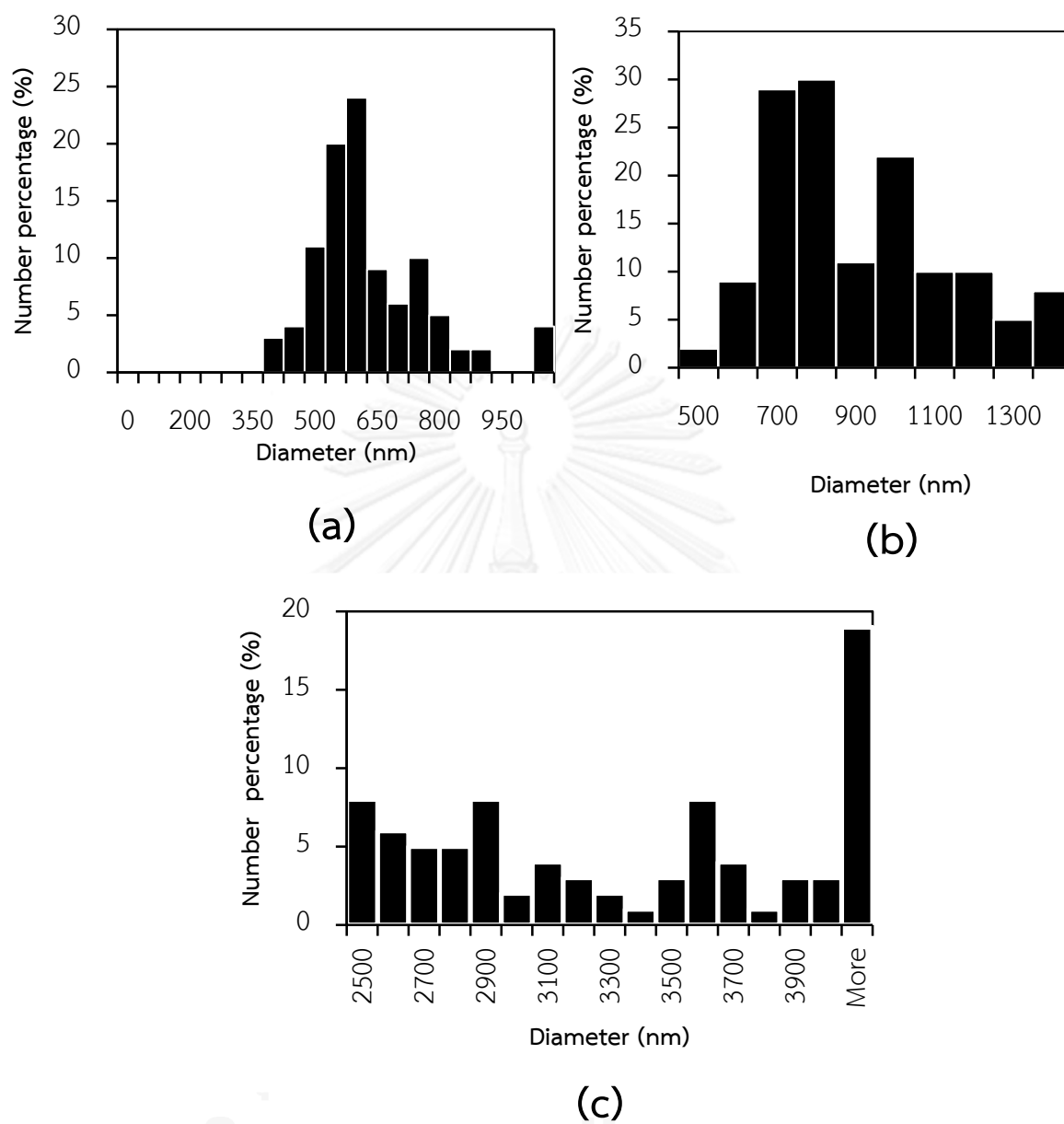
Figure 4-8. The size distributions of the nanofibers prepared by using PAN concentration of (a) 8%, (b) 10%, and (c) 12% by weight after calcination at 450⁰C. The concentration of PVP in the sheath solution was fixed at 12%.
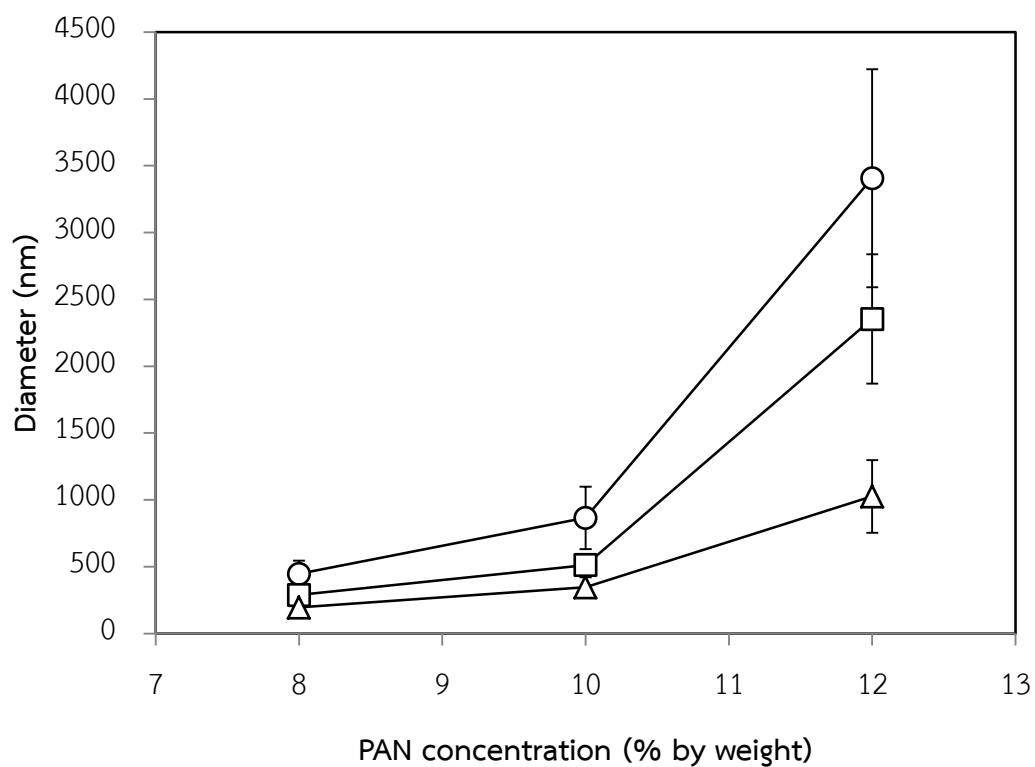
Figure 4-9. The diameters of co-axial nanofibers as the concentration of PAN in core solution is varied, while that of PVP in sheath solution is fixed at 12 wt%: (a) before being calcined, and after being calcined at (b) 450°C, and (c) 500°C.

Thereby, the increase in the core concentration increased both the core and overall fiber diameters as shown in schematic in Figure 4-10.

Figure 4-10. Schematic showing effect of core diameter on overall fiber diameter (a) smaller core diameter and larger sheath thickness, (b) larger core diameter and smaller sheath thickness [29].

The results from varying polymer concentration in both core and the sheath solutions indicate that the increase in the core concentration increases overall fiber diameters more significantly than the increase in the sheath concentration. So the PAN concentration is the significant factor to predict the diameter of co-axial fibers. The fixed analysis of variance (ANOVA) model for two-factor studies was used to determine the interaction between the effects of PAN concentration and PVP concentration on average diameter of the fibers. It concludes that interaction effects are present at 95% confidence levels. It also concludes that both of main effects are important (Appendix A).

4.1.4 Characteristic of core-sheath nanofibers

Thermal Gravimetric Analysis (TGA)
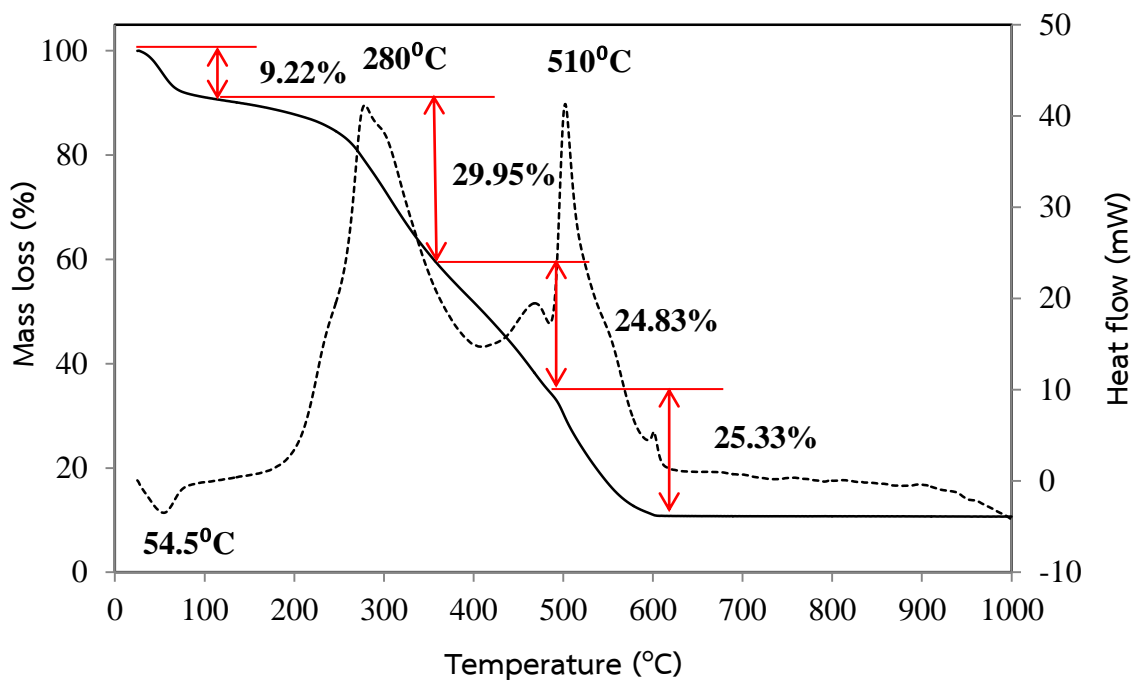
Figure 4-11. Thermal gravimetric analysis (TGA) and differential scanning calorimetry (DSC) of the as-spun ZnO/PAN co-axial fibers
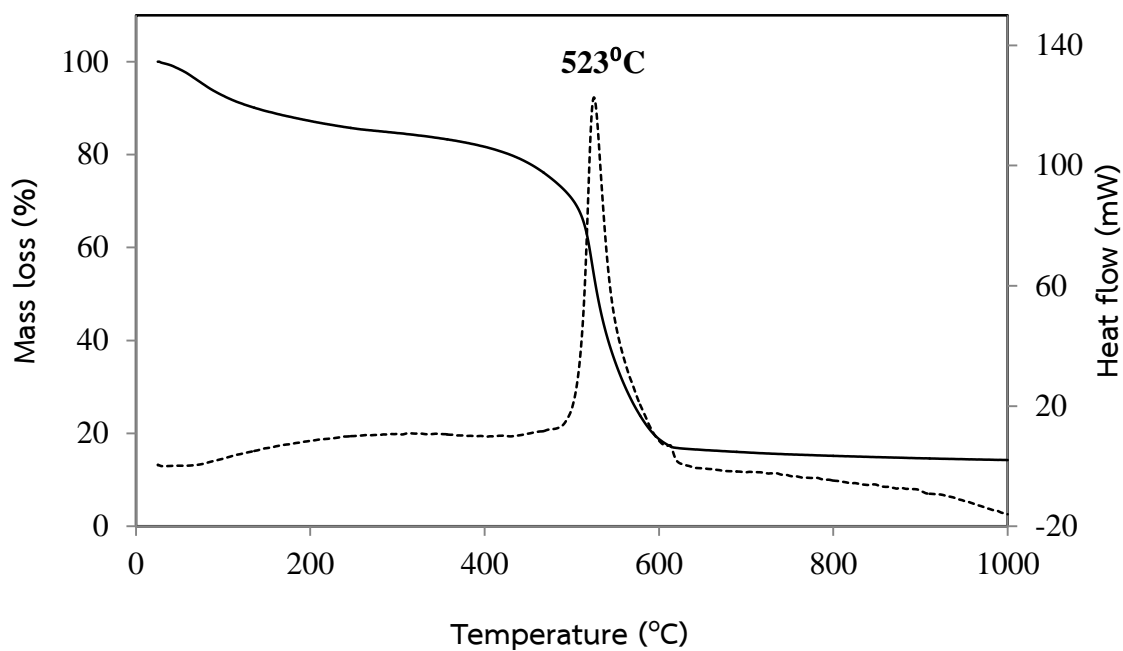
The thermal-gravimetric (TG) and differential scanning calorimetry (DSC) diagrams for as-spun co-axial nanofibers are shown in Figure 4-11. There are four-gravimetric steps. The first step is broad range between $54^\circ C$-$110^\circ C$, corresponding to about 9.22% weight loss, due to the volatilization of HCl and physio-sorbed water of which the boiling points are 57 and $100^\circ C$ respectively. The second step is between $110^\circ C$-$351^\circ C$, corresponding to about 29.95% weight loss, accompanied by a strong thermopositive peak ($280^\circ C$) in DSC curve. It is probably due to the decomposition of

PVP adhered to the ZnO nanoparticles surface, partial decomposition of PAN in the core structure, and removal of other organic matters such as DMF and diethanolamine, which has boiling point of 152-154, and 259°C respectively. The third step is accompanied by about 24.83% weight loss locating at around 351-477°C. This is due to the decomposition of polymer such as PVP and part of PAN according to reports by many researches about the decomposition temperature of PVP (Mw=1,300,000) and PAN (Mw=150,000) in the range of 250-420°C [11, 12] and 350-500°C [9] respectively. It should be noted that corresponding TG-DSC data of pristine PAN and PVP fibers are shown in Appendix B. The forth step is around 510°C, corresponding to about 25.33% weight loss, accompanied by a sharp thermopositive peak in the DSC curve. This step corresponds to the main decomposition of PAN core polymer.

According the TG-DSC diagram shown in Figure 4-12. for ZnO/PAN co-axial nanofibers after calcination at 450°C (for 2 hours in air), the TG graph shows a significant mass loss about 85%, accompanied by a strong thermopositive peak at 523°C which is due to the removal of residual PAN in the fibers.

From TG-DSC in Figure 4-11, and 4-12, it can be noted that, as the temperature is higher than 600°C, there is no significant weight loss, indicating the completion of ignition loss from the organic constituent and the remainder

corresponding to ZnO. The TG-DSC analysis shows the significant constraint of the calcination temperature to remove PVP in the sheath while keeping PAN in the core to sustain flexibility of final ZnO nanofibers. The proper calcination temperature is considered to be the range of 400°C-500°C.

Figure 4-12. Thermal gravimetric analysis (TGA) and differential scanning calorimetry (DSC) of ZnO/PAN co-axial nanofibers after calcination at 450°C for 2 h in air.
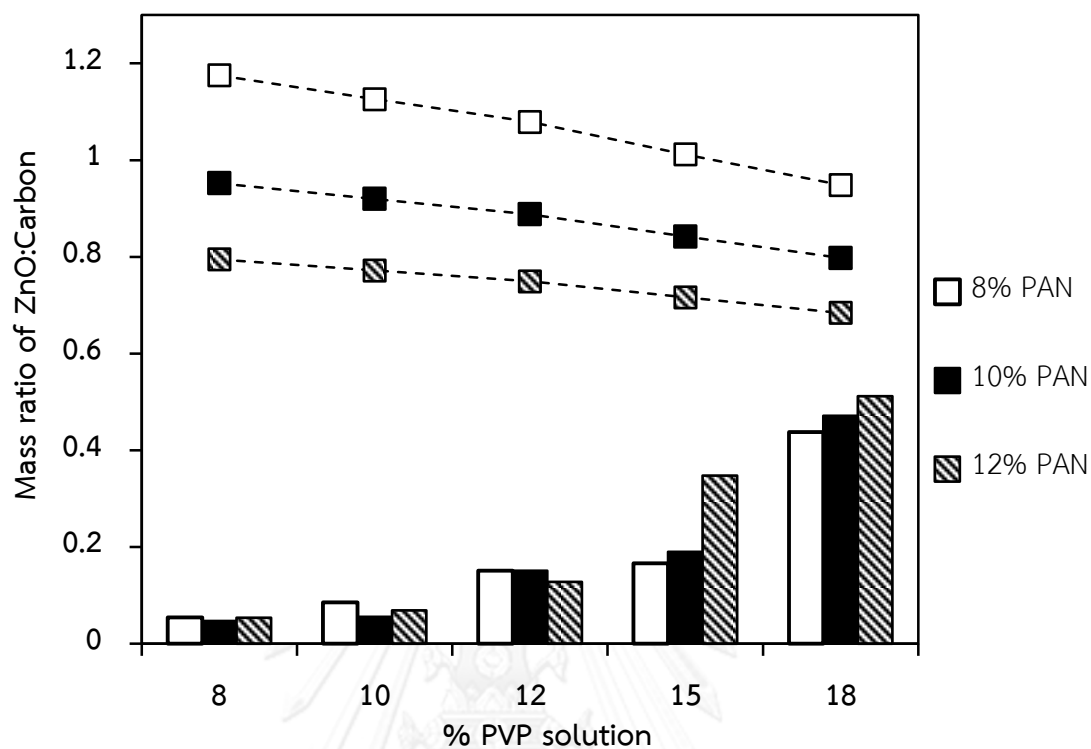
Figure 4-13. The comparison of the measured ZnO-to-carbon ratios in the fibers (bar graph) after calcination at 450⁰C to that of the predicted data (dash line).

The predicted ZnO-to-carbon ratio within the fibers was calculated from the basis of complete conversion of zinc acetate to zinc oxide. The residual mass of PVP and PAN after calcination at 450°C were gained from TGA data from pristine fiber of PVP and PAN. All prediction graphs (i.e., 8, 10, and 12% PAN concentration in core solution) decrease gradually when the concentration of PVP in the sheath solution is increased. Also the higher in the core concentration, the lower the ZnO content.

According to the bar graph expressing ZnO-to-Carbon from TGA data, shows that the higher in PVP concentration, the more ZnO content the fibers have. The

data cannot predict a relation between sheath concentration and core concentration in the range of 8-12% PAN in core solution. However, for 15 and 18% PVP in sheath solution, it can obviously see that high percentage of core yielding high content of ZnO.

From both of the comparison data, it is proposed that ZnO content does not directly related to polymers as predicted, but there is interaction between polymer concentrations and ZnO content. The concentration of sheath is the major factor affecting on ZnO content. Higher in sheath concentration carries more ZnO sol.

It can be explained that ZnO sol in PVP was not homogenously mixed with PAN in core, so the ZnO sol in PVP was not used up during the formation of stable Taylor cone. The important factors affecting the formation of Taylor cone are the viscosity and conductivity of both solutions. When the concentrations of solutions were varied that resulted in the different ratios of ZnO: PVP, it resulted in viscosity and conductivity of solutions. All reasons affected the Taylor cone structure and ZnO content eventually.

Characterization by electron microscopy

In this study, there were many constraints such as the calcination temperature should be high enough for removing PVP polymer from the sheath part of co-axial fibers and not too high to degrade most part of PAN core. Furthermore, the calcination temperature should be high enough to change the amorphous ZnO to crystalline ZnO. So, as a result from TGA, the calcination temperature was chosen to be 450°C for 2 hours, the after calcination products remain in fiber form and co-axial structure characterized from electron microscopy is shown in Figure 4-14 (b,d) respectively.
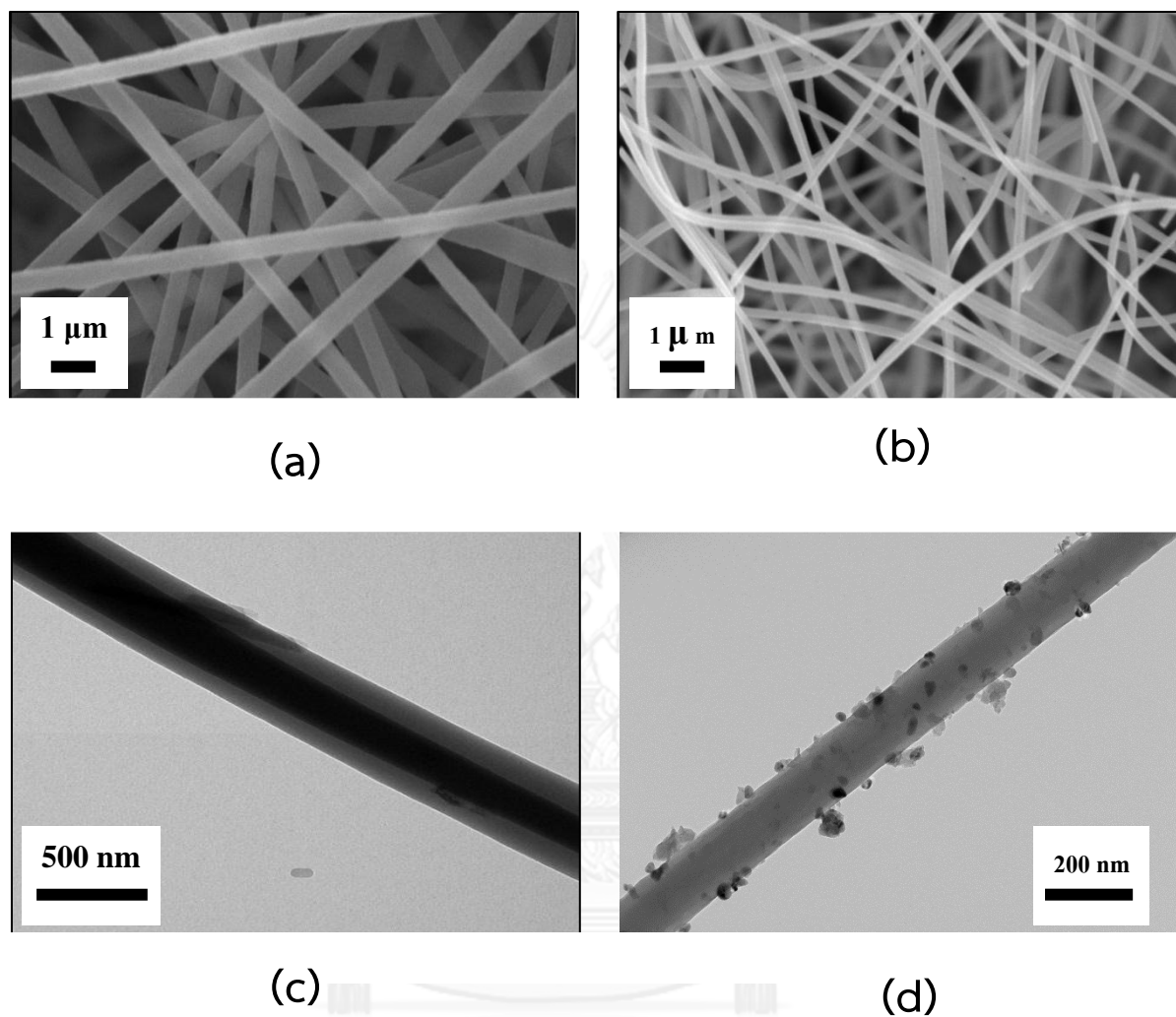
Figure 4-14. Electron microscropy images of co-axial nanofibers 15% PVP sheath and

8%PAN core; SEM images of (a) fibers before calcination, (b) fibers after it had been

calcined in air at 450⁰C and TEM images of; (c) fibers before calcination, (d) fibers

after it had been calcined in air at 450⁰C
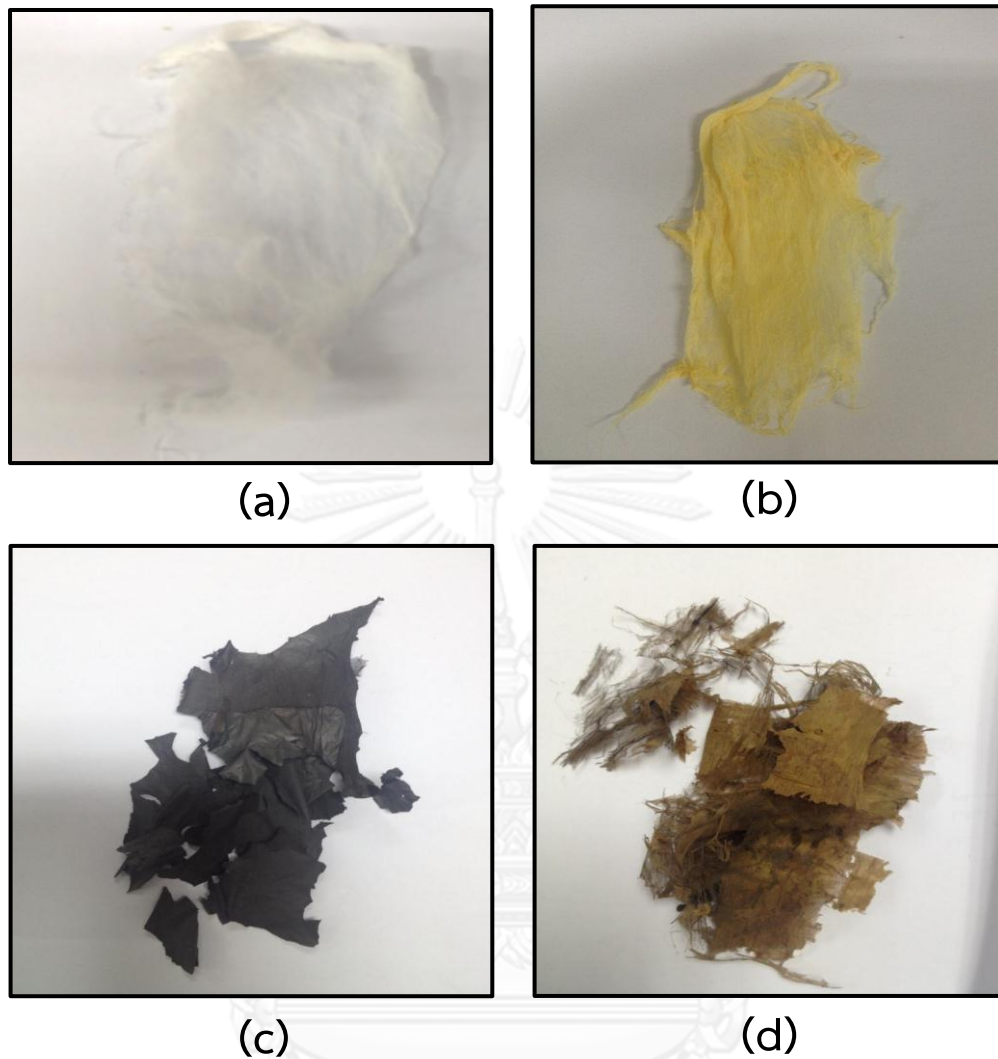
Figure 4-15. Photographs of nanofibers; (a) as-spun of co-axial ZnO/PAN, (b) co-axial

ZnO/PAN after heat treatment at 100^{0}C, (c) the after calcined co-axial fibers without

ZnO, and (d) ZnO/PAN co-axial fibers after calcination at 450^{0}C

From Figure 4-15d. the product after calcination are brown in colour that is

different from the after calcined co-axial fibers without ZnO, which were black colour

(figure 4-15c). The visible brown colour from the products may result from the

mixing effect of ZnO nanograins covering the polymer core due to the specific

physical property of ZnO called thermochromism [42, 43] and the visible core material.

Characterization by Brunauer-Emmett-Teller (BET)

Figure 4-16 and 4-17 presents the nitrogen adsorption-desorption isotherm of, ZnO/PAN co-axial fibers and PVP/PAN co-axial fibers, respectively. Both isotherms belonged to type III according to IUPAC classification, which is a typical characteristic adsorption-desorption isotherm of nonporous material.
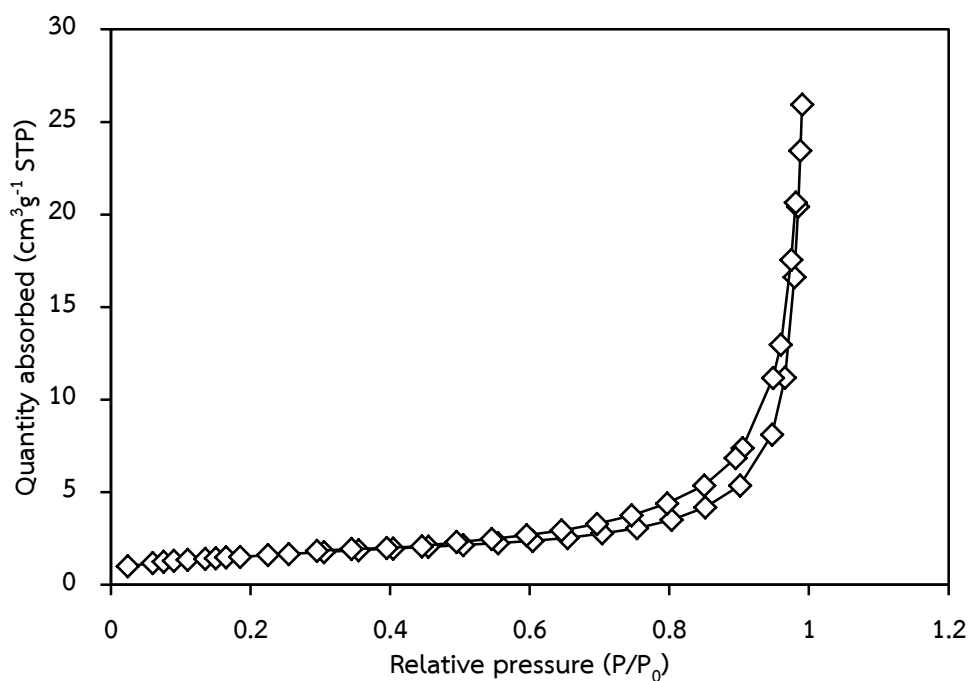
Figure 4-16. Nitrogen adsorption-desorption isotherm of the ZnO/PAN co-axial

nanofibers obtained at 450°C
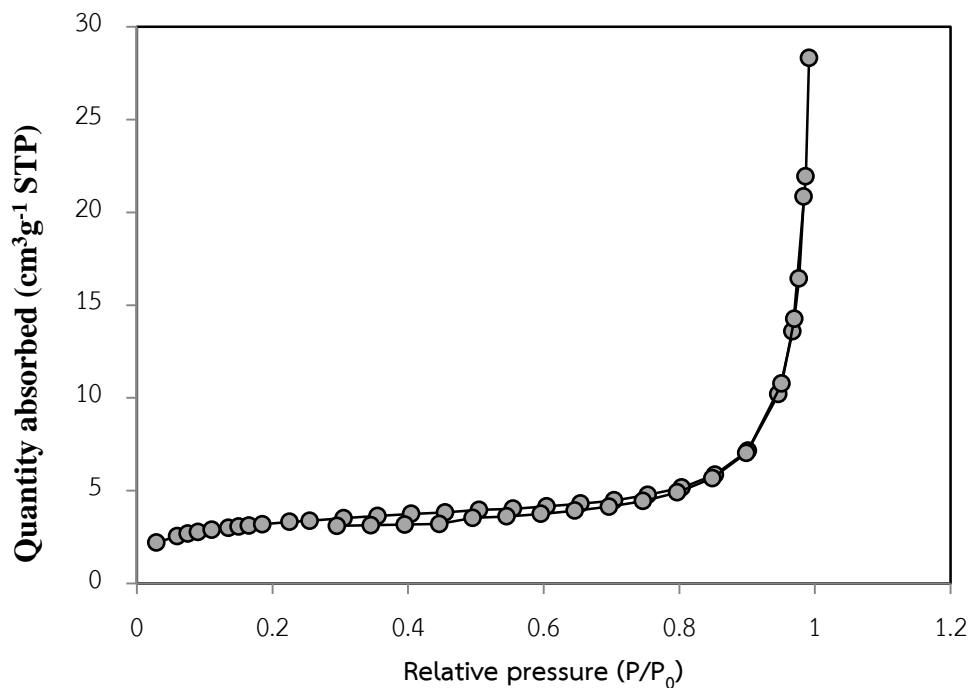
Figure 4-17. Nitrogen adsorption-desorption isotherm of the PVP/PAN co-axial

nanofibers obtained at 450°C

Table 4-1. Surface area of PVP/PAN co-axial fibers, ZnO/PAN co-axial fibers, ZnO

synthesis, ZnO commercial.

Product	Surface area ($m^2 g^{-1}$)
PVP/PAN co-axial fibers	5.2
ZnO/PAN co-axial fibers	4.8
ZnO synthesis	2.9
ZnO commercial	2.8

The difference between ZnO/PAN fibers and the synthesized ZnO powder is the specific surface area. As shown in Table 4-1, the specific area of ZnO/PAN fibers and the synthesized ZnO powder is 4.8 and 2.9 $m^2 g^{-1}$, respectively. The specific surface area of PVP/PAN co-axial fibers after calcination at 450°C is 5.2 $m^2 g^{-1}$ which is not different from the ZnO/PAN fibers. ZnO commercial and ZnO powder have the same specific surface area. Accordingly, the reason why the ZnO/PAN nanofibers have high surface area than ZnO powder may be the result from carbon fibers in polymer core.

4.1.5 Nanocrystalline ZnO in co-axial nanofibers

The morphology of ZnO nanocrystals and crystalline phase of ZnO are important factors influencing its photocatalytic activity. The corresponding XRD pattern shown in Figure 4-18. indicates that the ZnO nanocrystals have Wurtzite (hexagonal) phase. It may be noted that the (101) plane is a high density crystal plane (see the scheme of unit cell in Figure 4-21a) showing maximum diffraction intensity. The crystallite size of the ZnO phase calculated by the Debye-Scherrer was found to be 21 nm.
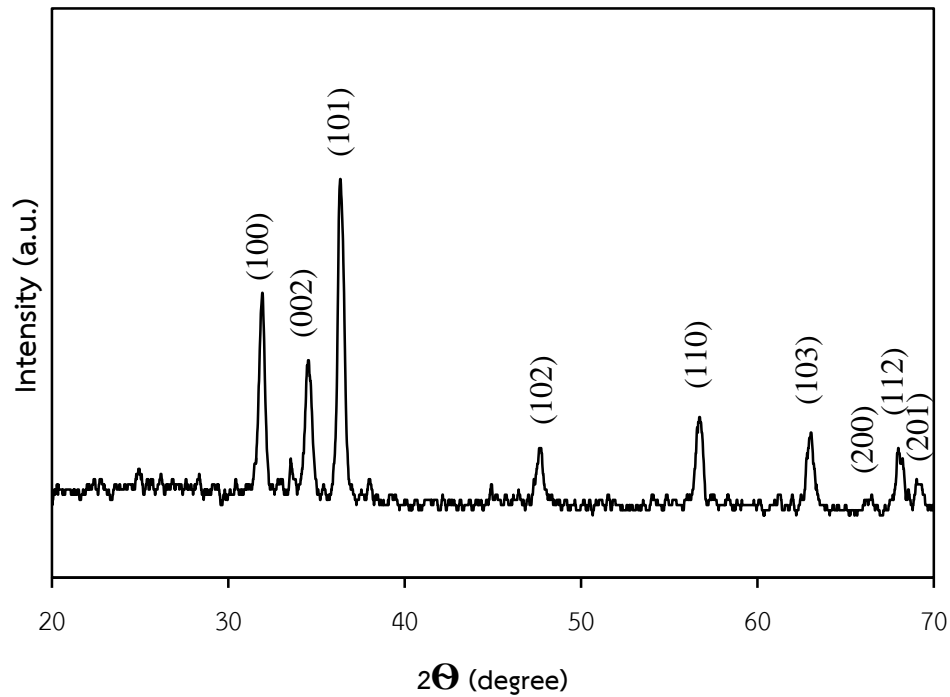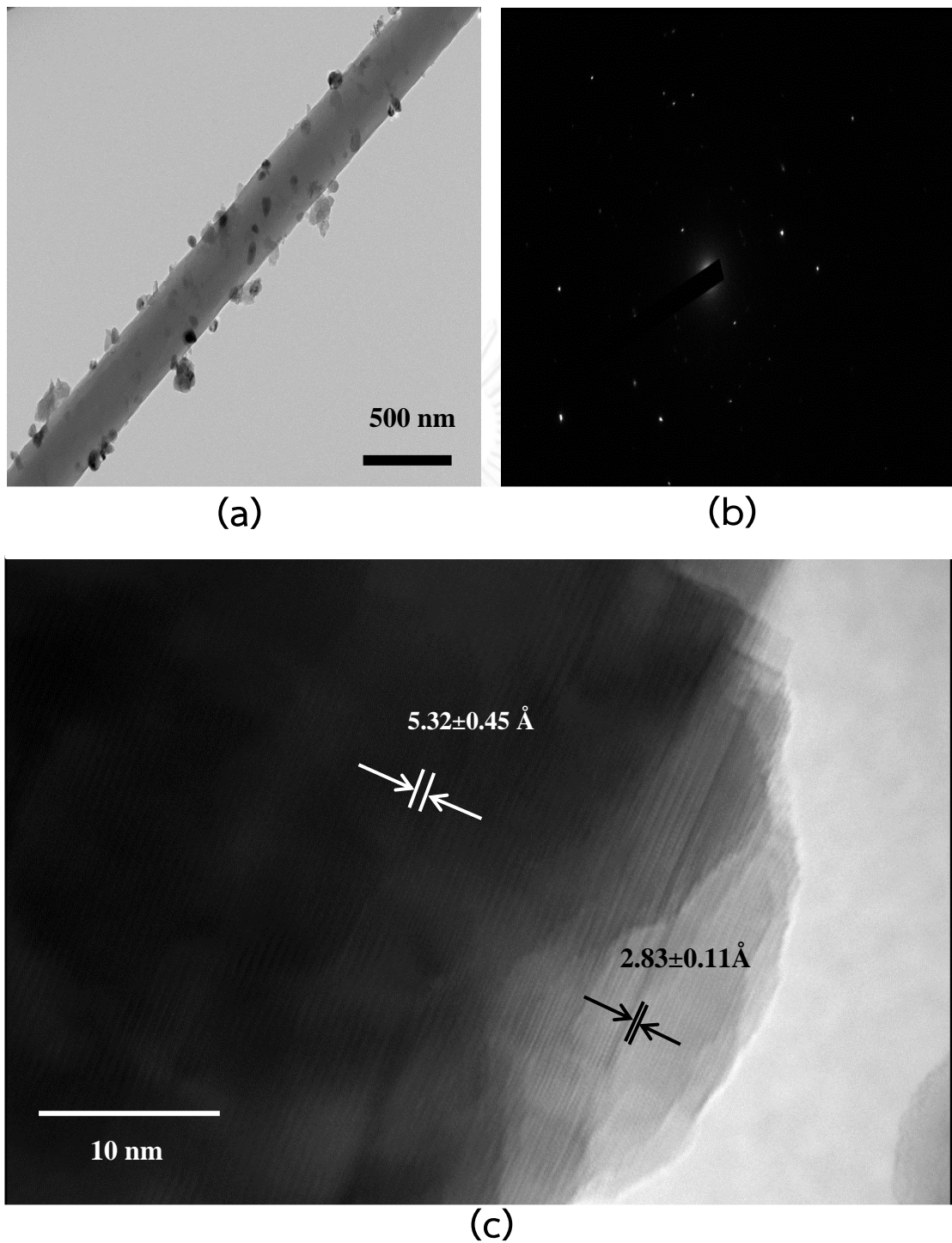
Figure 4-18. XRD pattern of ZnO/PAN nanofibers after calcination at 450°C for 2 hours in air

Figure 4-19 shows the TEM images of ZnO/PAN nanofibers after calcination at 450°C for 2 hours in air, in which the ZnO nanocrystals had an average grain size about 65±10 nm. From SAED pattern it suggests that single crystalline ZnO are distributing on the PAN core nanofibers. It can be confirmed by the SAED pattern in Figure 4-19(b)

(a)

(b)

(c)
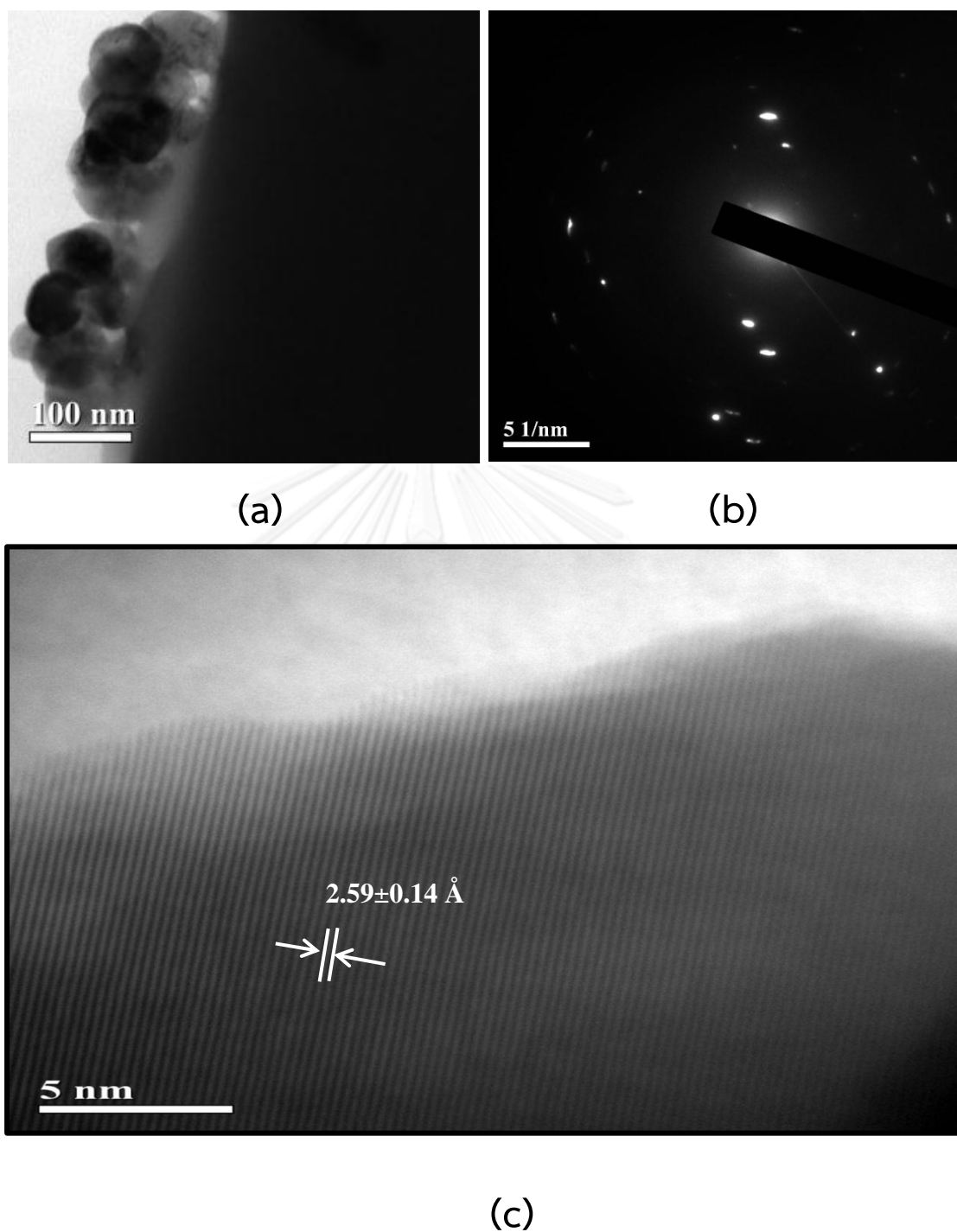
Figure 4-19. TEM image of (a) ZnO nanocrystals distributingon nanofibers after calcination at 450⁰C for 2 hours in air, (b) SAED pattern, and (c) HRTEM image showing lattice fringes of c-axis oriented ZnO.
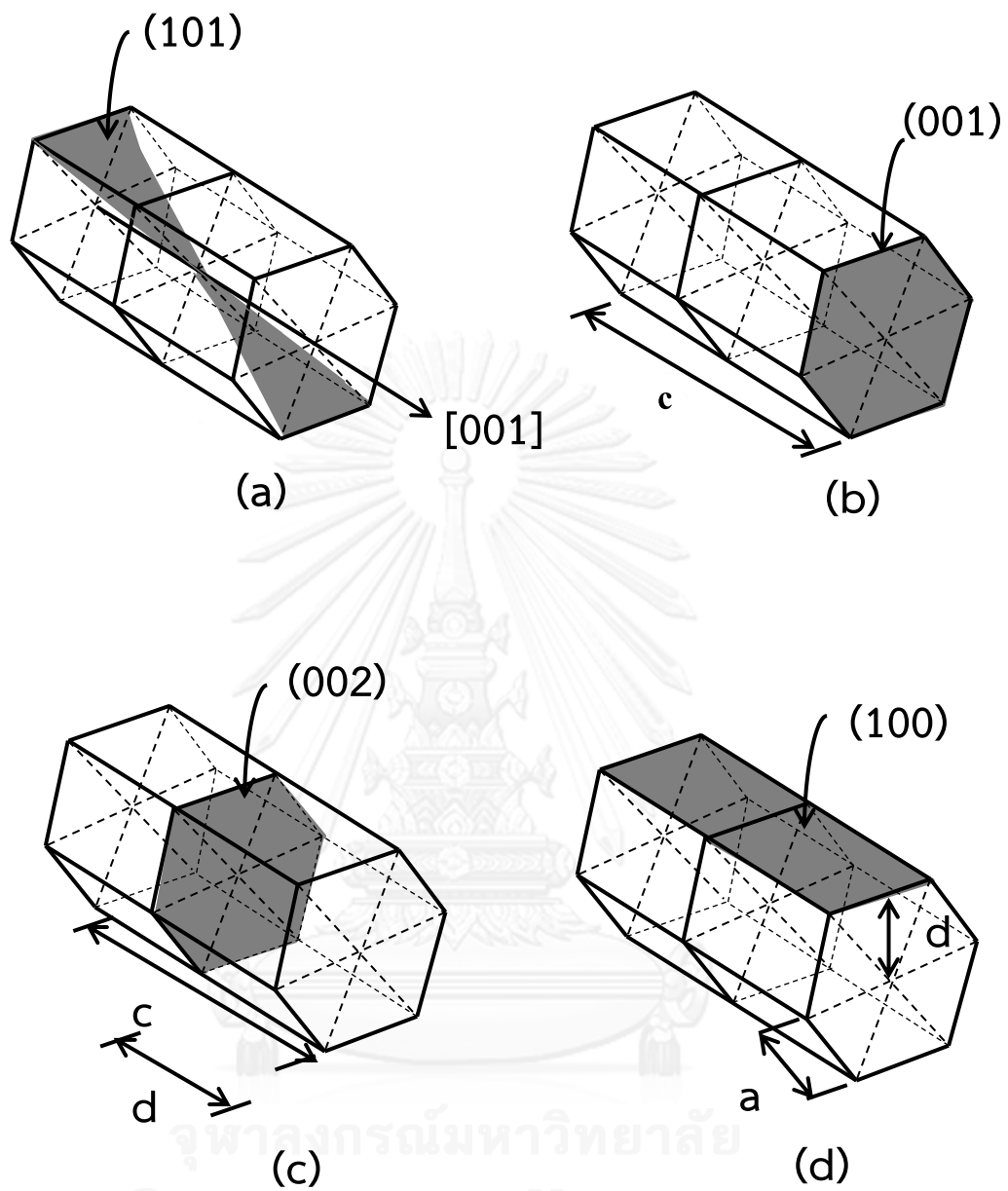
Figure 4-20. TEM image of (a) ZnO nanocrystals distributingon nanofibers after calcination at 450°C for 2 hours in air, (b) SAED pattern, and (c) HRTEM image showing lattice fringes of c-axis oriented ZnO

Figure 4-21. ZnO wurtzite (hexagonal) unit cell of (a) (101) plane, (b) (001) plane, (c) (002) plane, and (d) (100) plane

Figure 4-20 expresses the corresponding HRTEM image of the ZnO/PAN co-axial nanofibers, in which the measured interplanes spacing (d spacing) of 2.59, 2.82, and 5.32 Å match with the theory reported value of the (002), (100), and (001) plane in Wurtzite ZnO as reported in Table 4-2.

Table 4-2. Comparison between standard and measured spacing of lattice

(h k l)	Standard spacing of lattice (Å)	The measured spacing of lattice fringe (Å)	% of lattice error
(002)	2.6033	2.5861±0.1448	0.6616±0.0370
(100)	2.8146	2.8185±0.1047	0.1392±0.0051
(001)	5.2066	5.3247±0.4516	2.2684±0.1924

Table 4-3 summarizes the percent value of lattice error from the standard unit cell parameters. It is noted that the synthesized ZnO co-axial nanofibers have the same unit cell parameter value as the hexagonal ZnO wurtzite phase. The percent error of lattice in parameter a and c were due to the strain of crystal

Table 4-3. Comparison between standard lattice parameters and measured spacing

of lattice

Calculated from	unit cell parameters (Å)		% of lattice error
	a	c	
Standard spacing of lattice	3.2498	5.2066	
(002)		5.1722±0.2895	0.6618±0.0185
(100)	3.2545±0.0121		1.4639±0.0540
(001)		5.3247±0.4516	2.2684±0.1924
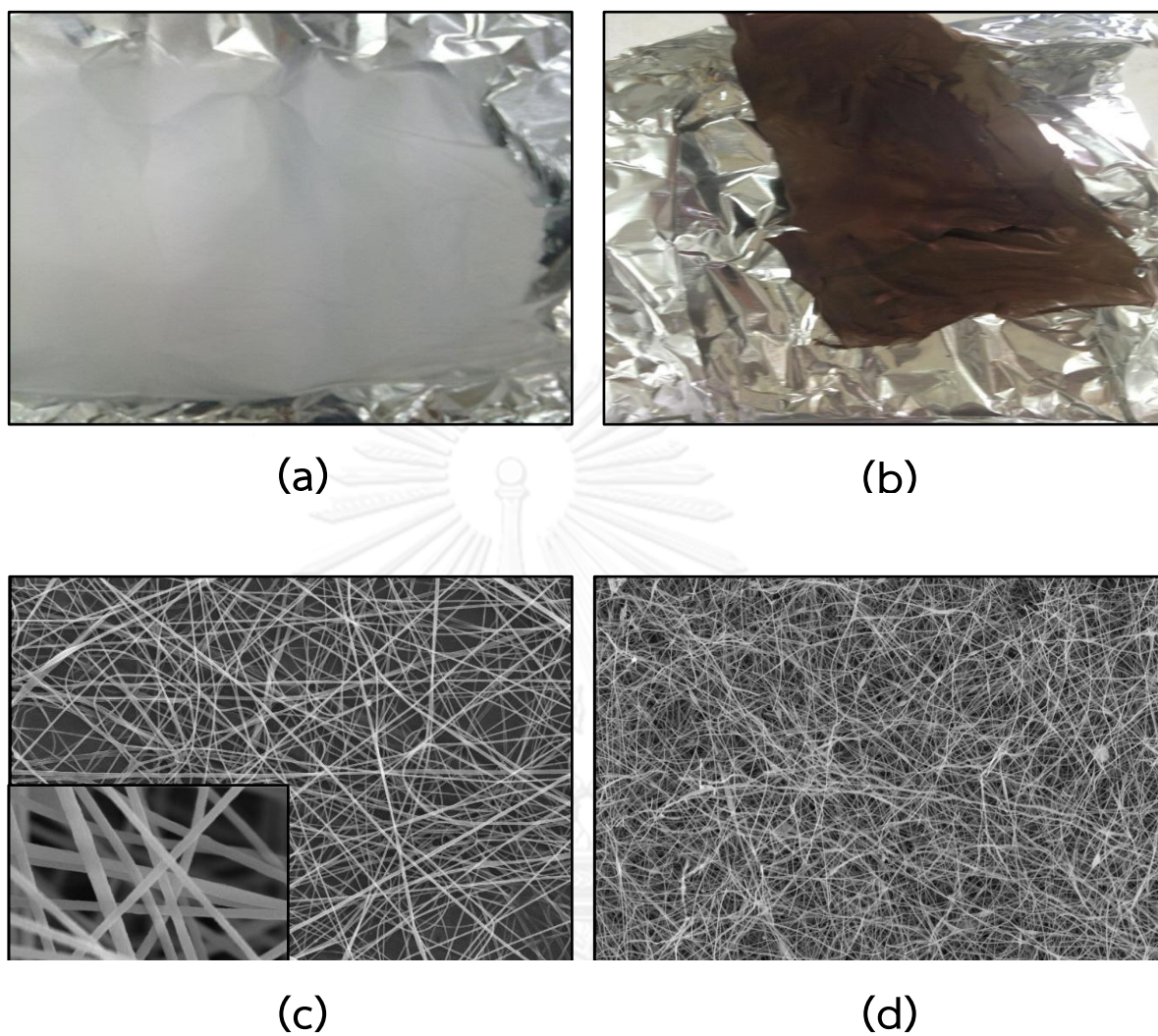
Figure 4-22. Photograph of PAN nanofibers (a) as-spun PAN fibers web (white), (b) after calcination at 450⁰C (dark brown) (2 hours in air), and scanning electron microscopy images (c) as-spun PAN fibers, (d) after calcination at 450⁰C (2 hours in air)

According to the Figure 4-22, the sheet of fibers still can be obtained after calcination due to the remaining of residual carbon from PAN polymer in ladder structure. As shown in Figure 4-22a. fibers were carbonized at elevated temperature, up to 450 ℃ in air, a dark brown nanofibers web was obtained. These molecular structure changes in the nanofibers can be further confirmed by the following FT-IR

4.1.7 Fourier transform infrared spectrpscopy (FT-IR) analysis
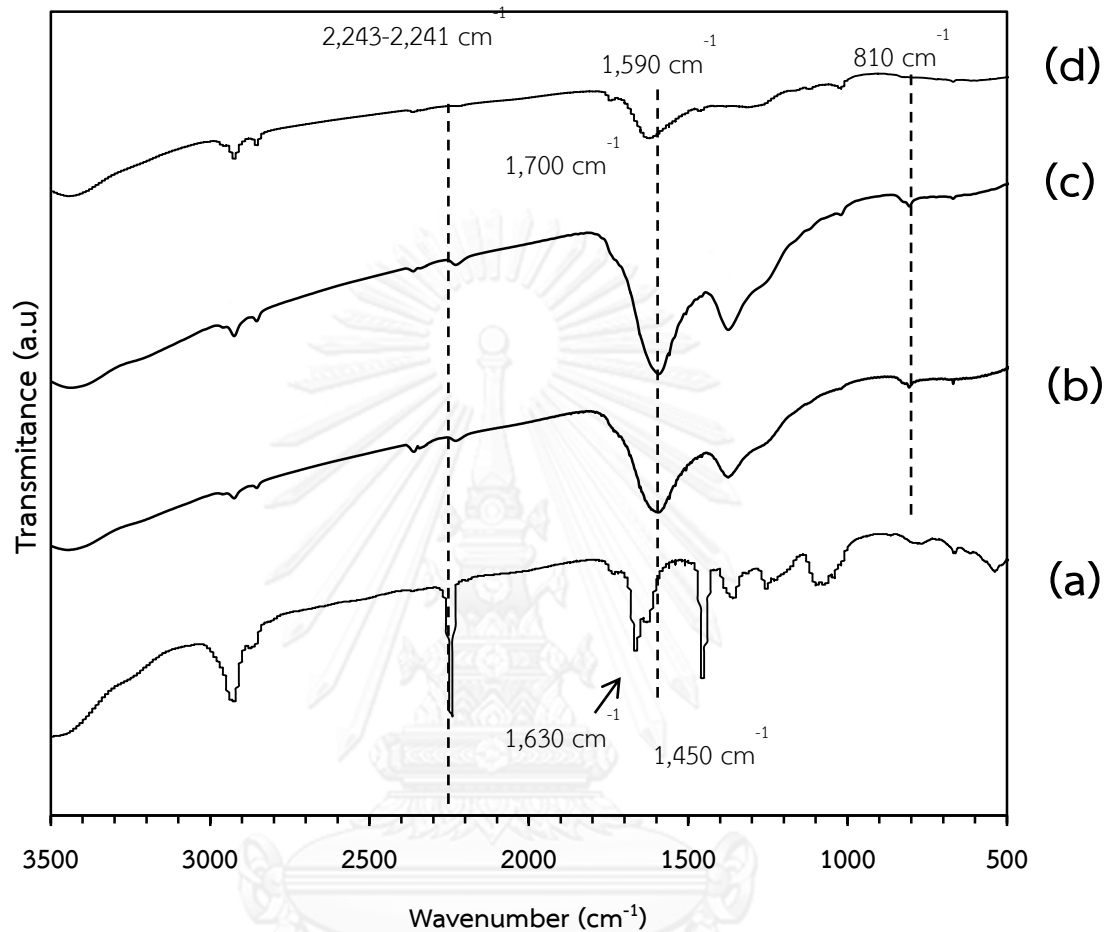
Figure 4-23. FT-IR spectra of PAN pristine fibers (a) as-spun fibers and after

calcination (b) at 400⁰C, (c) 450⁰C and, (d) 500⁰C respectively

Figure 4-23 shows the FT-IR spectra of PAN nanofibers calcination at different temperatures. The vibration characteristic of PAN pristine fibers are those of C≡N nitrile group at about 2,243-2,241 cm^{-1}, and the bands in regions 2,925 cm^{-1}, 1,450 cm^{-1}, 1,361 cm^{-1} and 1,254 cm^{-1} , which are assigned to the aliphatic CH group vibrations of different modes in CH, CH$_2$, and CH$_3$, respectively [44, 45]. As the calcination temperature is increased, the most prominent structural changes were the decrease in the intensities of the 2,243-2,241 cm^{-1}, attributed to C≡N band, and also the decrease of those for aliphatic C-H ones, concomitant with the advent and increase of a shoulder-like peak around 1,700 cm^{-1} due to cyclic C=O; Shimada and Takahagi reported that these shoulders are assigned to the free ketones in hydronaphthyridine rings and the conjugated ketones in acridone rings, resulting from the oxygen uptake reaction [46]; Peaks around 1,590 and 1,620 cm^{-1} corresponds to C=N, C=C, N=H mixed in-plane bending of the ladder frame, and the band at 810 cm^{-1} due to C=C-H (aromatic ring) [47]. The ladder may correspond to a side reaction taking place in the process. With the progression of the stabilization, the magnitudes of the band at 810 cm^{-1} from (=C—H) is increased, while that of signal for methylene (CH$_2$) at 1,450 cm^{-1} is decreased [48]. The conjugate structure concerning 1,580, 1,600, and 1,620 cm^{-1} are illustrated as seen in Figure 4-24.
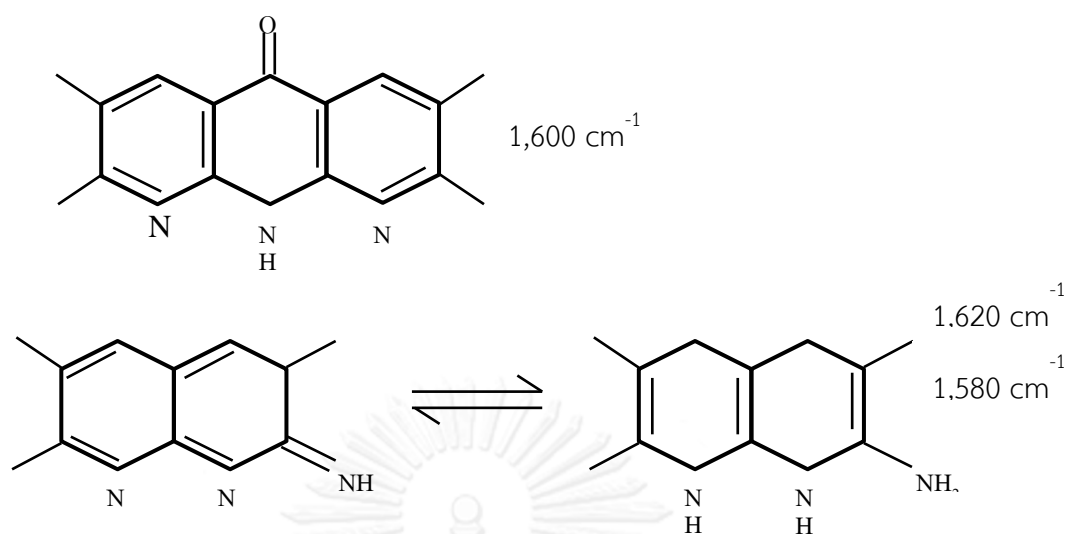
Figure 4-24. The conjugate structure concerning 1,580, 1,600, and 1,620 cm^{-1}

The band at 1630 cm^{-1} appearing only in spectrum of as-spun fibers is assigned to be the stretching of C=O bond from the DMF solvent remaining in fibers.

These spectroscopic results express that some chemical processes occurred during the oxidative stabilization. Firstly, reaction of nitriles results in conjugated C=N containing structures which results from intramolecular cyclization or intermolecular crosslinking. Secondly, the generation of conjugated C=C structures results from dehydrogenation or from imine-enamine tautomerization and subsequent isomerization [49]. Thirdly, the oxidation gives rise to carbonyl group.
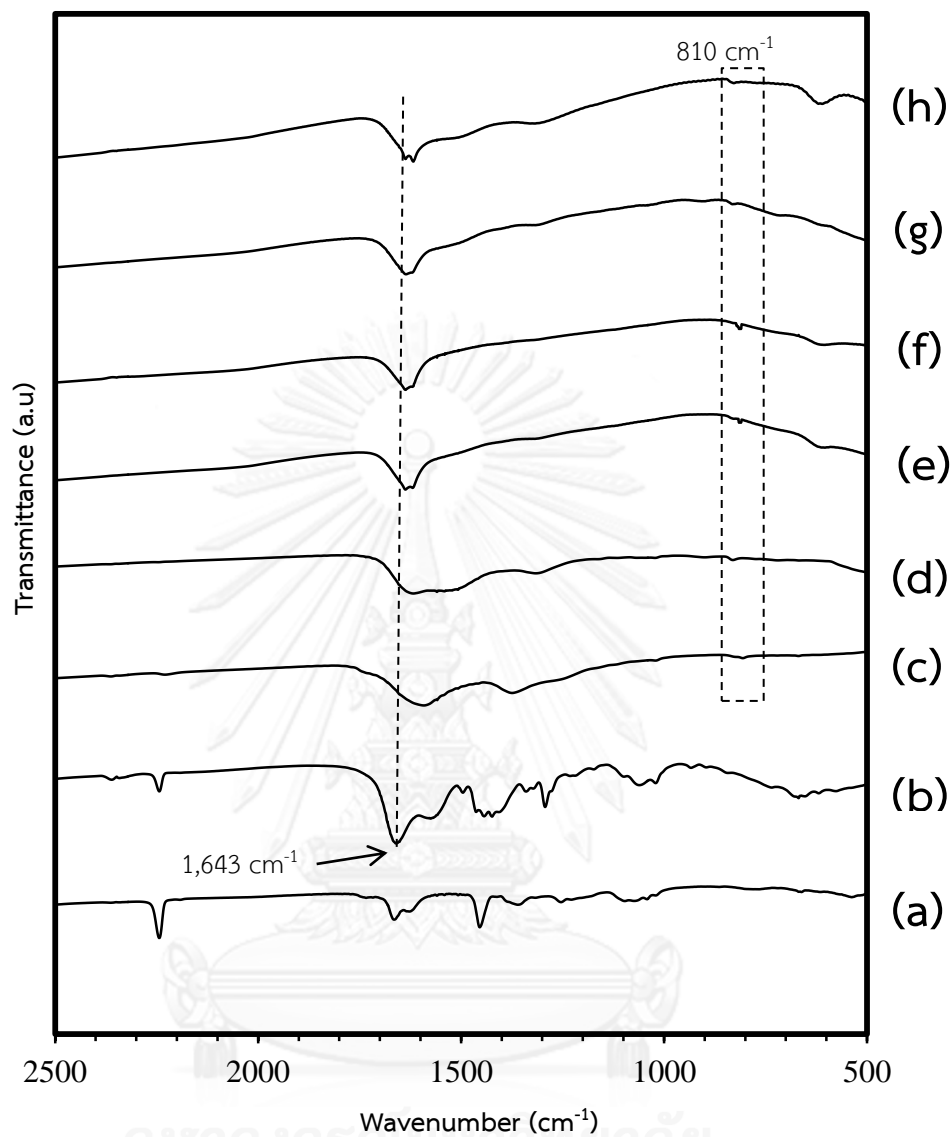
Figure 4-25. FT-IR spectrums of (a) as-spun PAN pristine fibers, (b) as-spun co-axial fibers, (c) PAN pristine fibers after calcination at 450°C, co-axial fibers after calcination at 450°C for (d) 2 hours, (e) 3 hours, (f) 4 hours, (g) 5 hours, and (h) 6 hours.

Figure 4-25 (a,c) shows that heating up PAN fibers for longer period of time results in the conjugation in cyclic structure of PAN forming aromatic ring as

confirmed by the band of aromatic C=C at wavenumber of 810 cm^{-1}. FT-IR spectra of PAN/ZnO co-axial fibers is almost the same as the spectra of pristine PAN fibers after being calcined at 450$^{\mathbf{o}}$C. It can be learned from this result that PAN in the core fibers remains in the stable ladder polymer after calcination [50]. However, the change of PAN does not affect the flexibility significantly, since the modified PAN is still a polymer. The wavenumber below 600 cm^{-1} is the spectra of ZnO in the fibers. On the other hand, PVP in the sheath is removed after calcination as noticed in the C=O bond at wavenumber of 1643 cm^{-1} of Figure 4-25b.

4.2 Flexibility of PAN/ZnO Co-axial Nanofibers

The fibers flexibility is recognized as one of the most important feature in this work. The carbon core from PAN sustained the flexibility of co-axial fibers after calcination at relatively high temperature in order to eliminate PVP and form the ZnO crystalline. The expectation of the final PAN/ZnO co-axial nanofibers should have the flexibility implied by the appearance of plastic region in stress-strain curve.

The flexibility of PAN/ZnO fibers cannot be measured by bending test directly due to the limitation of the characterization. So the plastic region appearing in stress-strain curve implies the flexibility of product.

4.2.1 Effect of calcination temperature on flexibility of fibers

The flexibility of the PAN/ZnO core/sheath nanofibers was investigated by universal testing machine. It can be seen from Figure 4-26 that mechanical behavior of the products after calcination at 450°C is somewhat similar to that of the as-spun fibers, i.e., consisting of two regions starting from linear elastic region and subsequent plastic region. The ductile behavior shown by the plastic region is the significant indicator for the flexibility of the fibers (also shown in Figure 4-27). Nevertheless, it should be noted that the yield strength of the calcined fibers is about 18% lower than that of the as-spun fibers due to the deterioration of PAN by heat. When the calcination temperature was raised to 500°C, however, the obtained fibers reveal the

lack of the plastic region representing brittle behavior. The mechanical performances

of the products are summarized in Table 4-4. So the suitable calcination temperature

was below 500°C to keep the residual PAN carbon in the flexible form such as ladder

structure.

Table 4-4. Mechanical Properties of co-axial nanofibers

Co-axial fibers	Stress (MPa)	Strain (%)	Fracture point (%)
As-spun	10.33	8.85	10.13
After calcination at 450°C	8.5	5.74	6.53
After calcination at 500°C	6.87	2.89	2.89
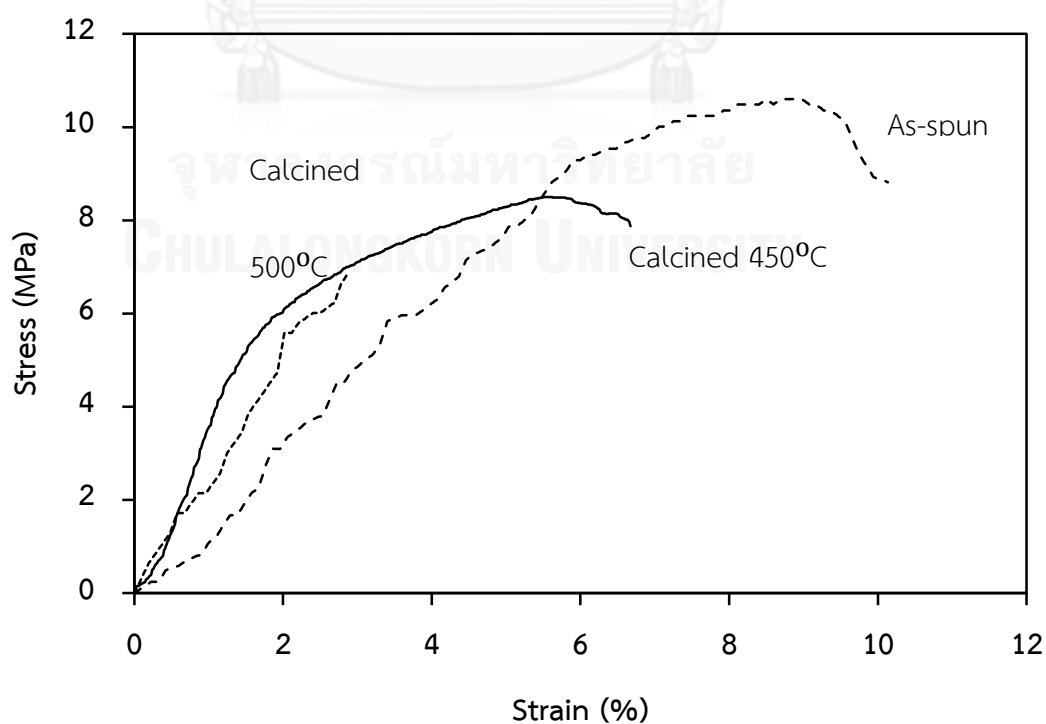
Figure 4-26. Stress-strain curves of co-axial fibers before calcination and after it had been calcined at 450⁰C and at 500⁰C.
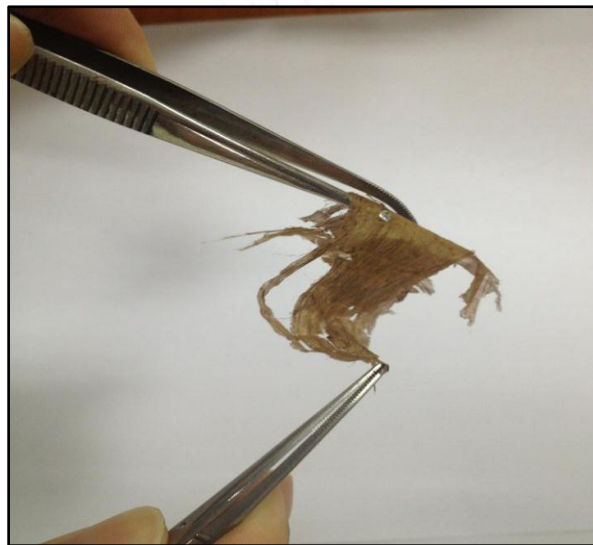
Figure 4-27. PAN/ZnO co-axial fibers after calcination at 450⁰C

4.2.2 Effect of polymer concentration on flexibility of fibers

In this work, the polymer concentrations, both PVP in sheath and PAN in core, were varied in order to achieve the co-axial structure and flexibility of the fibers. The PVP sheath concentration was varied five values i.e., 8, 10, 12, 15 and 18 % by weight. PAN core concentration was varied three values i.e., 8, 10, and 12 % by weight. After being calcination at 450°C, either residual PAN in the core or ZnO crystals including remainder PVP in the sheath, depending on the varied PVP sheath

concentration, affects the flexibility of products. Figure 4-28 shows the stress-strain curves of the products. Mechanical behavior of the products after calcination at 450°C can be seen in Fig.4-28. The dash line shows the behavior of pristine PAN at 8, 10, and 12%. From the stress-strain curves, it can obviously divide into two groups; one is below the stress of 10 MPa, the other is above this value. The conditions that stress higher than 10 MPa were 8%PVP-8%PAN, 8%PVP-10%PAN, 8%PVP-12%PAN, 10%PVP-8%PAN, and 10%PVP-12%PAN. It may be the effect between the viscosity of core and sheath. At relatively low viscosity of sheath i.e., 8% and 10%, the effect of core was stronger than sheath. So the performance of curves was near the behavior of the pristine PAN. Most of the co-axial fibers abide by the former group, which the stress is lower than 10 MPa (not shown in Figure) Appendix C. The behavior of stress-strain deviated from pristine PAN significantly.
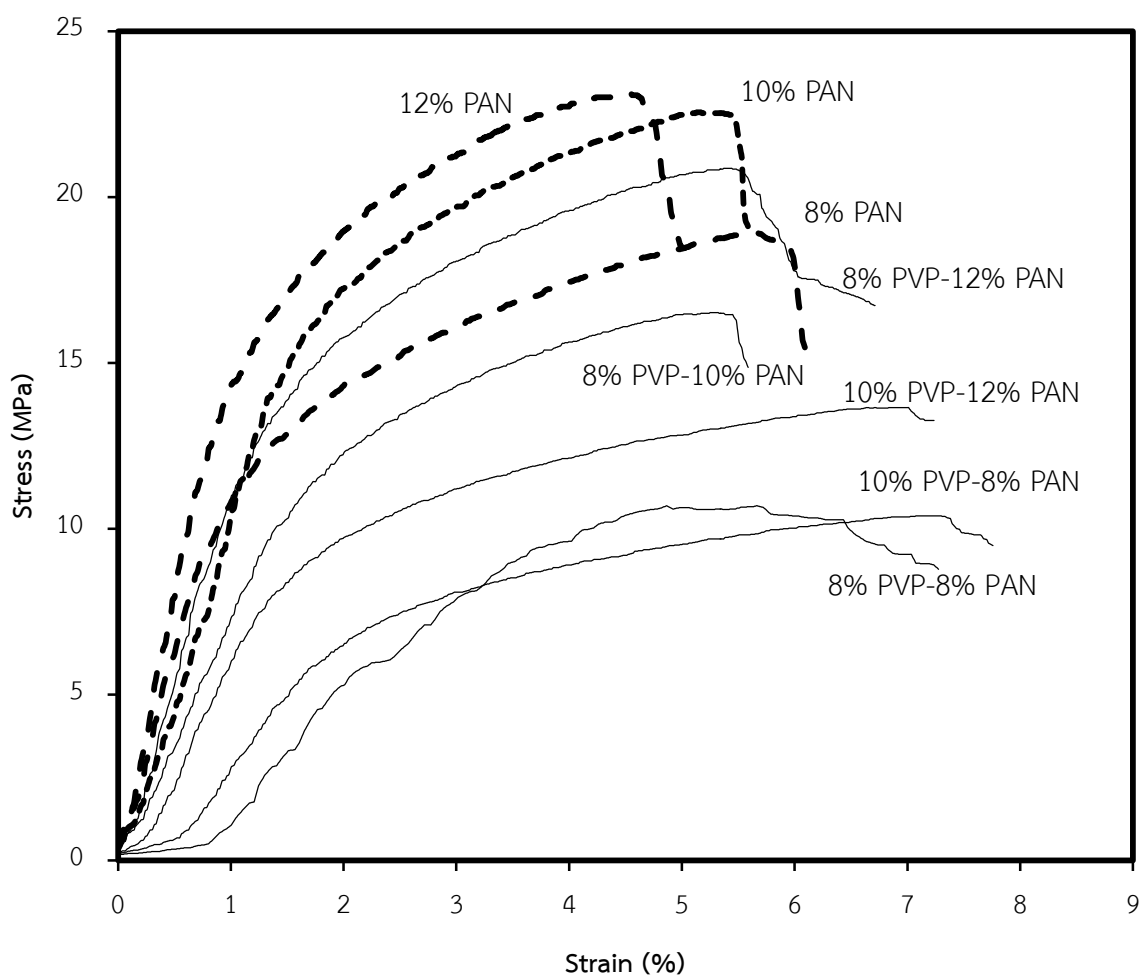
Figure 4-28. Stress-strain curves of co-axial fibers after it had been calcined at 450⁰C

(selected data above the stress of 10 MPa)

4.2.3 Strain of ZnO/PAN co-axial nanofibers

As seen in Figure 4-28, the conventional stress-strain curve can identify different ways in which the fibers behaved; starting at elastic behavior. A slight increase in stress above the elastic limit will result in a breakdown of the fibers and cause them to deform permanently. This behavior is called yielding. Once the yield point is reach, the fibers will continue to elongate (strain) without any increase in load. When the material is in this state, it is referred to being "plastic behavior". The objective of this work is the use of co-axial fiber for photocatalytic applications in form of membrane catalyst. The flexibility is the most important characteristic one value that can represent the flexibility is the strain at yield point. Table 4-5 shows the strain at ultimate point of fibers.

**Table 4-5.** The ultimate strain of fibers (%)

Factor A	Factor B				
	(display PVP sheath concentration)				
(display PAN-core concentration)	B1 (8%)	B2 (10%)	B3 (12%)	B4 (15%)	B5 (18%)
A1 (8%)	4.84	7.04	5.47	4	4.94
	4.68	6.59	5.7	3.95	5.14
Average	4.76	6.82	5.59	3.97	5.04
A2 (10%)	5.22	6.83	6.8	6.97	4.70
	4.272	7	6.85	6.75	3.96
Average	4.75	6.92	6.83	6.86	4.33
A3 (12%)	5.34	6.6	9.84	6.99	6.4
	6.74	7.96	9.95	8.16	6.23
Average	6.04	7.28	9.90	7.58	6.32

The number of cases for each of 15 treatments is 2.

Figure 4-29 contains two plots of the estimated treatment means. In Figure 4-29a, the five curves represent the different percentage of PVP sheath, and in figure 4-29b, the three curves represent the different percentage of PAN core. Multiple group comparisons were used one way ANOVA by Bonferroni test confidence coefficient of

95%. It can be noted that 12% sheath-12% core yield the best value of strain. It should be noted that the statistically significant difference between two points are marked with the asterisk (*).
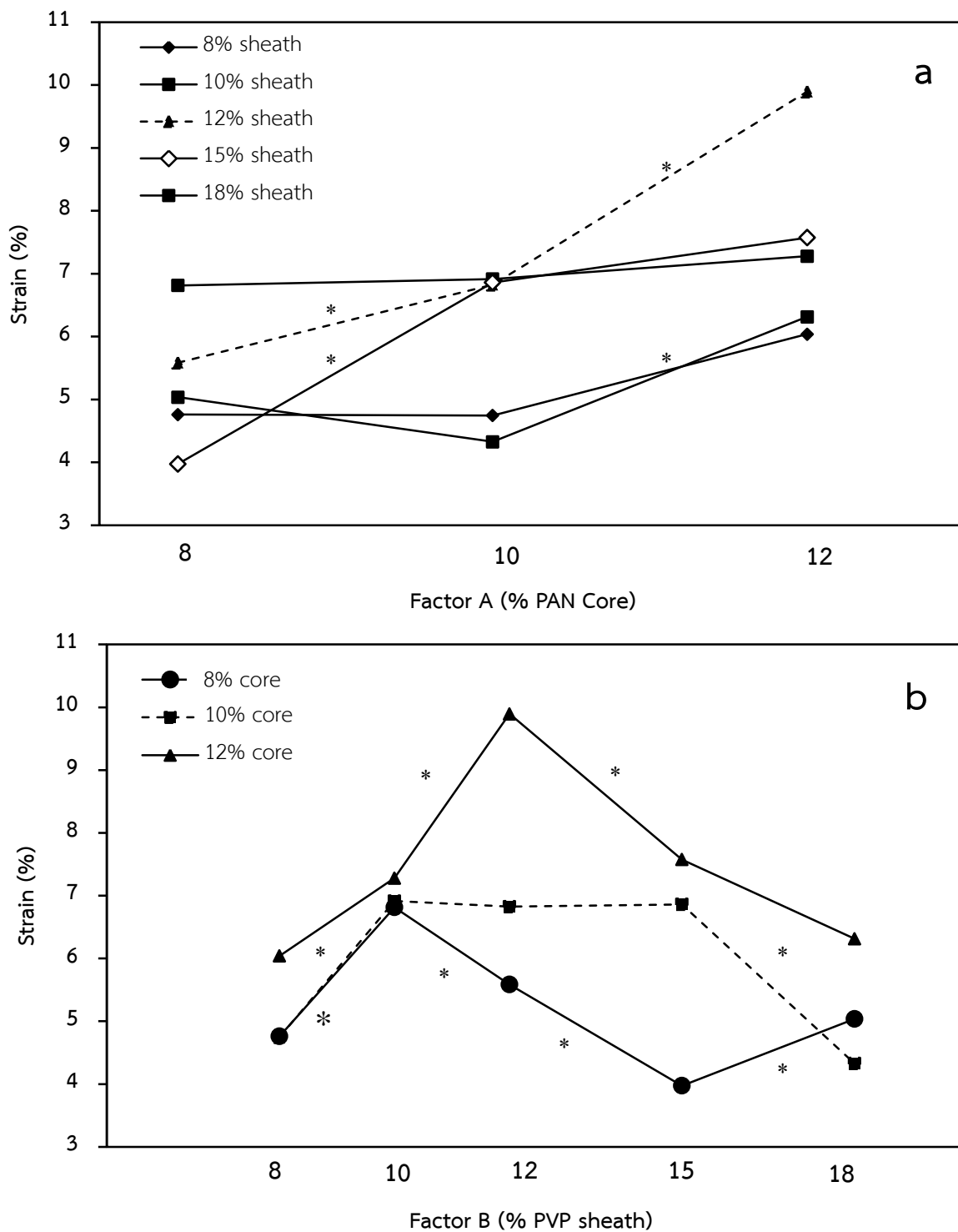
Figure 4-29. Plots of the estimated treatment means, (a) percentage of PVP sheath curves, and (b) percentage of PAN core curves. (Multiple groups comparisons were used one way ANOVA by Bonferroni test *P<0.05)

4.2.4 Stress of ZnO/PAN co-axial nanofibers

Stress value represents the internal force acing normal to the area of fibers.

On the other hand, it shows how strong the fibers are. Table 4-6

Table 4-6. The ultimate stress of fibers (MPa)

Factor A	Factor B				
	(display PVP sheath concentration)				
(display PAN-core concentration)	B1 (8%)	B2 (10%)	B3 (12%)	B4 (15%)	B5 (18%)
A1 (8%)	10.69	10.39	8.50	6.96	7.42
	10.91	11.15	8.73	6.75	7.30
Average	10.8	10.77	8.62	6.86	7.36
A2 (10%)	16.51	6.63	7.47	8.57	8.95
	18.83	6.86	9.16	8.57	5.70
Average	17.67	6.75	8.31	8.57	7.33
A3 (12%)	20.86	13.63	6.13	10.06	8.91
	18.10	11.17	6.15	8.23	9.35
Average	19.48	12.40	6.14	9.14	9.13

Figure 4-30 and 4-31 show plots of the estimated treatment means. In Figure 4-30, the five curves represent the different percentage of PVP sheath, and in figure 4-31, the three curves represent the different percentage of PAN core. It should be noted that the statistically significant difference between two points are marked with the asterisk (*).

Figure 4-30 and 4-31 also suggest that the average ultimate stress of the fibers tends to be higher when the core concentration is increased. It can be marked that the low percentage in sheath gave the high of stress value. The reason is the domination of PAN core, as shown in Figure 4-31 for 8 and 10% sheath.
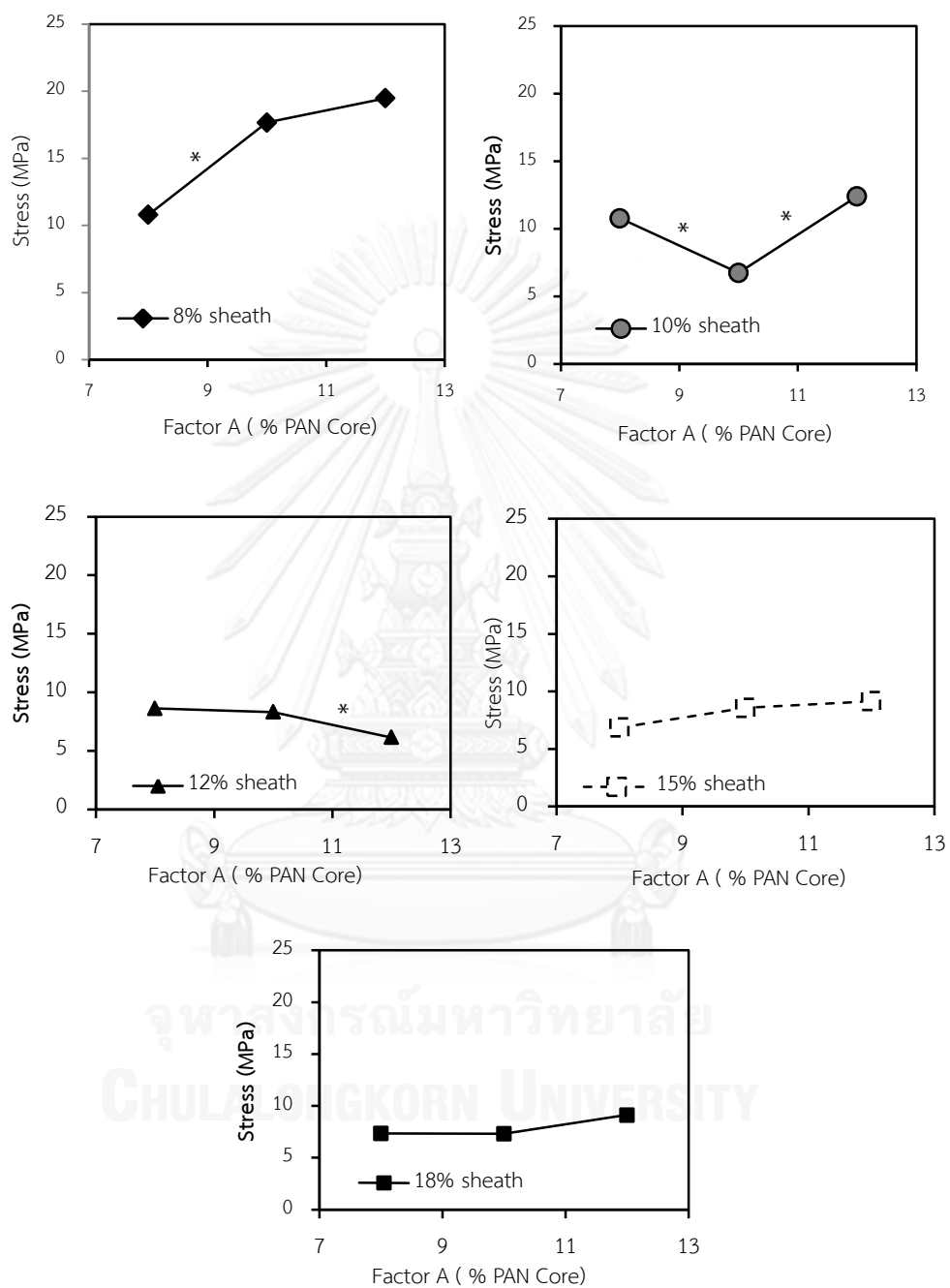
Figure 4-30. Plot of the estimated treatment means shows percentage of PVP sheath curves (Multiple groups comparisons were used one way ANOVA by Bonferroni test *P<0.05).
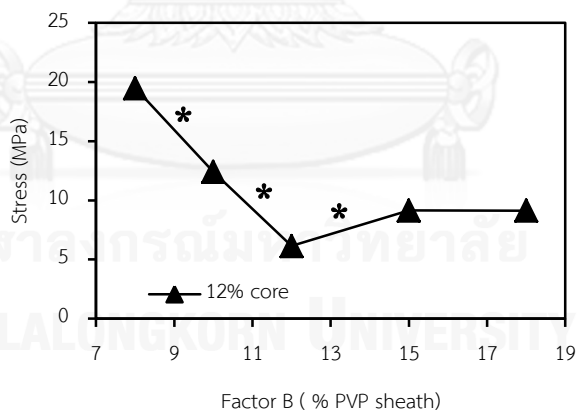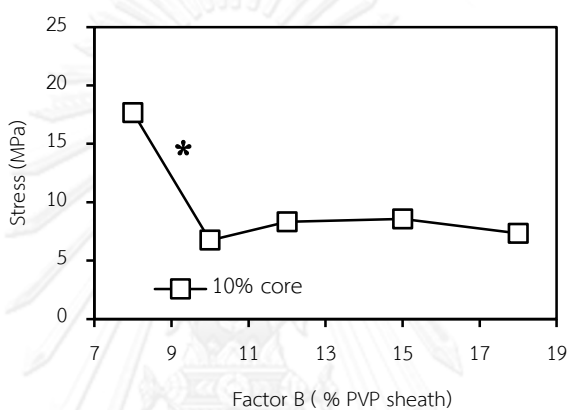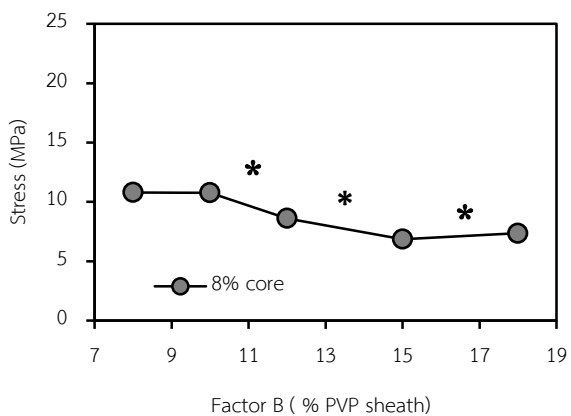
Figure 4-31. Plot of the estimated treatment means shows percentage of PAN core curves. (Multiple groups comparisons were used one way ANOVA by Bonferroni test *P<0.05)

4.3 Photocatalytic degradation of PAN/ZnO co-axial nanofibers

The objects of this study are to fabricate the ZnO/PAN co-axial nanofibers and study effects from variables such as calcination temperature, calcination time and aging time on photocatalytic activity of the products.

The photocatalytic property of ZnO/PAN co-axial nanofibers was studied in comparison with ZnO powder synthesized by the same sol-gel process. All products were calcined at $450^{O}C$ which was considered as the proper temperature sustaining the flexibility of the co-axial fibers.
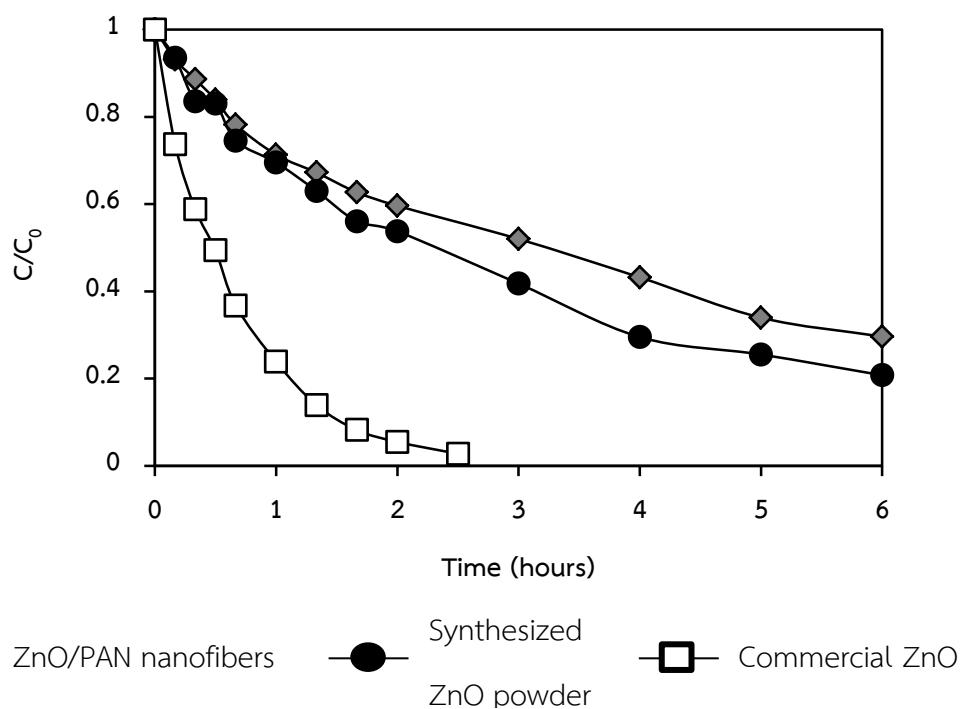
Figure 4-32. Photocatalytic degradation of ZnO/PAN nanofibers, ZnO power and ZnO commercial ($450^{O}C$, 10 ppm dye concentration, 1 mg/ 1 ml of solution)

In order to study the degradation kinetics, a pseudo first order kinetic model was used. The general rate equation is given as $\frac{-dC}{dt} = kCC_{OH*}$ where C is the methylene blue concentration and C_{OH*} the hydroxyl radical concentration. For the pseudo-first order hypothesis which considered C_{OH*} to be constant due to the continuous hydroxyl ion formation by photocatalysis. So the rate depends only on methylene blue concentration giving the rate equation to $-\ln\left(\frac{C}{C_0}\right) = kt$. The plot of C/C_0 as a function of irradiation time was represented in Figure 4-32 where C is the concentration of dye in the reaction mixture and C_0 is the initial concentration of dye. Maximum degradation of 100% was obtained using commercial ZnO as the catalyst for the reaction for 2.5 hours.

The degradation rate data was plotted using pseudo-first order kinetic model in equation (18). The data perfectly fit pseudo-first order kinetics (Figure 4-33) and rate constant of ZnO/PAN nanofibers was 0.218 hour^{-1} as reported in Table 4-7. It was close to the rate constant of ZnO powder synthesized by the same process.
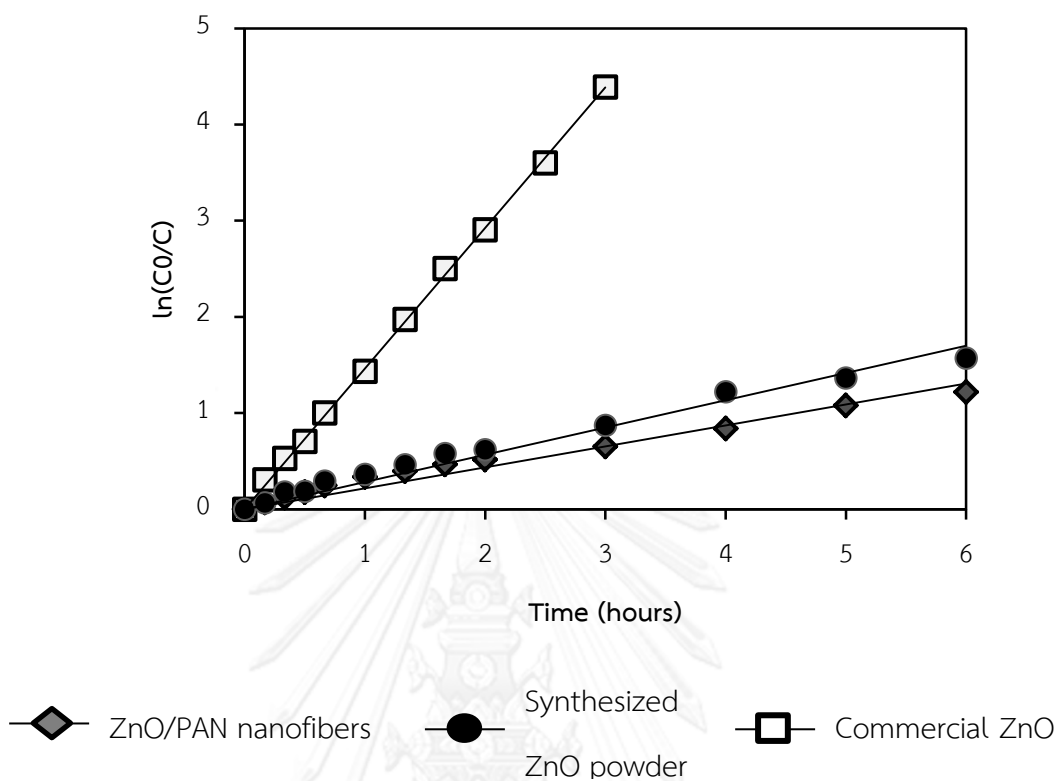
Figure 4-33. Pseudo-first-order kinetic curve fitting of ZnO/PAN nanofibers, ZnO power and ZnO commercial (450°C, 10 ppm dye concentration, 1 mg/ 1 ml of solution)

Table 4-7. Pseudo-first-order kinetic parameters of ZnO/PAN nanofibers, ZnO power

and ZnO commercial (10 ppm dye concentration, 1 mg/ 1 ml of solution)

Product	k (1/hour)	r^2
ZnO/PAN nanofibers	0.218	0.960
Synthesized ZnO power	0.283	0.976
Commercial ZnO	1.462	0.999

It is noted that the photocatalytic activity of ZnO/PAN co-axial nanofibers had a little bit lower than the activity of ZnO powder. The reasons should be the loss of the surface area of ZnO which adhered to the polymer core. Furthermore, the crystal defects were one of the most probable structural features relating to e^--h^+ recombination which retarded the photocatalytic activity [51]. The discussion on crystal defects is presented in the previous section.
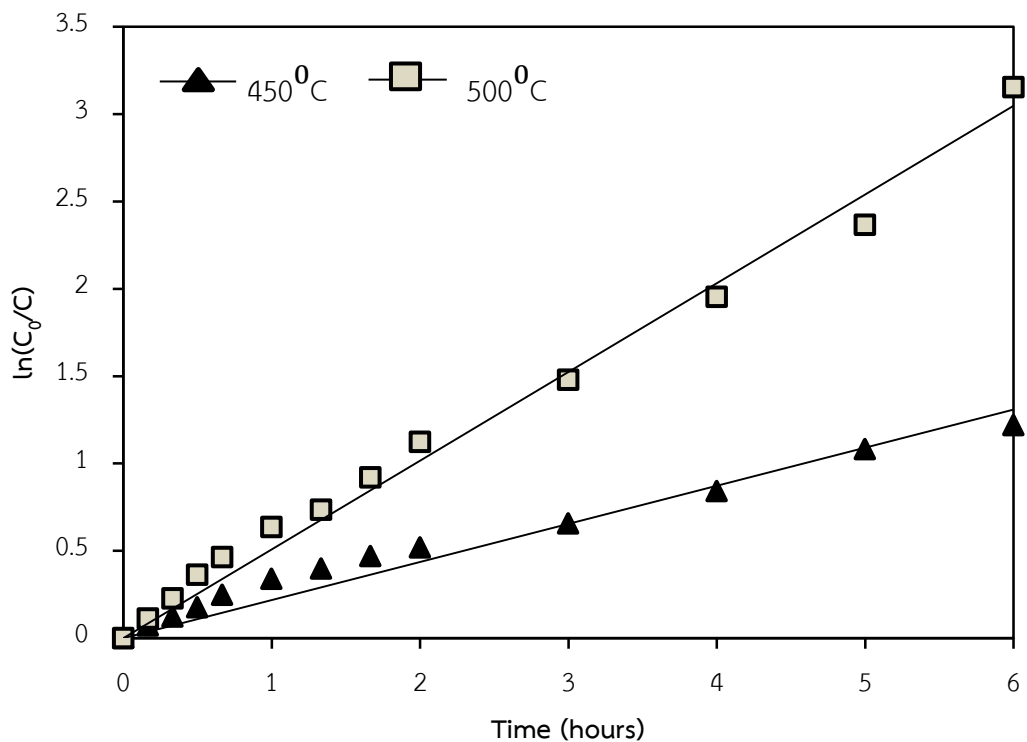
4.3.1 Effect of calcination temperature.

The effect of calcination temperature on the photocatalytic activity is an important parameter to be studied. Calcination at higher temperature induces growth of crystallite and also eliminates some contaminants which often decrease photocatalytic activity.

Plot of C/C_0 versus time is represented in Figure 4-34. The degradation rate data obtained for different calcination temperature i.e., 300, 450, and 500^oC, were plotted using pseudo-first order kinetic model in Figure 4-35. The data perfectly fit pseudo-first order kinetics. The rate constants and r^2 values were tabulated in Table 4-8. The maximum rate constant of 0.508 h^{-1} was observed at calcination temperature of 500^oC. The fairness of the fit is indicated by the fact that linear regression (r^2) values are greater than 0.9. Therefore the model is in good agreement with the experimental data. It should be noted that the calcination temperature below 300^oC is not high enough to convert amorphous ZnO to crystalline ZnO.
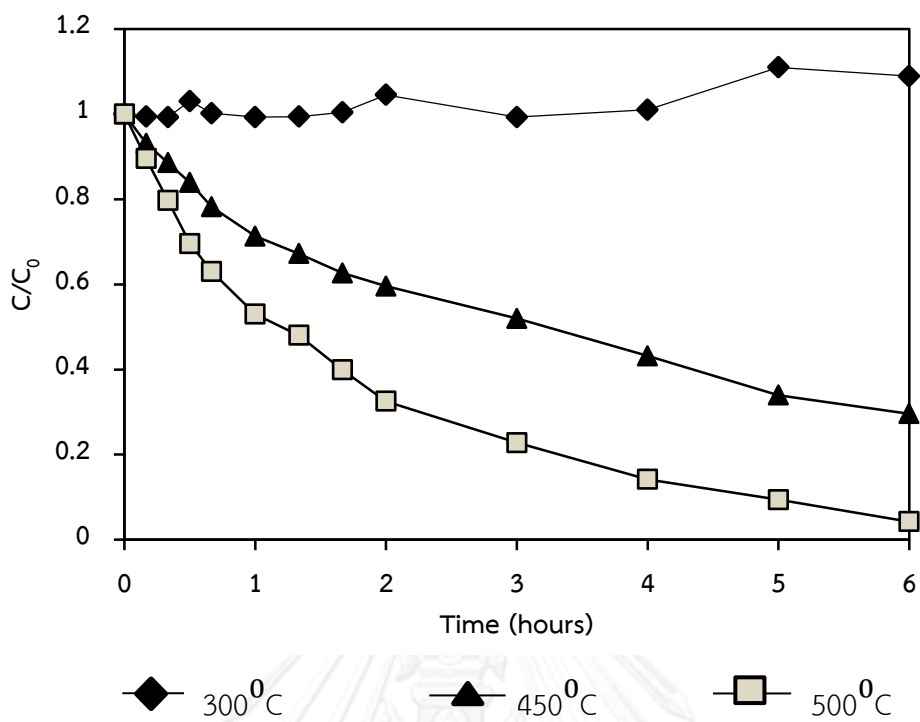
Figure 4-34. Effect of calcination temperature on degradation of MB (10 ppm dye

concentration, 1 mg/ 1 ml of solution)

Figure 4-35. Pseudo-first-order kinetic curve fitting of calcination temperature on

degradation of MB (10 ppm dye concentration, 1 mg/ 1 ml of solution)

Table 4-8. Pseudo-first-order kinetic parameters for degradation of MB at different

calcination temperature (10 ppm dye concentration, 1 mg/ 1 ml of solution)

Calcination temperature (^0C)	k (1/hour)	r^2
400	0.122	0.966
450	0.218	0.960
500	0.508	0.989

The crystalline phase of ZnO is an important factor influencing its photocatalytic activity. According to XRD results shown in Figure 4-36, the co-axial products after calcination at 400 and 450°C (Figure 4-36(c,d)) contain ZnO in wurtzite structure (JCPDS- pattern: 00-036-1451), as well as unidentified crystalline materials (represented by solid markers). On the other hand, calcination at 300°C does not result in any peak indicating the appearance of crystalline material as shown in Figure 4-36b. It is also suggested from the XRD analysis of neat PAN fibers that the core part of the product remains as amorphous phase after the calcination (Figure 4-36 a).

The crystallite size of the ZnO phase calculated by the Debye-Scherrer was found to be 13.1 and 20.8 nm for calcination at 400 and 450°C, respectively. It can be seen that by increasing the temperature, the particle size will increase.
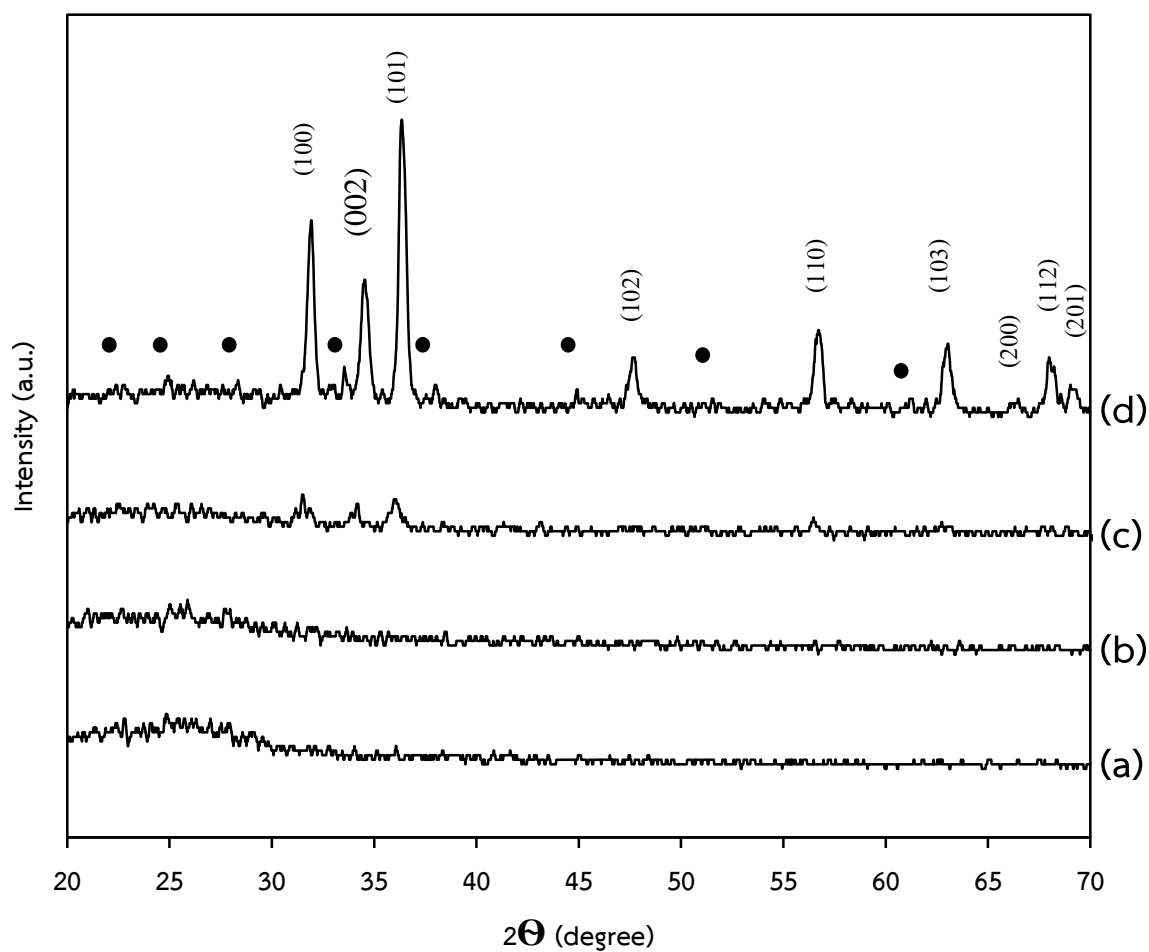
Figure 4-36. XRD patterns of the ZnO/PAN co-axial fibers calcination at (a) 300⁰C, (b)

400⁰C, (c) 450⁰C, and (d) 500⁰C

4.3.2 Effect of calcination time

Experiments were conducted to study the effect of calcination time on degradation of MB. The calcination time was varied from 2 to 6 hours. Plot of C/C_0 versus time is represented in Figure 4-37. According to the data, an increase in the calcination time leads to increase the rate of its degradation. However the range of 2 to 3 hours does not give significantly different results.
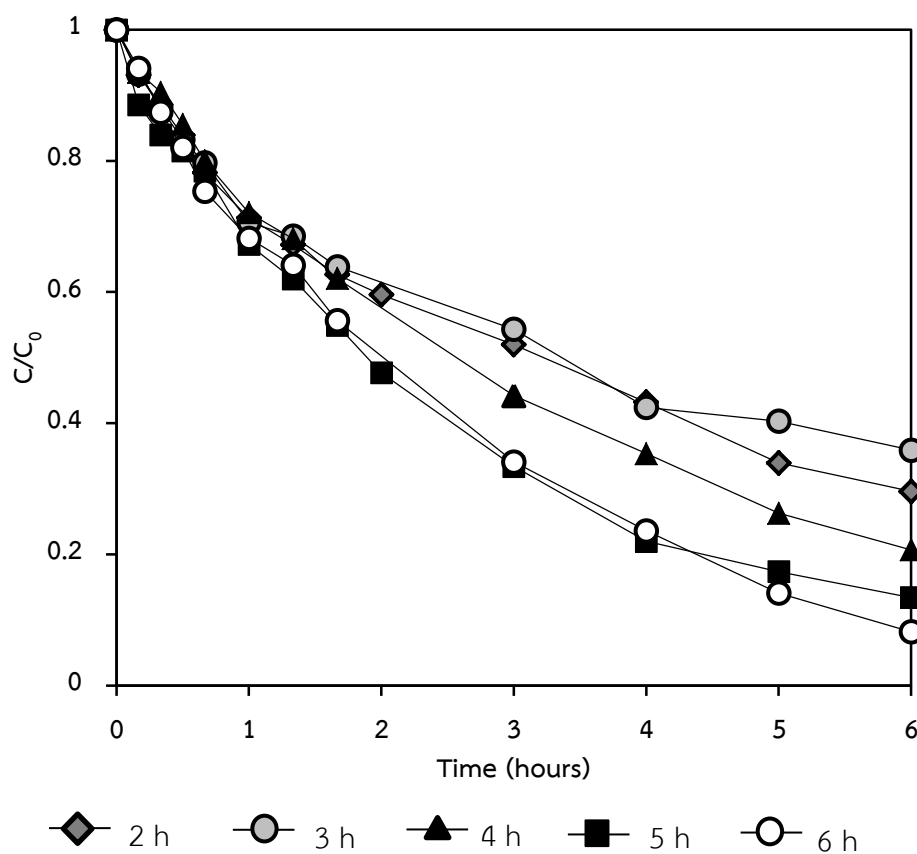
Figure 4-37. Effect of calcination time on degradation of MB (450°C, 10 ppm dye concentration, 1 mg/ 1 ml of solution)
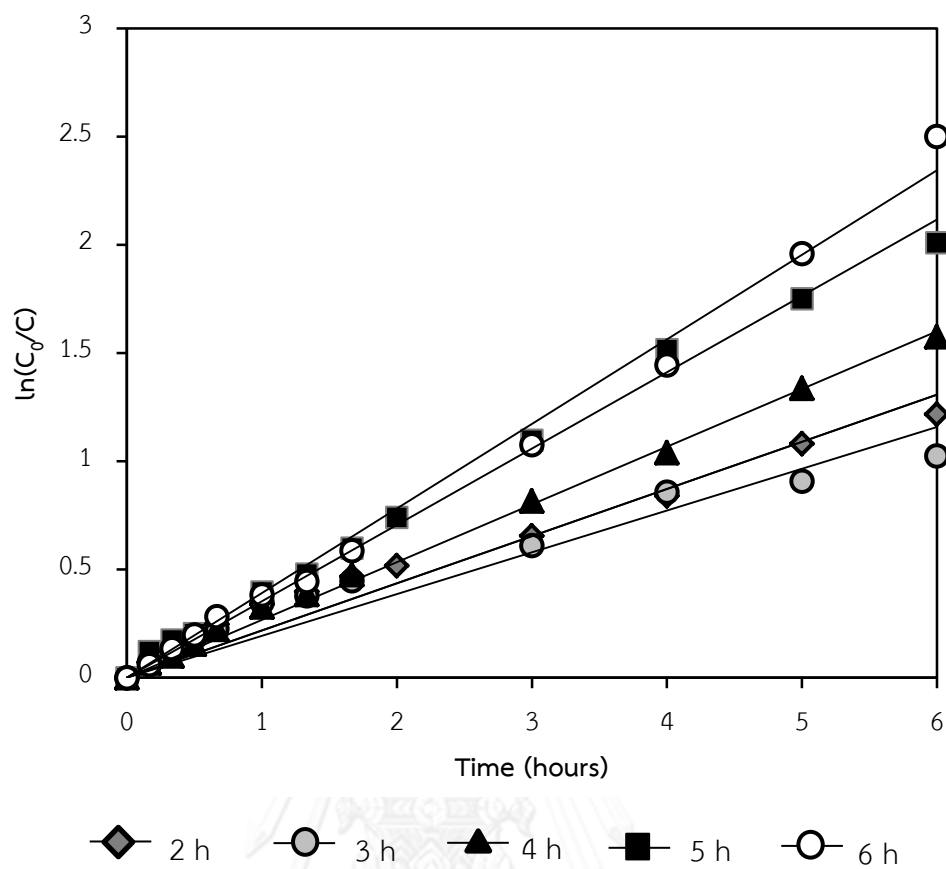
Figure 4-38. Pseudo-first-order kinetic curve fitting of calcination time on degradation

of MB (450°C, 10 ppm dye concentration, 1 mg/ 1 ml of solution)

Table 4-9. Pseudo-first-order kinetic parameters for degradation of MB at different calcination time (10 ppm dye concentration, 1 mg/ 1 ml of solution)
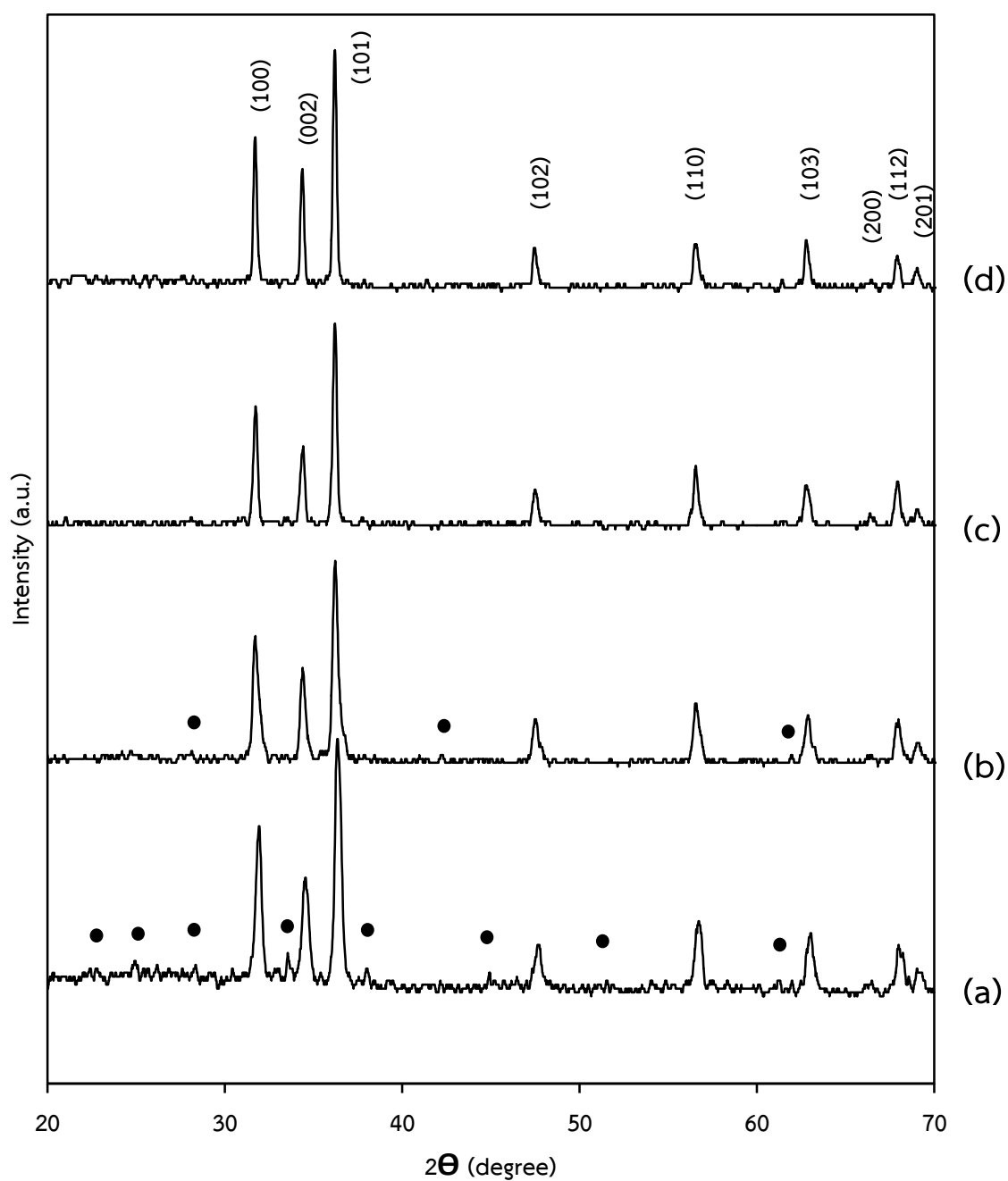
Calcination time (hours)	k (1/hour)	r^2
2	0.218	0.960
3	0.193	0.919
4	0.267	0.997
5	0.353	0.993
6	0.391	0.992

The degradation rate data obtained for different calcination time were plotted using pseudo-first order kinetic model. The data perfectly fit pseudo-first order kinetics (Figure 4-38) and rate constant data is tabulated in Table 4-9. The apparent rate constant of 0.391 h^{-1} was found to be the maximum obtained 6 hours of calcination time. The fairness of the fit is indicated by the fact that linear regression (r^2) values are greater than 0.9. Therefore the model is in good agreement with the experimental data.

X-ray diffraction patterns of ZnO /PAN nanofibers are illustrated in Figure 4-39. All peaks can be well indexed to the wurtzite phase of ZnO (JCPDS- pattern: 00-036-1451). The amorphous from polymer core including unidentified peaks (black spots)

have been appeared in co-axial nanofibers after calcined at 450^{0}C. The more prolongation of calcinations time was applied, the less in impurities were appeared.

The effect of calcinations time upon the grain size of ZnO is shown in Table 4-10 and Figure 4-40. At 450°C the calcination time is influence upon the grain size. The time yields the larger grain size. There was a little influence from 2 to 3 hours, but it increased markedly between 3 and 4 hours and rose gradually from 4 to 5 hours. Due to the longer time of calcination caused the grain growth to result in a better crystallinity. The results are in good accordance with photocatalytic degradation of MB in Figure 4-37.

Figure 4-39. XRD patterns of the ZnO/PAN co-axial fibers calcination at $450\,^{0}\mathrm{C}$ for (a)

2 hours, (b) 3 hours, (c) 4 hours, and (d) 5 hours

Table 4-10. Crystallite sizes of the ZnO/PAN co-axial fibers calcination at 450°C at different calcination time.

Calcination Time (hour)	Grain size (nm)
2	20.8
3	23.3
4	34.3
5	38.9
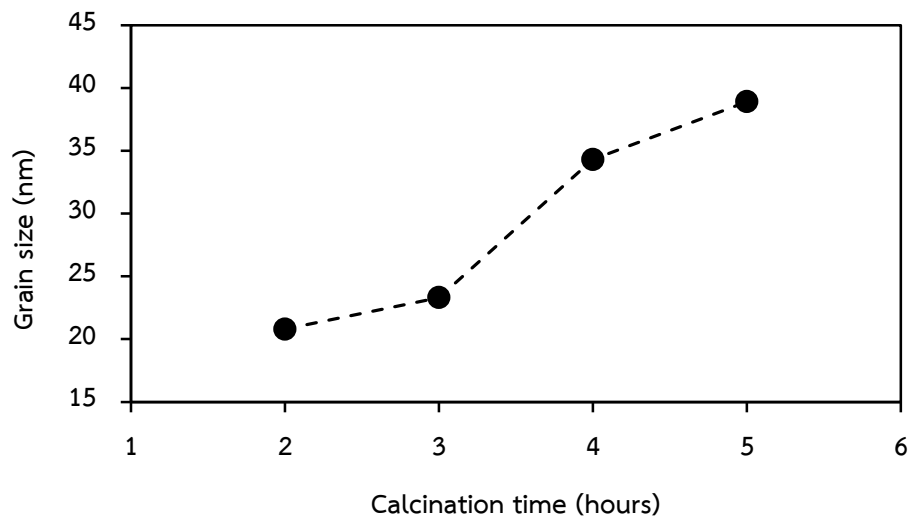
**Figure 4-40.** Trend of grain size at different calcination time

4.3.3 Effect of aging time

ZnO in the sheath was prepared by sol-gel method. The effect of sol aging time was investigated. In this study, it was serendipitously found that sol aging time of 7 days could be fabricated into the co-axial fibers and yielded the high photocatalytic activity rather than the one that was not aged. Figure 4-41, shows the C/C_0 plots of different aging time of ZnO sol namely no aging, 4, and 7 days. The rate constants and r^2 values were tabulated in table 4-11.
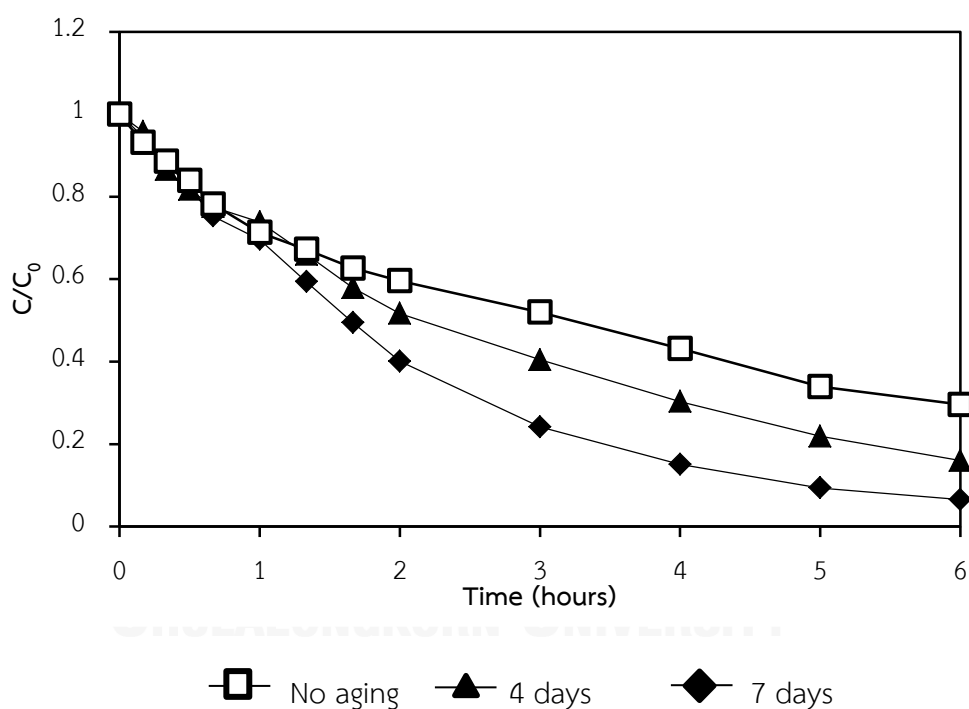
Figure 4-41. Effect of aging time on degradation of MB (450°C, 10 ppm dye concentration, 1 mg/ 1 ml of solution)
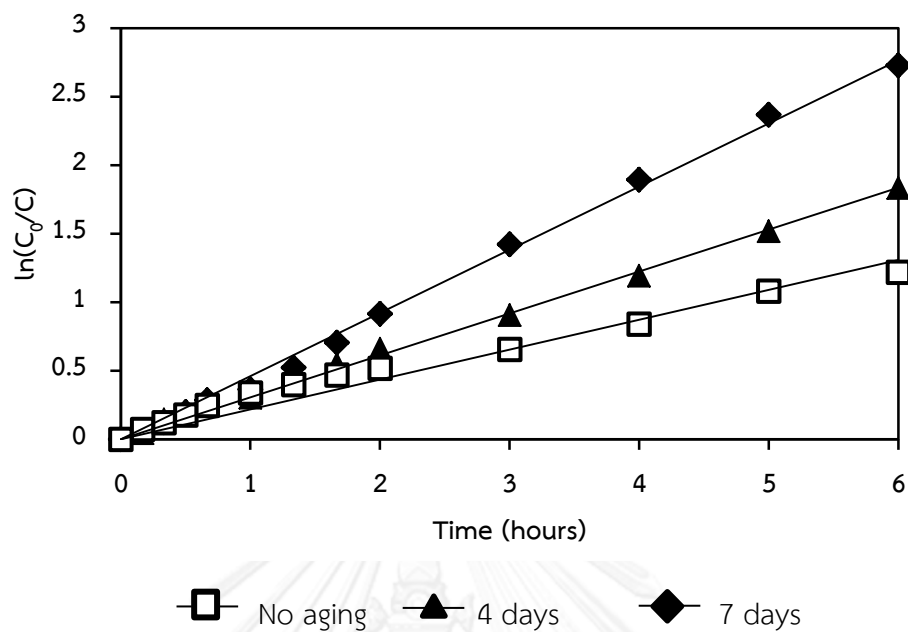
Figure 4-42. Pseudo-first-order kinetic curve fitting of aging sol time on degration of

MB (450°C, 10 ppm dye concentration, 1 mg/ 1 ml of solution)

Table 4-11. Crystallite sizes of the ZnO/PAN co-axial fibers calcination at 450°C at

different aging sol time

Aging time (days)	k (1/hour)	r^2
No aging	0.218	0.960
4	0.306	0.997
7	0.461	0.996

According to the XRD in Figure 4-43, the crystallite size of the ZnO phase calculated by the Debye-Scherrer was found to be 20.8 and 36.6 nm for aging time at no aging and 7 days, respectively. It can be concluded that the increase in aging time renders grain growth by Ostwald ripening and aggregation as described in Chapter 2.

There are interesting factors which have influent on the photocatalytic activity of ZnO/PAN co-axial nanofibers such as calcination temperature, calcination time, aging time and etc. It can conduct the experiment to find the high photocatalytic activity. But one must bear in mind that there are many constraints such as the flexibility of fibers, the potential ZnO crystalline to yield the successful products.
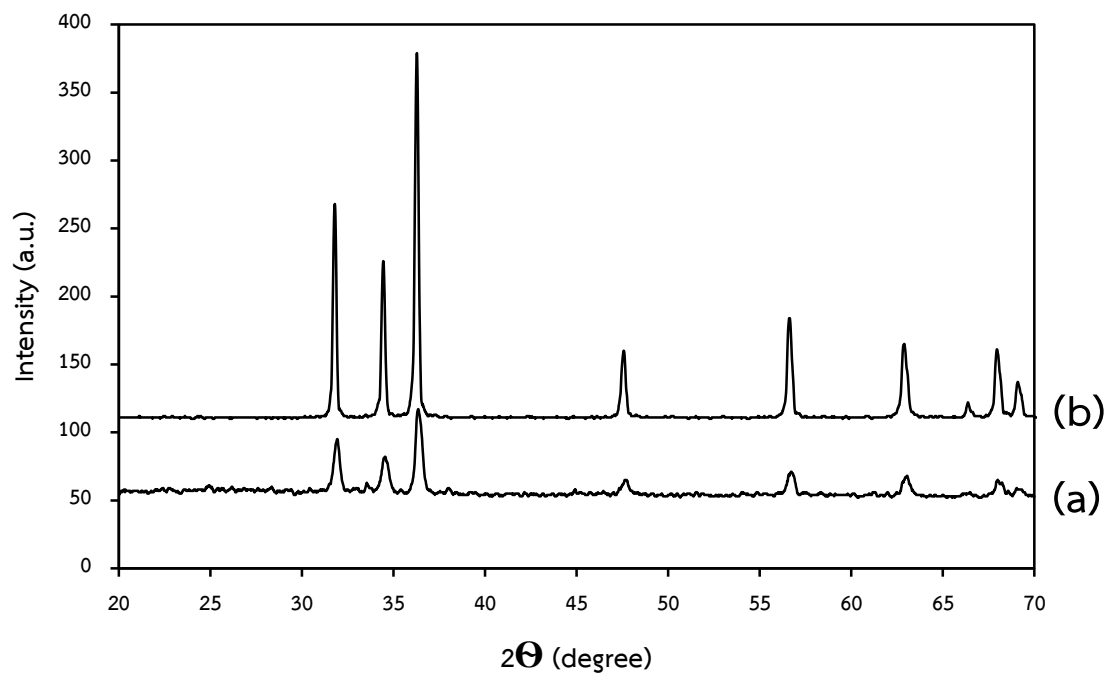
Figure 4-43. XRD patterns of the ZnO/PAN co-axial fibers calcination at 450⁰C for

aging time of (a) no aging, (b) 7 days

CHAPTER V

CONCLUSION AND RECOMMENDATIONS

5.1 Summary of the results

1. The fabrication of ZnO/PAN co-axial nanofibers have been accomplished via the combination of sol-gel method and electrospinning technique yielding the uniform and bead-free fibers

2. Viscosity of both the core and the sheath solution has influence on the core-sheath structure of fibers. The viscosity of sheath solution is required to be higher than the viscosity of core solution.

3. By varying percentage of the polymer content in core and the sheath solution, it was found that the overall fiber diameter is affected more significantly by core concentration rather than by the sheath concentration. Accordingly the PAN core concentration is the significant factor to predict the diameter of co-axial fibers.

4. The diameter of the ZnO/PAN co-axial nanofibers depends on the viscosity and concentration of solutions. The average diameter of the as-spun co-axial nanofibers is in the range of 216±31 to 1,403±194 nm.

5. The ZnO in Wurtzite phase distributing on PAN core can be obtained after calcination at 450°C. The synthesized ZnO co-axial nanofibers had crystallite size of 21 nm.

6. The PAN/ZnO core/sheath nanofibers are still flexible after being calcined at 450°C. The mechanical properties of the fibers, such as yield strain and yield stress, are affected by PAN core concentration and PVP sheath concentration.

7. The photocatalytic activity of ZnO/PAN co-axial is slightly lower than that of ZnO powder.

8. The photocatalytic activity of fibers depends on calcination temperature, calcination time, and aging time sol.

5.2 Conclusions

In this study, the flexible PAN/ZnO core/sheath coaxial nanofibers were successfully prepared by combined sol-gel process and co-axial electrospinning, yielding the smooth surface, bead-free and uniform fibers. The core/sheath structure was formed before the calcination and was retained after the calcination. Even after the calcination at relatively high temperature to convert ZnO sols into wurtzite phase, the PAN core is still present to provide flexibility of the fibers. The photocatalytic degradation of methylene blue of ZnO/PAN fibers is slightly lower than the activity of ZnO powder. The photocatalytic activity of ZnO/PAN co-axial

fibers depends on calcination temperature, prolongation of calcination time, and aging sol time.

5.3 Recommendations for the Future Studies

There are some recommendations for future studies given below.

1. Co-axial electrospinning process is a very complex process with more variables affecting output parameters than those were tested in this study such as feeding flow rate for each of polymers, applied voltage. Effect of these parameters should be studied.

2. The effect of aging time should be pursued in order to draw stronger conclusions on the photodegradation activity

REFERENCES

1. Kim, T.-H. and B.-H. Sohn, *Photocatalytic thin films containing TiO< sub> 2</sub> nanoparticles by the layer-by-layer self-assembling method.* Applied surface science, 2002. **201**(1): p. 109-114.

2. Ohyama, M., H. Kouzuka, and T. Yoko, *Sol-gel preparation of ZnO films with extremely preferred orientation along (002) plane from zinc acetate solution.* Thin solid films, 1997. **306**(1): p. 78-85.

3. Znaidi, L., *Sol–gel-deposited ZnO thin films: a review.* Materials Science and Engineering: B, 2010. **174**(1): p. 18-30.

4. Zhang, Q., W. Fan, and L. Gao, *Anatase TiO< sub> 2</sub> nanoparticles immobilized on ZnO tetrapods as a highly efficient and easily recyclable photocatalyst.* Applied Catalysis B: Environmental, 2007. **76**(1): p. 168-173.

5. Alves, A., et al., *Photocatalytic activity of titania fibers obtained by electrospinning.* Materials Research Bulletin, 2009. **44**(2): p. 312-317.

6. Ozgur, U., et al., *A comprehensive review of ZnO materials and devices.* Journal of applied physics, 2005. **98**(4): p. 041301-041301-103.

7. Wang, Z.L., *Zinc oxide nanostructures: growth, properties and applications.* Journal of Physics: Condensed Matter, 2004. **16**(25): p. R829.

8. Ouyang, Q., et al., *Mechanism and kinetics of the stabilization reactions of itaconic acid-modified polyacrylonitrile.* Polymer Degradation and Stability, 2008. **93**(8): p. 1415-1421.

9. Korobeinyk, A.V., R.L. Whitby, and S.V. Mikhalovsky, *High temperature oxidative resistance of polyacrylonitrile-methylmethacrylate copolymer powder converting to a carbonized monolith.* European Polymer Journal, 2012. **48**(1): p. 97-104.

10.   Haaf, F., A. Sanner, and F. Straub, *Polymers of N-vinylpyrrolidone: synthesis, characterization and uses.* Polymer Journal, 1985. **17**(1): p. 143-152.

11.   Lee, H.-J., et al., *Gas permeation properties of carbon molecular sieving membranes derived from the polymer blend of polyphenylene oxide (PPO)/polyvinylpyrrolidone (PVP).* Journal of Membrane Science, 2007. **296**(1–2): p. 139-146.

12.   Silva, M.F., et al., *Thermal and FTIR study of polyvinylpyrrolidone/lignin blends.* Journal of Thermal Analysis and Calorimetry, 2005. **79**(2): p. 367-370.

13.   Levy, D. and L. Esquivias, *Sol–gel processing of optical and electrooptical materials.* Advanced Materials, 1995. **7**(2): p. 120-129.

14.   Tseng, T.K., et al., *A review of photocatalysts prepared by sol-gel method for VOCs removal.* International journal of molecular sciences, 2010. **11**(6): p. 2336-2361.

15.   Mehrotra, R., *Present status and future potential of the Sol-Gel process*, in *Chemistry, Spectroscopy and Applications of Sol-Gel Glasses*. 1992, Springer. p. 1-36.

16.   Hench, L.L. and J.K. West, *The sol-gel process.* Chemical Reviews, 1990. **90**(1): p. 33-72.

17.   Hohman, M.M., et al., *Electrospinning and electrically forced jets. II. Applications.* Physics of Fluids, 2001. **13**: p. 2221.

18.   Lee, K., et al., *The change of bead morphology formed on electrospun polystyrene fibers.* Polymer, 2003. **44**(14): p. 4029-4034.

19.   Fong, H., I. Chun, and D. Reneker, *Beaded nanofibers formed during electrospinning.* Polymer, 1999. **40**(16): p. 4585-4592.

20.   Deitzel, J., et al., *The effect of processing variables on the morphology of electrospun nanofibers and textiles.* Polymer, 2001. **42**(1): p. 261-272.

21.   Shenoy, S.L., et al., *Role of chain entanglements on fiber formation during electrospinning of polymer solutions: good solvent, non-specific polymer–polymer interaction limit.* Polymer, 2005. **46**(10): p. 3372-3384.

22.   Munir, M.M., et al., *Scaling law on particle-to-fiber formation during electrospinning.* Polymer, 2009. **50**(20): p. 4935-4943.

23.   Yang, Q., et al., *Influence of solvents on the formation of ultrathin uniform poly (vinyl pyrrolidone) nanofibers with electrospinning.* Journal of Polymer Science Part B: Polymer Physics, 2004. **42**(20): p. 3721-3726.

24.   Teo, W. and S. Ramakrishna, *A review on electrospinning design and nanofibre assemblies.* Nanotechnology, 2006. **17**(14): p. R89.

25.   Zander, N.E., *Hierarchically Structured Electrospun Fibers.* Polymers, 2013. **5**(1): p. 19-44.

26.   Greiner, A., et al., *Biohybrid nanosystems with polymer nanofibers and nanotubes.* Applied microbiology and biotechnology, 2006. **71**(4): p. 387-393.

27.   Chakraborty, S., et al., *Electrohydrodynamics: A facile technique to fabricate drug delivery systems.* Advanced drug delivery reviews, 2009. **61**(12): p. 1043-1054.

28.   Li, D. and Y. Xia, *Direct fabrication of composite and ceramic hollow nanofibers by electrospinning.* Nano Letters, 2004. **4**(5): p. 933-938.

29.   Moghe, A. and B. Gupta, *Co‑axial Electrospinning for Nanofiber Structures: Preparation and Applications.* Polymer Reviews, 2008. **48**(2): p. 353-377.

30.   Yu, J.H., S.V. Fridrikh, and G.C. Rutledge, *Production of submicrometer diameter fibers by two‑fluid electrospinning.* Advanced Materials, 2004. **16**(17): p. 1562-1566.

31.   Díaz, J.E., et al., *Controlled encapsulation of hydrophobic liquids in hydrophilic polymer nanofibers by co‑electrospinning.* Advanced Functional Materials, 2006. **16**(16): p. 2110-2116.

32.   McCann, J.T., M. Marquez, and Y. Xia, *Melt coaxial electrospinning: a versatile method for the encapsulation of solid materials and fabrication of phase change nanofibers.* Nano letters, 2006. **6**(12): p. 2868-2872.

33.   Zhang, Y., et al., *Preparation of core-shell structured PCL-r-gelatin bi-component nanofibers by coaxial electrospinning.* Chemistry of Materials, 2004. **16**(18): p. 3406-3409.

34.   He, C.L., et al., *Coaxial electrospun poly (L‑lactic acid) ultrafine fibers for sustained drug delivery.* Journal of Macromolecular Science Part B--Physics, 2006. **45**(4): p. 515-524.

35.   Sun, Z., et al., *Compound Core–Shell Polymer Nanofibers by Co‑Electrospinning.* Advanced Materials, 2003. **15**(22): p. 1929-1932.

36.   Li, D., et al., *Nanofibers of conjugated polymers prepared by electrospinning with a two‑capillary spinneret.* Advanced materials, 2004. **16**(22): p. 2062-2066.

37.   Larsen, G., R. Spretz, and R. Velarde‑Ortiz, *Use of coaxial gas jackets to stabilize Taylor cones of volatile solutions and to induce particle‑to‑fiber transitions.* Advanced Materials, 2004. **16**(2): p. 166-169.

38.   Linsebigler, A.L., G. Lu, and J.T. Yates Jr, *Photocatalysis on TiO2 surfaces: principles, mechanisms, and selected results.* Chemical Reviews, 1995. **95**(3): p. 735-758.

39.   Herrmann, J.-M., *Heterogeneous photocatalysis: fundamentals and applications to the removal of various types of aqueous pollutants.* Catalysis Today, 1999. **53**(1): p. 115-129.

40.   Konstantinou, I.K. and T.A. Albanis, *TiO< sub> 2</sub>-assisted photocatalytic degradation of azo dyes in aqueous solution: kinetic and mechanistic investigations: A review.* Applied Catalysis B: Environmental, 2004. **49**(1): p. 1-14.

41.   Bhatkhande, D.S., V.G. Pangarkar, and A.A. Beenackers, *Photocatalytic degradation for environmental applications–a review.* Journal of Chemical Technology and Biotechnology, 2002. **77**(1): p. 102-116.

42.   Wang, J., et al., *Oxygen vacancy induced band-gap narrowing and enhanced visible light photocatalytic activity of ZnO.* ACS applied materials & interfaces, 2012. **4**(8): p. 4024-4030.

43.   Moezzi, A., A.M. McDonagh, and M.B. Cortie, *Zinc oxide particles: Synthesis, properties and applications.* Chemical Engineering Journal, 2012. **185**: p. 1-22.

44.   Bajaj, P., D. Paliwal, and A. Gupta, *Acrylonitrile–acrylic acids copolymers. I. Synthesis and characterization.* Journal of Applied polymer science, 1993. **49**(5): p. 823-833.

45.   Wangxi, Z., L. Jie, and W. Gang, *Evolution of structure and properties of PAN precursors during their conversion to carbon fibers.* Carbon, 2003. **41**(14): p. 2805-2812.

46.   Lee, S., et al., *Structural evolution of polyacrylonitrile fibers in stabilization and carbonization.* Advances in Chemical Engineering and Science, 2012. **2**: p. 275.

47.   Kakida, H. and K. Tashiro, *Mechanism and kinetics of stabilization reactions of polyacrylonitrile and related copolymers III. Comparison among the various types of copolymers as viewed from isothermal DSC thermograms and FT-IR spectral changes.* Polymer journal, 1997. **29**(7): p. 557-562.

48.   Zhu, D., et al., *Oxidative stabilization of PAN/VGCF composite.* Journal of applied polymer science, 2003. **87**(13): p. 2063-2073.

49.   Dalton, S., F. Heatley, and P.M. Budd, *Thermal stabilization of polyacrylonitrile fibres.* Polymer, 1999. **40**(20): p. 5531-5543.

50.   Miao, P., et al., *Influence of electron beam pre-irradiation on the thermal behaviors of polyacrylonitrile.* Polymer Degradation and Stability, 2010. **95**(9): p. 1665-1671.

51.   Beattie, A. and P. Landsberg, *One-dimensional overlap functions and their application to Auger recombination in semiconductors.* Proceedings of the Royal Society of London. Series A. Mathematical and Physical Sciences, 1960. **258**(1295): p. 486-495.

APPENDIX

APPENDIX A

Statistical analysis of effect of polymer concentration on morphology of fibers

The fixed analysis of variance (ANOVA) model for two-factor studies was used to determine the interaction between the effects of PAN concentration and PVP concentration on average diameter of the fibers. The PAN concentration was studied at 3 levels, i.e., 8, 10, and 12 %, while the PVP concentration was studied at 5 levels, i.e., 8, 10, 12, 15 and 18 %. The number of cases for each of 15 treatments is 30. Table A-1. shows the average diameter of fibers after calcination at 450°c for 2 hours.

Table A-1. Summary of average diameter for ANOVA analysis

PAN core concentration (wt%)	PVP sheath concentration (wt%)	Average fibers diameter (nm)
8	8	216 ± 31
	10	319 ± 91
	12	369 ± 75
	15	304 ± 48
	18	323 ± 74
10	8	592 ± 148
	10	703 ± 153
	12	569 ± 108
	15	521 ± 155
	18	1233 ± 219
12	8	571 ± 120
	10	1092 ± 243
	12	750 ± 318
	15	1058 ± 230
	18	1403 ± 194

Table A- 2. ANOVA table for average diameter

Source of Variation	Sum of squares	Degree of freedom	MS	F*	Percentiles of the F distribution
Factor A (Core)	2280680	2	12.47	43.12	F(0.95,2,435) =3
Factor B (sheath)	953019	4	6.24	9.01	F(0.95,4,435) =2.37
AB interactions	54144212	8	1.97	255.92	F(0.95,8,435) = 1.94
Error	11503851	435	0.24		
Total	68881763	449			
SSTR	57377912				

Five curves in Figure A-1 represent results using different percentage of PVP sheath, while Figure A-2, shows three curves representing result using the different percentage of PAN core. The overlap of some curves confirms the presence of interaction effects between PAN core concentration and PVP sheath concentration on diameter of fibers. A formal test for interactions confirms by two-way ANOVA. As seen in Table 2, F^* =255.92 **>** 1.94, it concludes that interaction effects are present at 95% confidence levels. It also concludes that both of main effects are important due to F^* =43.12 **>**3 for PAN concentration in the core solution and F^* =9.01 **>** 2.37 for PVP concentration in the sheath solution.

Figure A-1 and A-2 suggest that the interactions are important. Multiple group comparisons were used one way ANOVA by Bonferroni test confidence coefficient of

95% to express the significant difference of data. It can be marked that the percentage of PAN in core solution influences diameter of fibers more significantly than the effect of sheath solution.
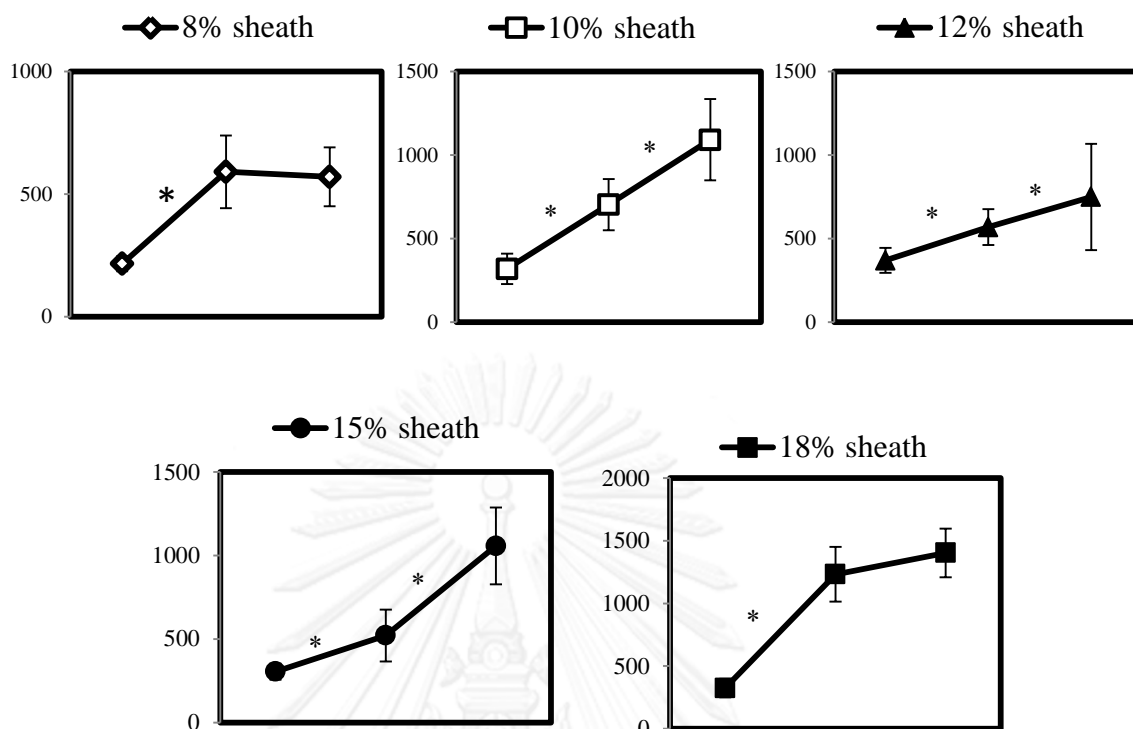
Figure A-1. Plot of the average diameter shows percentage of PVP sheath curves

(Multiple groups comparisons were used one way ANOVA by Bonferroni test *P<0.05).
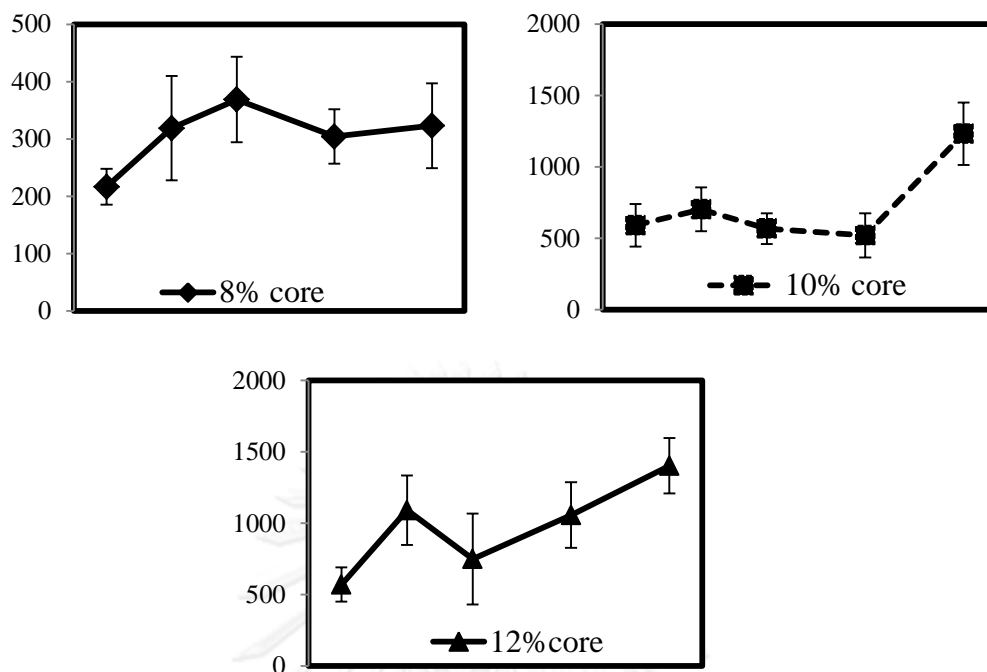
Figure A-2. Plot of the average diameter shows percentage of PAN core curves.

(Multiple groups comparisons were used one way ANOVA by Bonferroni test *P<0.05)

APPENDIX B

TGA THERMOGRAMS OF pristine PAN AND PVP fibers
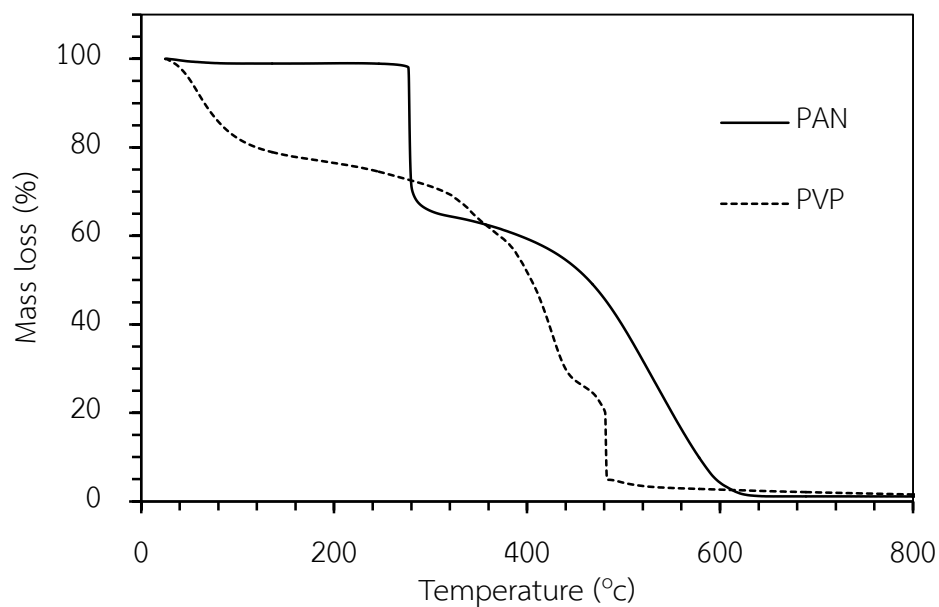
Figure B-1. TGA thermogram of pristine PAN and PVP fibers
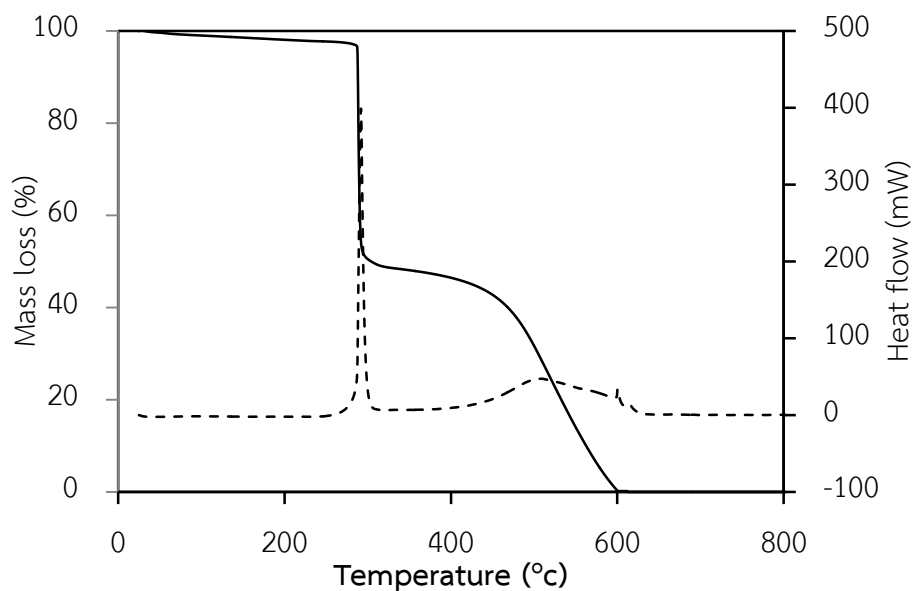
Figure B-2. Thermal gravimetric analysis (TGA) and differential scanning calorimetry

(DSC) of pristine PAN fibers
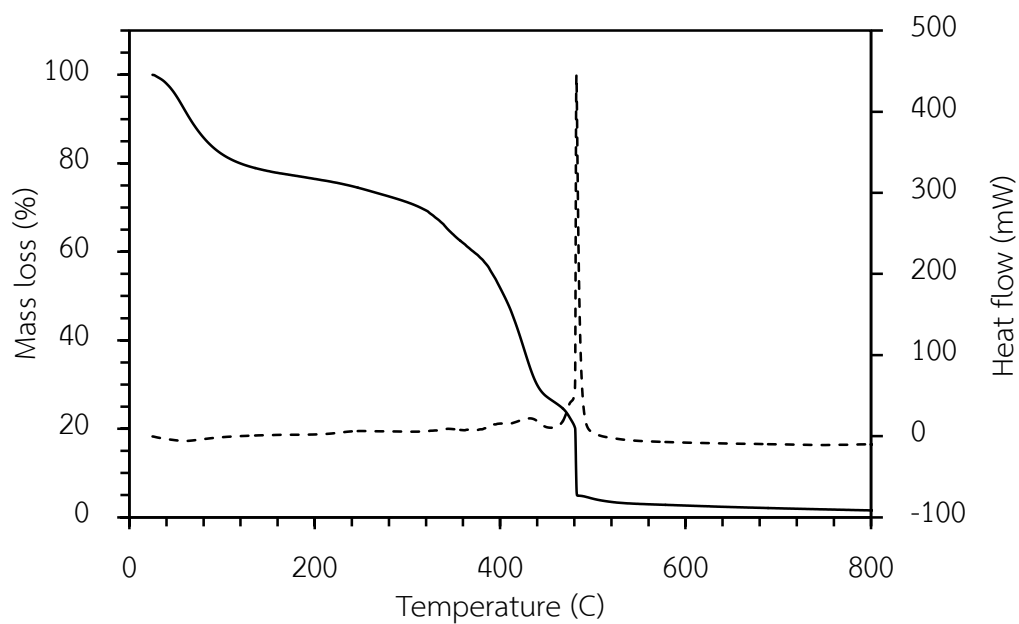
Figure B-3. Thermal gravimetric analysis (TGA) and differential scanning calorimetry

(DSC) of pristine PVP fibers

APPENDIX C
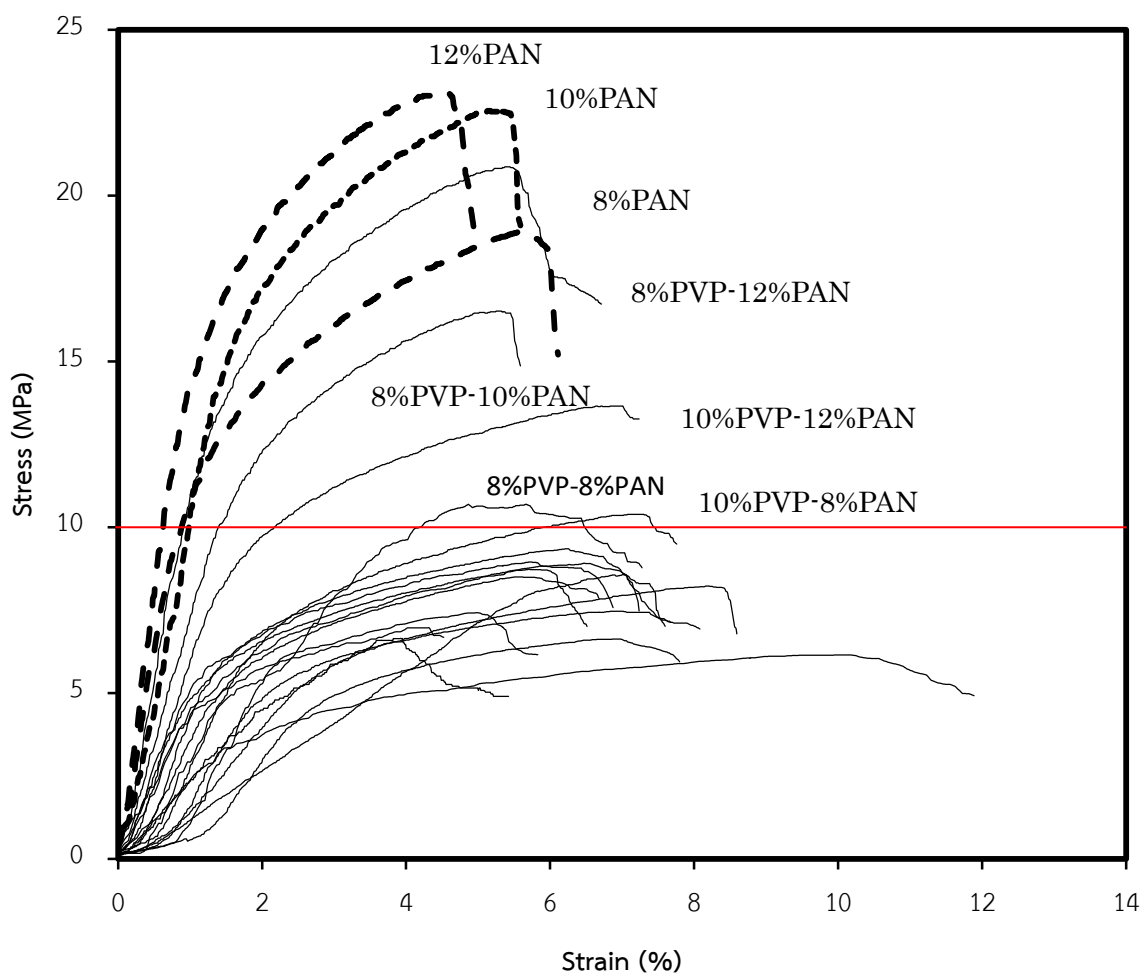
Figure C-1. Stress-strain curves of co-axial fibers after it had been calcined at 450⁰C (all conditions).
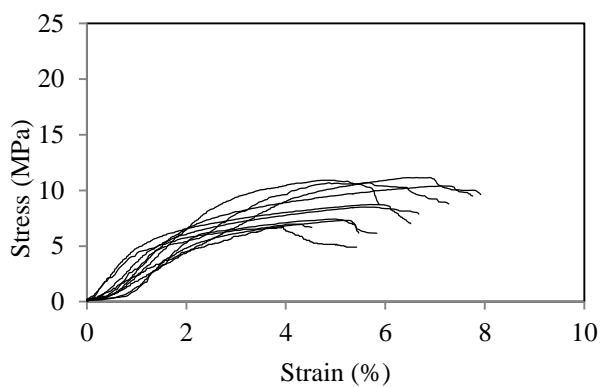
Figure C-2. Stress-strain curves of co-axial fibers 8% PAN after calcined at 450⁰C
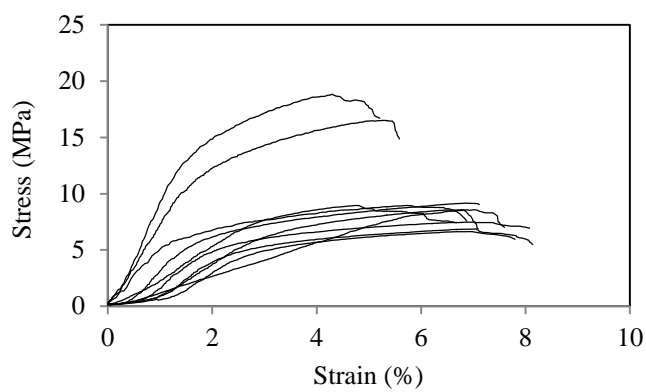
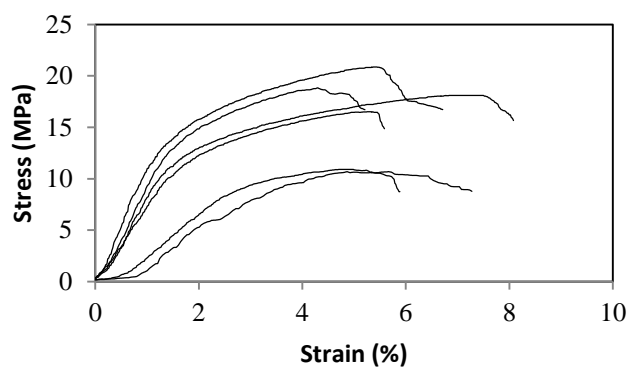**Figure C-3.** Stress-strain curves of co-axial fibers 10% PAN after calcined at 450⁰C
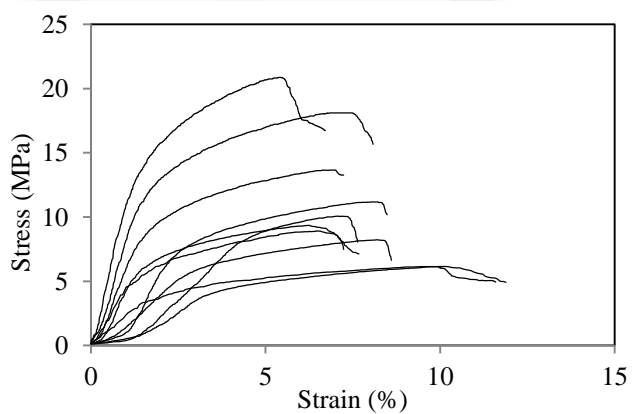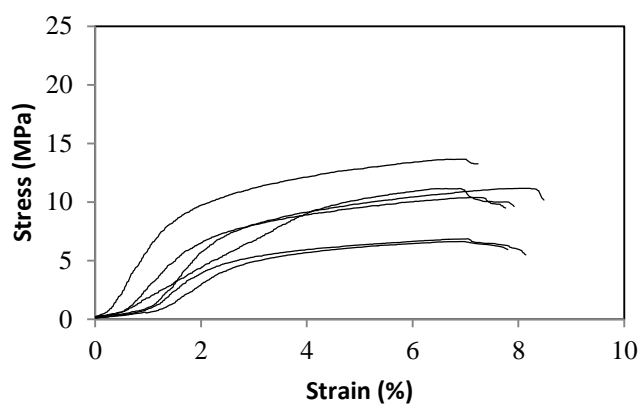

Figure C-4. Stress-strain curves of co-axial fibers 12% PAN after calcined at 450⁰C

Figure C-5. Stress-strain curves of co-axial fibers 8% PVP after calcined at 450⁰C

Figure C-6. Stress-strain curves of co-axial fibers 10% PVP after calcined at 450⁰C
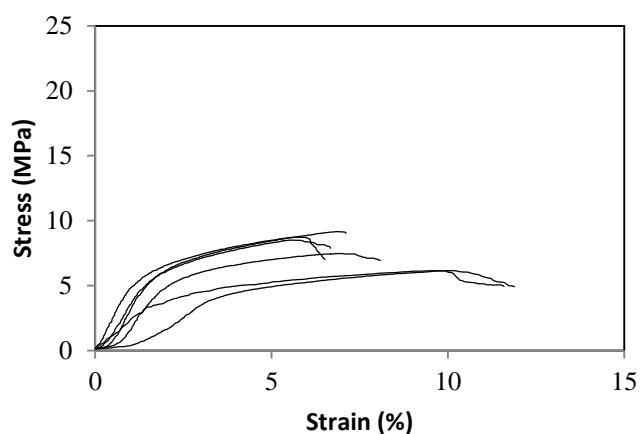

Figure C-7. Stress-strain curves of co-axial fibers 12% PVP after calcined at 450⁰C
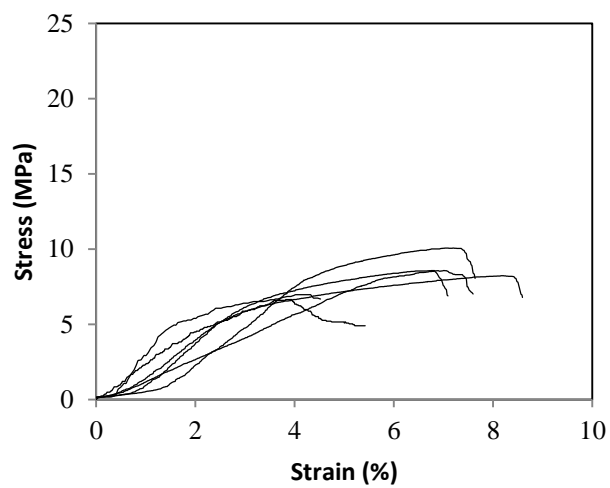
Figure C-8. Stress-strain curves of co-axial fibers 15% PVP after calcined at 450⁰C
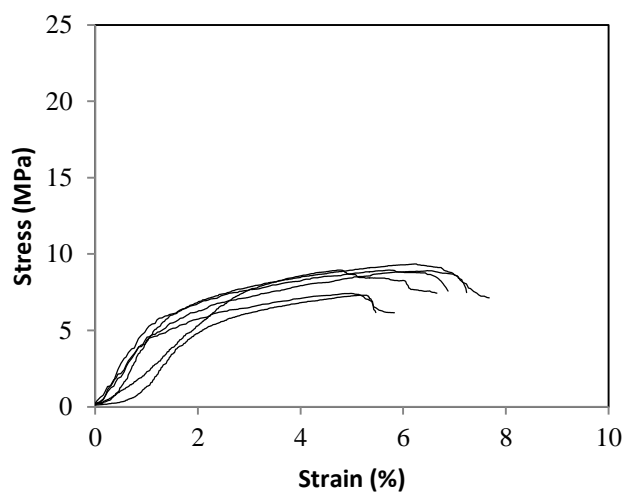

Figure C-9. Stress-strain curves of co-axial fibers 18% PVP after calcined at 450⁰C
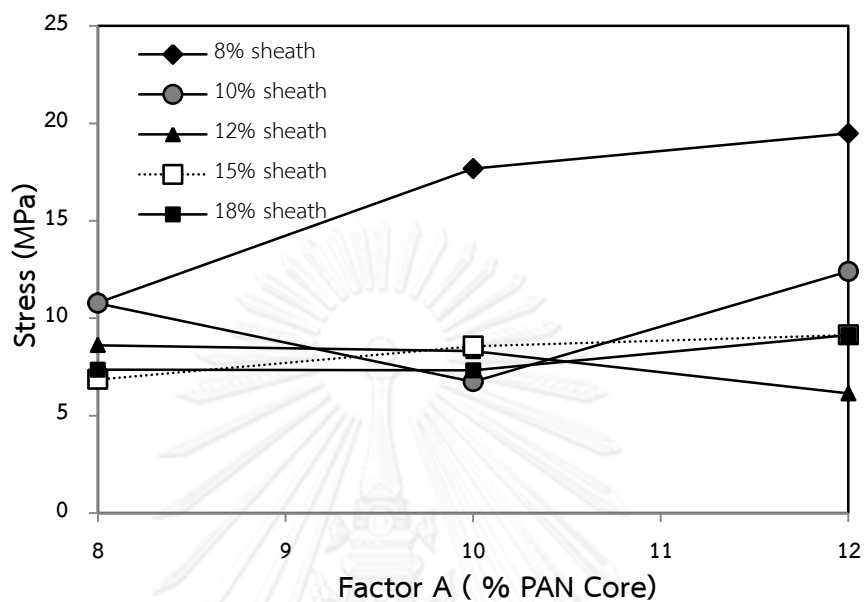
APPENDIX D

Figure D-1. Plot of the estimated treatment means shows percentage of PVP sheath
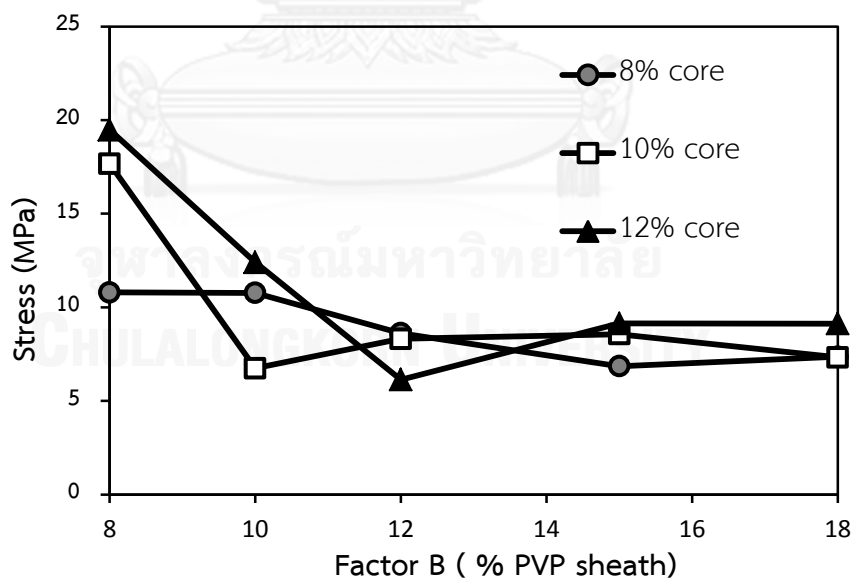
curves

Figure D-1. Plot of the estimated treatment means shows percentage of PAN core

curves

APPENDIX E

LIST OF PUBLICATION

Kanchat Chutchakul, Varong Pavarajarn, "Fabrication of Flexible PAN/ZnO Core/Sheath nanofibers by Coaxial Electrospinning for Photocatalytic Applications", The 2nd Joint Conference on Renewable Energy and Nanotechnology 2013, Higashi-Hiroshima, Japan, November 25-26, 2013.

Fabrication of Flexible PAN/ZnO Core/Sheath nanofibers by Coaxial Electrospinning for Photocatalytic Applications

Kanchat Chutchakul and Varong Pavarajarn*
Department of Chemical Engineering, Chulalongkorn University,
Bangkok, THAILAND
* Corresponding E-mail: Varong.P@chula.ac.th

Abstract

Polyacrylonitrile (PAN)/zinc oxide (ZnO) nanofibers were fabricated in flexible core/sheath structure using combination of sol-gel and co-axial electrospinning techniques. PAN dissolved in dimethyl formamide (DMF) was used as core-solution while poly vinyl pyrrolidone (PVP) solution containing ZnO sol in DMF was used as sheath-solution. Concentration of PAN in the core-solution was fixed at 8 wt%, while the PVP concentration in the sheath-solution was varied in the range of 8 to 18 wt%. Under the applied potential of 25 kV, the uniform and bead-free co-axial nanofibers can be fabricated. The average diameter of the as-spun co-axial nanofibers is in the range of 400-510 nm. Upon the calcination, at temperature in the range of 400-500°C, PVP in the sheath is removed while ZnO sol is crystallized into ZnO nanoparticles attached to the PAN core. The presence of PAN core, which can withstand the calcination, provides flexibility for the final PAN/ZnO nanofibers so that crumbling of the fibers during the use can be avoided. The calcined fibers have average diameter of 240-310 nm. The obtained fibers were characterized by universal testing machine for their strength and flexibility, thermogravimetric analysis for PAN content, X-ray diffraction (XRD) for crystallinity, scanning electron microscopy (SEM) and transmission electron microscopy (TEM) for size and morphology.

Key words: ZnO nanofibers, Co-axial electrospinning, Flexible, Photocatalyt, Core/Sheath structure

1. Introduction

ZnO has been attracting much attention to industry today because of its important role in various applications. One of the most promising uses of ZnO is being photocatalyst, which has been widely reported in literature. Most studies were carried out using nanocrystals. Although nanoparticles show high photocatalytic efficiency, in practical processes, the separation of these fine-powders after the reaction is complete could be difficult. On the other hand, metal oxides have been fabricated in the form of nanofiber, which is much easier to separate from the fluid [1, 2]. Unfortunately, most ceramic nanofibers are easily crumbled into powder after repeated. It is, therefore, the objective of this research to introduce polymer core into the nanofiber structure to retain its flexibility. In this work, it is achieved by using co-axial elctrospinning in which PAN is supplied as the core, while ZnO sols dispersed in PVP is formed into covering sheath.

2. Experimental

The PAN core solution was prepared by dissolving PAN (Mw=150,000) in DMF at 60°C and stirred for 1h. The concentration of PAN was fixed at 8 wt%. At the same time, ZnO sol was prepared by dissolving 3.29 g of zinc acetate and PVP at different content in the range of 8 to 18 wt% with respect to zinc acetate in 20 ml of DMF and

stirred to get the precursor solution. Then, a mixture of 0.26 ml distilled water, 0.18 ml HCl and 1.58 ml diethanolamine in 5 ml DMF was dropped into the precursor solution and continuously stirred for 2 h to form the sheath solution.

Each electrospinning solution was filled into a plastic syringe and connected to core and annular part of the coaxial nozzle, respectively. The coaxial electrospinning process was initiated by applying electric potential with the field strength of 1 kV/cm between the tip of the nozzle and the collector drum, which was located at 25 cm from the nozzle. The flow rates of both core and sheath solutions were controlled at 0.8 ml/h. The products collected on the drum were calcined at 400-500°C for 2 h, using heating rate of 10°C/min, in a muffle furnace.
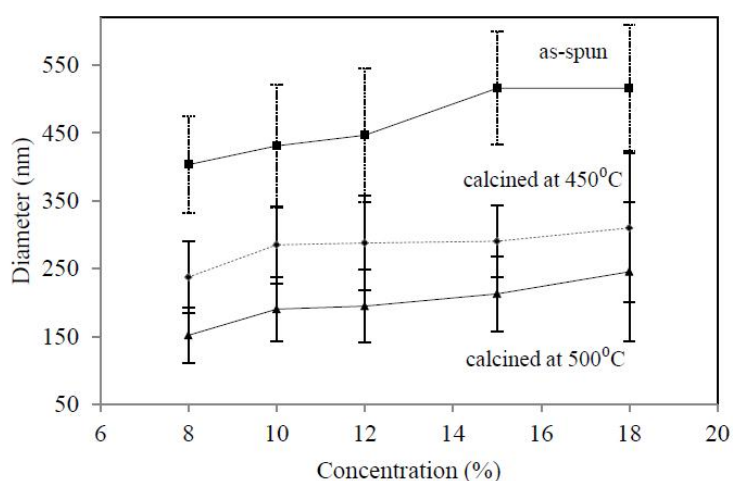
Fig.1 The diameters of co-axial nanofibers on varying concentration 8%, 10%, 12%,15% and 18% of PVP sheath by weight and fixing 8% PAN core before calcined, after calcined at 450°C, and after calcined at 500°C
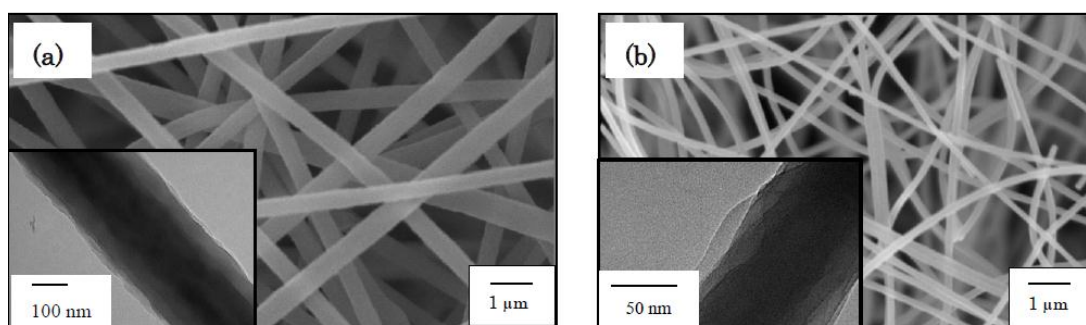
Fig.2 SEM and TEM images of co-axial nanofibers 15% PVP sheath and 8%PAN core; (c) before calcination,(d) after it had been calcined in air at 450°C

3. Results and Discussion

It has been reported that the increase in concentration of the core solution results in the increased size of the core which consequently increases overall fiber

diameters [3]. In this work, it was found from preliminary experiments that the suitable PAN concentration is 8 wt%, of which viscosity of the core solution is 0.11 Pa·s, yielding uniform fibers with the diameter of 380±45 nm. The other important factor affecting morphology of the co-axial fibers is the concentration of PVP in the sheath solution. In this study, the PVP concentration was varied from 8 to 18 wt%, which gave viscosity of the sheath solution in the range of 0.05 to 0.35 Pa·s. According to **Fig.1**, the average diameter of the co-axial nanofibers is gradually increased when the PVP concentration becomes higher. The fibers become smaller as they are subjected to the calcination because of the loss of solvent and the degradation of PVP. The higher the calcination temperature is, the smaller the final fibers become. It should be noted that the calcination temperature used in this work, i.e., 450-550°C, was determined from the degradation temperature of PVP and PAN analyzed by TGA, respectively.

The SEM images of the co-axial fibers before and after calcination at 450^{0}C for 2 h are shown in **Fig.2a** and **2b**, respectively. The fibers are smooth and uniform in size. The core/sheath structure was confirmed by TEM as shown in the insets of **Fig.2**.
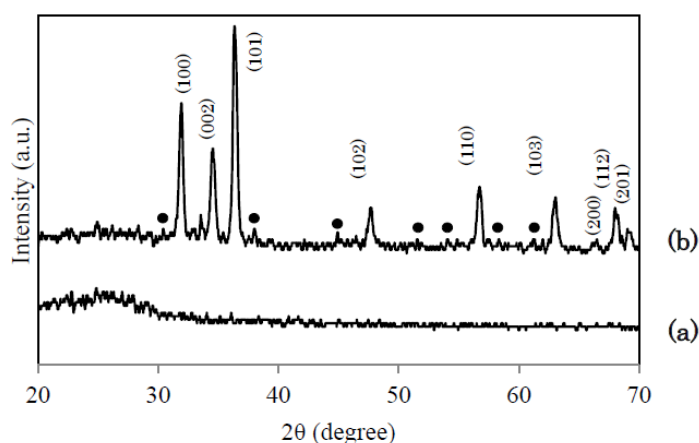

Fig.3 X-ray diffraction patterns: (a) pristine PAN after calcination, (b) co-axial nanofibers after calcination at 500^{0}C

The crystalline phase of ZnO is an important factor influencing its photocatalytic activity. According to XRD results shown in **Fig.3**, the co-axial product after calcination at 450°C contains ZnO in wurtzite structure as well as unidentified crystalline materials (represented by solid markers). The crystallite size of the ZnO phase calculated by the Debye-Scherrer was found to be 21 nm. It is also suggested from the XRD analysis of neat PAN fibers that the core part of the product remains as amorphous phase after the calcination.

The flexibility of the PAN/ZnO core/sheath nanofibers was investigated by universal testing machine. It can be seen from **Fig.4** that mechanical behavior of the products after calcination at 450°C is somewhat similar to that of the as-spun fibers, i.e., consisting of two regions starting from linear elastic region and subsequent plastic region. The ductile behavior shown by the plastic region is the significant indicator for the flexibility of the fibers (also shown in **Fig.4b**). Nevertheless, it should be noted that the yield strength of the calcined fibers is about 24% lower than that of the as-spun fibers due to the deterioration of PAN by heat. When the calcination temperature was raised to 500°C, however, the obtained fibers reveal the lack of the plastic region representing brittle behavior. The mechanical performances of the products are summarized in **Table 1**.
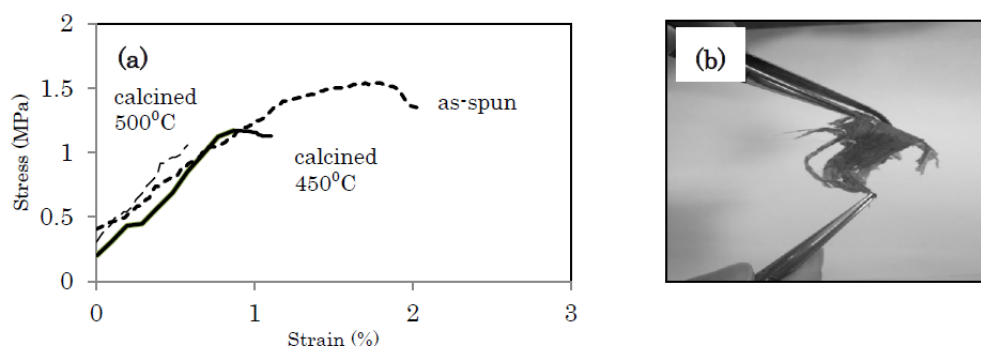
Fig.4. (a) Stress-strain curves of co-axial fibers before calcination and after it had been calcined at 450°C and at 500°C, (b) PAN/ZnO co-axial fibers after calcination at 450°C.

Table1. Mechanical Properties of co-axial nanofibers.

Co-axial fibers	thickness (mm)	Young Modulus (MPa)	Yield Strength (MPa)	Ultimate strength (%)	Fracture (%)
As-spun	0.18	24.35	1.54	1.77	2.11
After calcination at 450°C	0.23	13.31	1.17	0.90	1.13
After calcination at 500°C	0.20	40.82	1.06	0.60	0.60

4. Conclusion

In this study, the flexible PAN/ZnO core/sheath coaxial nanofibers were successfully prepared by combined sol-gel process and co-axial electrospinning, yielding the smooth surface, bead-free and uniform fibers. The core/sheath structure was formed before the calcination and was retained after the calcination. Even after the calcination at relatively high temperature to convert ZnO sols into wurtzite phase, the PAN core is still present to provide flexibility of the fibers.

References

[1] Alves, A., et al., *Photocatalytic activity of titania fibers obtained by electrospinning*. Materials Research Bulletin, 2009. **44**(2): p. 312-317.
[2] Li, D. and Y. Xia, *Fabrication of titania nanofibers by electrospinning*. Nano Letters, 2003. **3**(4): p. 555-560.
[3] Moghe, A. and B. Gupta, *Co-axial Electrospinning for Nanofiber Structures: Preparation and Applications*. Polymer Reviews, 2008. **48**(2): p. 353-377.

VITA

Mister Kanchat Chutchakul was born on 3rd October, 1989, in Phuket, Thailand. He graduated from Triam Udom Suksa School. He received the Bachelor's degree of Engineering with a major in Chemical Engineering from Chulalongkorn University, Bangkok in April 2012. He continued his Master study in the major in Chemical Engineering at Chulalongkorn University, Bangkok, Thailand in May 2012.